UNIVERSITY OF CALIFORNIA SAN DIEGO

The dynamics of internal tides and mixing in coastal systems

A dissertation submitted in partial satisfaction of the
requirements for the degree
Doctor of Philosophy

in

Oceanography

by

Madeleine M. Hamann

Committee in charge:

Professor Matthew H. Alford, Chair
Professor Andrew J. Lucas, Co-Chair
Professor Peter J.S. Franks
Professor Jennifer A. MacKinnon
Professor Eugene R. Pawlak

2019

The dissertation of Madeleine M. Hamann is approved, and it is acceptable in quality and form for publication on microfilm and electronically:

_____

_____

_____

_____
Co-Chair

_____
Chair

University of California San Diego

2019

DEDICATION

To my family–especially to my parents and siblings–whose endless love and support gives me the freedom to explore unknown worlds.

EPIGRAPH

"Problems that remain persistently insoluble

should always be suspected

as questions asked in the wrong way."

Alan Watts

TABLE OF CONTENTS

LIST OF FIGURES

LIST OF TABLES

ACKNOWLEDGEMENTS

First, I want to thank my committee chair, Matthew, for the priceless gift his mentorship has been for me over the last five years. Thank you for sharing your wealth of knowledge, inspiring me with your lofty yet grounded visions and your curiosity, and for being the kind of leader who empowers everyone you work with. Thank you for giving me the freedom and encouragement to explore my passions both within and outside of the academic world. Most importantly, thank you for your friendship, your vulnerability, and your love – it completely transformed my life.

I would also like to thank my co-chair, Drew, for his crucial contributions to my graduate experience. Thank you for the many extra hours, the enthusiasm, and the unwavering force of will you put in to collect these data. Thank you, even more, for being an example of everything that can be accomplished with a little elbow grease.

I would also like to acknowledge the rest of my thesis committee (Jen, Peter, and Geno) for their time and for the new perspectives that they brought to this work – I couldn't have asked for a more enthusiastic, curious, helpful, and supportive team.

I would like to thank all of my co-authors (Matthew H. Alford, Andrew J. Lucas, John B. Mickett, Amy F. Waterhouse, Marion S. Alberty, Samuel Billheimer, Celia Y. Ou, and Veronica Tamsitt) for their contributions to this work – for their brilliance, patience, dedication, and friendship, I am most grateful.

Thank you to my cohort and to all of the students and post-docs who toiled through late night problem sets, watched and gave feedback on practice talks, and generally shared their moral support, their incredible intellect, and their inspiring diligence. Thank you, especially, to my mentor Bonnie Ludka who shed so much light on making difficult decisions, and to Maddie Harvey, Sarah Shackleton, Dara Goldberg, Jeff Sussman, Eric Gallimore, and Ned Richards for always making light of the PhD experience and for many many many hours of full belly laughter.

To the MOD pod – watching this group grow from its infancy to the large, organized,

supportive, talented, and fun-loving collection of humans it is today has been one of the most inspiring aspects of my time here. A special thanks to Jonny Ladner, Sara Goheen, Tyler Hughen, San Nguyen, Gunnar Voet, Paul Chua, and Sam Fletcher for the technical support that made my Frankenstein student experiments possible. I have learned so much from all of you and look forward to many more days in the field with these talented, hard-working folks.

I would like to give a special thanks to Bruce Applegate and the UC Ship Funds program. Without this amazing program and the gift it is to Scripps students and scientists, this work would not have been possible. Thanks also to the National Science Foundation for funding my Graduate Research Fellowship. This funding allowed me the freedom and flexibility to pursue a project of my choice.

Finally, I want to thank my many families for their love, support, and inspiration that has shaped me into the woman I am today. I could not be luckier to have been born into the most silly, funky, fun-loving, compassionate, and loving family – I love you all to the moon and back. And to my chosen families – my Fern Glen family, my Arenas Street family, my Notre Dame family, my yoga family, my acro family, my Space family, my Burning Man family, my at-sea adventure family – what a joy and a blessing it has been to discover a world beyond the midwest with the help and support of these magical people. Each one of you have so many talents and such unique experience. To be with you is to see new possibilities everywhere, and to know that there is hope for this world yet.

Chapter 1, in full, is a reprint of the material as it appears in Journal of Geophysical Research: Oceans, 2018. Hamann, Madeleine M.; Alford, Matthew H.; Mickett, John B., 2018. The dissertation/thesis author was the primary investigator and author of this paper.

Chapter 2, in full, is a reprint of the material as it appears in Journal of Geophysical Research: Oceans, 2017. Alberty, Marion S.; Billheimer, Samuel; Hamann, Madeleine M.; Ou, Celia Y.; Tamsitt, Veronica; Lucas, Andrew J.; Alford, Matthew H., 2018. The dissertation/thesis author was the primary investigator and author of this paper.

Chapter 3, in part, is currently being prepared for submission for publication of the material. Hamann, Madeleine M.; Alford, Matthew H.; Lucas, Andrew J.; Waterhouse, Amy F. The dissertation/thesis author was the primary investigator and author of this material.

Chapter 4, in part, is currently being prepared for submission for publication of the material. Hamann, Madeleine M.; Alford, Matthew H.; Lucas, Andrew J. The dissertation/thesis author was the primary investigator and author of this material.

VITA

2013	B. S. in Civil and Environmental Engineering *magna cum laude*, University of Notre Dame.
2017	M. S. in Oceanography, Scripps Institution of Oceanography, UC San Diego. Field of study: Physical Oceanography.
2019	Ph. D. in Oceanography, Scripps Institution of Oceanography, UC San Diego. Field of study: Physical Oceanography.

PUBLICATIONS

Hamann, M. M., Alford, M. H., & Lucas, A.J., "Internal tides in a submarine canyon with variable stratification: reflectivity, mixing dynamics, and stationarity", *in prep. for Journal of Physical Oceanography*.

Hamann, M. M., Alford, M. H., Lucas, A.J., & Waterhouse, A.F., "Reflected internal tides in a shelf-incising submarine canyon: dynamics, turbulence, and context", *in prep. for Journal of Physical Oceanography*.

Nazarian, R., Legg, S., Waterhouse, A.F., & **Hamann, M. M.**,"Internal Wave Scattering in a Selection of Continental Slope Canyons", *Journal of Physical Oceanography*, *submitted*.

Hamann, M. M., Alford, M. H., & Mickett, J. B., "Generation and Propagation of Nonlinear Internal Waves in Sheared Currents Over the Washington Continental Shelf", *Journal of Geophysical Research: Oceans*, 2018.

Alberty, M. S., Billheimer, S., **Hamann, M. M.**, Ou, C. Y., Tamsitt, V., Lucas, A. J., & Alford, M. H., "A reflecting, steepening, and breaking internal tide in a submarine canyon", *Journal of Geophysical Research: Oceans*, 6872:6882, 2017.

Kennedy, A.B., Westerink, J.J., Smith, J.M., Hope, M.E., Hartman, M., Taflanidis, A.A., Tanaka, S., Westerink, H., Cheung, K.F., **Hamann, M. M.**, Minamide, M., Dawson, C., "Tropical cyclone inundation potential on the Hawaiian Islands of Oahu and Kauai", *Ocean Modelling*, 52-53, 2012.

ABSTRACT OF THE DISSERTATION

The dynamics of internal tides and mixing in coastal systems

by

Madeleine M. Hamann

Doctor of Philosophy in Oceanography

University of California San Diego, 2019

Professor Matthew H. Alford, Chair
Professor Andrew J. Lucas, Co-Chair

This thesis examines two phenomena that occur over the continental shelf and generate mixing in stratified coastal systems.

In Chapter 1, we examine the generation, propagation, and dissipation of nonlinear internal waves (NLIW) in sheared background currents on continental shelf offshore of Washington state. At the shelf break, semi-diurnal (M_2) energy flux is onshore and the incident M_2 internal tide is partially reflected and partially transmitted. NLIW appear at an inshore mooring at the leading edge of the onshore phase of the baroclinic tide, consistent with nonlinear transformation of the shoaling internal tide as their generation mechanism. Of the M_2 energy flux observed at the

eastern extent of the generation region approximately 30% goes into the NLIW observed inshore.

NLIWs are tracked into shallow (30-40 m) water, where a vertically sheared, southward current becomes strong. As train-like waves propagate onshore, wave amplitudes of 25-30 m and energies of 5 MJ decrease to 12 m and 10 kJ, respectively. The observed direction of propagation rotates from 30° N of E to $\sim$ 30° S of E in the strongly sheared region. Bore-like waves do not rotate and do not appear to lose energy within the observed ranges.

Chapters 2-4 are focused on the dynamics of internal tides in the La Jolla Canyon System (LJCS) a steep, shelf-incising submarine canyon off the coast of San Diego, California.

In Chapter 2 we present the results from a short student-led study at the steep head of the canyon system. Baroclinic energy flux is oriented up-canyon and decreases from 182 ± 18 W m^{-1} at the canyon mouth to 46 ± 5 W m^{-1} near the head. Variance is dominated by the semi-diurnal (M_2) tide which is partially standing. Moving up-canyon, the relative importance of M_2 decreases and its higher harmonics are needed to account for a majority of the observed variance, indicating steepening. Steep internal tides cause large isopycnal displacements ($\sim$50 m in 100m water depth) and high strain events. These events coincide with enhanced dissipation of turbulent kinetic energy at mid-depths.

In Chapter 3, we present results from spatial surveys of the LJCS made during a more extensive follow-up experiment. M_2 energy flux was oriented up-canyon and contained mostly in mode 1. High values of dissipation occurred near the canyon head at mid-depths associated primarily with high strain. Modal analyses suggest that LJCS was reflective to the mode 1 M_2 tide. Higher modes were found to be progressive, and smaller energy fluxes associated with them were oriented down-canyon, suggesting that incident low-mode waves were both back-reflected and scattered. Flux integrated over a canyon cross-section was always onshore, but generally decreased moving shoreward (240 kW to 5 kW), with a jump in flux occurring on a section just

inshore of the canyon's major bend due to reflection of incident waves from the steep sidewalls of the meander. Flux convergence from canyon mouth to head was balanced by the volume integrated dissipation observed. By comparing simple energy budgets from all canyons with sufficient observations, a similar balance is found for most canyons suggesting that much of the elevated turbulence in these canyon systems is driven by internal tide dynamics.

In Chapter 4, we use long, coincident time series from the same experiment to examine temporal variability of the internal wave field, internal tide dynamics, and associated mixing in the LJCS. Results from Chapter 3 are confirmed: the M_2 internal tide dominates the signal in both velocity and isopycnal displacement and it is partially standing throughout the measurement period; near the canyon mouth, dissipation is bottom-enhanced and occurs during up-canyon flow periods, while near the canyon head dissipation is elevated during high strain events at mid-depths and time-averaged dissipation is elevated throughout the water column.

At the canyon head spring-neap cycles in depth-integrated energy, energy flux, stratification, and dissipation occur at times throughout the year. Depth-integrated chlorophyll fluorescence also demonstrates spring-neap variability; maxima in [Chl] lag behind maxima in M_2 internal tide energy by 2-3 days. Phase offsets between the surface tide and harmonic fits to isopycnal displacement (η) are relatively constant, suggesting that the internal tide incident at the canyon mouth is generated nearby. At the head of the canyon the skill of a harmonic fit to η over a 90-day fit window is 49.7% – very high when compared to most other coastal mooring records that have been similarly assessed and indicating surprisingly high stationarity of the internal tide in the canyon. Long time series within canyon systems are rare, and this result could motivate an investigation into whether the skill of internal tide predications may be useful near canyon systems or steep topographic features more generally, and whether such regular tidal motions foster significant enhanced productivity nearby.

Introduction

Acting at the smallest scales of space-time continuum, turbulence and mixing in the ocean are integral to dynamics that arise and drive her movement and evolution. Large-scale meridional overturning circulation (MOC; driven by dense water formation at the poles) and eddy-generating processes remove potential energy that must be re-supplied by small-scale mixing processes to maintain the ocean's circulation [*Munk*, 1966]. Since the late sixties, when instrumentation to sense turbulent motions in the ocean was first developed, it has become increasingly evident that mixing is far from uniform in the ocean's interior – rather, turbulence is intermittent, patchy, and difficult to predict given our current level of understanding [*Gregg and Cox*, 1972; *Gregg*, 1998; *MacKinnon et al.*, 2017].

While its distribution and the dynamics that drive it are only partially understood, it is clear from a modeling perspective that understanding and parameterizing the horizontal and vertical distribution of turbulence in the ocean is of order one importance in the effort to successfully reproduce the ocean's circulation and coupled atmospheric processes [*Samelson*, 1998; *Simmons et al.*, 2004; *Saenko and Merryfield*, 2005; *Jochum*, 2009; *Friedrich et al.*, 2011]. Coupled ocean-sea ice models are highly sensitive to vertical mixing parameterization [*Goosse et al.*, 1999]. Varying the vertical distribution of mixing on the boundaries in global climate models (GCMs) modifies circulation and heat distribution in a robust way and changes basin-averaged thermocline temperatures [*Melet et al.*, 2016]. Re-partitioning mixing that occurs in modern-day shallow seas into the deep ocean during the last glacial maximum (LGM) leads to enhanced MOC

and quadrupled energy fluxes below 200m [*Schmittner et al.*, 2015]. Obtaining skillful results from global models hinges on correct reproduction of small-scale mixing dynamics.

The investigations presented in this thesis are concerned primarily with mixing that occurs in stratified waters at the ocean's margins. Of the 3.5 TW of energy input from wind and lunisolar tides, 2.6 TW (73%) is dissipated on the ocean's shelves and in its shallow seas [*Wunsch and Ferrari*, 2004]. This dissipation is relevant primarily to the shallow cell of the ocean's overturning circulation, which dominates meridional heat transport in the Pacific [*Talley*, 2003], drives and responds to changes in atmospheric circulation patterns [*Lee*, 2004], and regulates the uptake of atmospheric CO_2 [*DeVries et al.*, 2017]. Dissipation over the shelf also drives buoyancy fluxes and circulation along the coast – the most immediately accessible and relevant region of ocean for mankind; one that is an important source of food, a conduit for industrial activities, and a recipient of terrestrial runoff of nutrients, sediments, and pollution. Mixing processes in the coastal ocean have an impact on all of these.

The focus of this work is on mixing in stratified coastal systems that results from high-frequency (tidal) motions superimposed on a slowly-varying background state. It examines two phenomena that are both of near-ubiquitous relevance in coastal regions: high-frequency nonlinear internal waves (NLIWs) and mixing processes in submarine canyons.

Nonlinear Internal Waves

Since they were first discovered in the ocean in the mid-70's [*Osborne and Burch*, 1980], NLIWs have been observed both in situ and via satellite imagery across the world's coastlines [*Apel et al.*, WHOI-2006-04; *Jackson et al.*, 2012]. They induce large isopycnal displacements and velocities and have been observed to cause strong mixing [*Sandstrom and Oakey*, 1995; *MacKinnon and Gregg*, 2003; *Moum et al.*, 2007; *Shroyer et al.*, 2010a]. NLIWs can thus play a key role in the coastal environment by impacting lateral mass transport and cross-shelf exchange

[*Sandstrom and Elliott*, 1984; *Pineda*, 1991; *Scotti and Pineda*, 2007], vertical flux of energy, nutrients, and heat [*Shroyer et al.*, 2010b], and acoustic propagation [*Chiu et al.*, 2004].

Although they have been the focus of numerous theoretical, laboratory, and observational studies, the vast majority work has focused on the properties of NLIWs in a two-dimensional, uni-directional, and weakly-nonlinear sense. The effects of continuous stratification, background currents, and shear have been studied for only a handful of simple cases [*Stastna and Lamb*, 2002; *Choi*, 2006]. Our understanding of NLIW dynamics – especially where and how they dissipate – is far from complete.

In areas partially isolated from the open ocean, NLIW arrivals are observed to be phase-locked to the barotropic tide [*Apel et al.*, 1985; *Hyder et al.*, 2005; *Lien et al.*, 2014], suggesting two primary NLIW generation mechanisms in the ocean: 1) nonlinear steepening and transformation of the internal (baroclinic) tide impinging upon slope-shelf topography [*Lee and Beardsley*, 1974; *Gerkema*, 1995; *Nash et al.*, 2012], and 2) the release and subsequent evolution of lee waves formed on the ebb (barotropic) tide [*Maxworthy*, 1979; *Farmer and Smith*, 1980; *Farmer and Armi*, 1999; *Scotti et al.*, 2008]. NLIWs observed in areas exposed to the open ocean do not exhibit a strong phase-locked relationship to the local barotropic tide, suggesting that remotely generated internal tides, refracted by variable currents and stratification, are their primary source [*Jeans and Sherwin*, 2001; *Shroyer et al.*, 2011; *Moum and Nash*, 2008]. However, due to the variability of conditions between possible generation sites and the corresponding irregularity of NLIW observations in open shelf regions, direct observation of their generation has remained elusive.

In Chapter 1 of this thesis, observational evidence of NLIW generation is presented. At the shelf break, an incident low-mode tide is partially reflected and partially transmitted. Approximately 30% of the transmitted internal tide energy is transformed into NLIW that propagate into a laterally variable and strongly sheared tidal current – a common paradigm in the coastal ocean. The NLIW observed inshore are either train-like or bore-like. Those that are

train-like rotate clockwise up to 90 degrees and lose energy steadily as they progress onshore into a vertically sheared, southward current. Bore-like waves do not rotate, nor do they appear to lose energy as trains do. Although predicting the exact timing and character of NLIWs that occur at this location remains a challenge [*Zhang et al.*, 2015], we offer here better understanding of both the origin and fate of those waves.

Submarine Canyons

Submarine canyons are common features of the coastal ocean, incising up to 20% of the continental margins around the globe [*Hickey*, 1995; *Harris and Whiteway*, 2011]. These conduits cut across the otherwise shallow and gently sloping continental shelf, and thus are natural pathways by which deep, nutrient–rich waters from offshore may be channeled into coastal ecosystems [*Allen and Hickey*, 2010]. In addition to nutrients, a canyon's steep-walled geometry can trap energy from the incident internal wave field and focus it towards its head [*Hotchkiss and Wunsch*, 1982]. En route, interactions with the complex topography give rise to turbulent processes that dissipate this energy.

In the few canyons studied to date, observed dissipation rates and diapycnal diffusivities are up to 1000 times the average in the open ocean [*Kunze et al.*, 2002; *Lee et al.*, 2009; *Zhao et al.*, 2012; *Wain et al.*, 2013]. *Kunze et al.* [2012] extrapolate from their observations that these canyon-related processes may contribute up to 15% of the dissipation of internal wave energy globally–or 10% of the diapyncal diffusivity required to balance bottom water formation at the poles. Locally, the resulting mixing sets the properties of onshore flows and may govern both the vertical and lateral distribution of heat, carbon, oxygen, and nutrients [*Allen et al.*, 2001; *Carter and Gregg*, 2002; *Lee et al.*, 2009].

The distribution of canyons along coastlines is highly heterogeneous [*Harris and Whiteway*, 2011] so that they are primary candidates for inducing lateral heterogeneity in diapycnal

transport at the margins of the ocean. Such lateral heterogeneity has a strong influence in GCMs [*Friedrich et al.*, 2011; *Melet et al.*, 2013]. In addition, the range of processes that arise in canyons and generate turbulence at different depths [*Waterhouse et al.*, 2017; *Alberty et al.*, 2017] may be significant in altering the *vertical* distribution of mixing along the continental shelf, which has been shown to have the largest influence on model results [*Melet et al.*, 2016]. Understanding and parameterizing processes in coastal canyons may be integral to our ability to model the global circulation, and the knowledge required to parameterize those effects is far from complete.

The dynamics of internal waves in canyons is of particular interest due to their tendency to trap and funnel waves of tidal frequency. Upon encountering an obstacle, an IW's behavior depends upon both its characteristic slope (S_w) and the slope of the impacted feature (S_b). A steep obstacle ($\frac{S_w}{S_b} < 1$) is considered to be "supercritical" and causes the wave to reflect backward, leading to standing wave patterns. Gentle bathymetric slopes ($\frac{S_w}{S_b} > 1$, subcritical) allow the wave to reflect forward. Slopes nearly equal to the characteristic wave slope will cause "critical reflection" where reflected waves have high wavenumber and energy density leading to breaking and dissipation near the bottom [*Eriksen*, 1982; *Ivey and Nokes*, 1989]. In a canyon, whose sidewalls are generally steep, incident internal waves are reflected downward. Whether they then progress forward, reflect back, or dissipate then depends on the slope and ambient stratification.

Chapters 2-4 of this work center around observations made in the La Jolla Canyon system (LJCS)–a 24 km long shelf-incising canyon system in San Diego, California . The slope along the axis of the canyon system transitions from slightly subcritical to the M_2 internal tide to supercritical $\sim$1km from the bifurcation point (Fig. 3.1). This relatively short, "transcritical" geometry is common for shelf-incising canyons (e.g. Eel canyon observed by *Waterhouse et al.* [2017]) and makes for complicated internal wave dynamics given that the location of critical slopes can change with variable stratification or internal wave frequencies. Studies in the anomalously large, mostly subcritical Monterey Canyon have given some insight as to the effects of variable stratification [*Petruncio et al.*, 1998; *Zhao et al.*, 2012]; however, no long-term

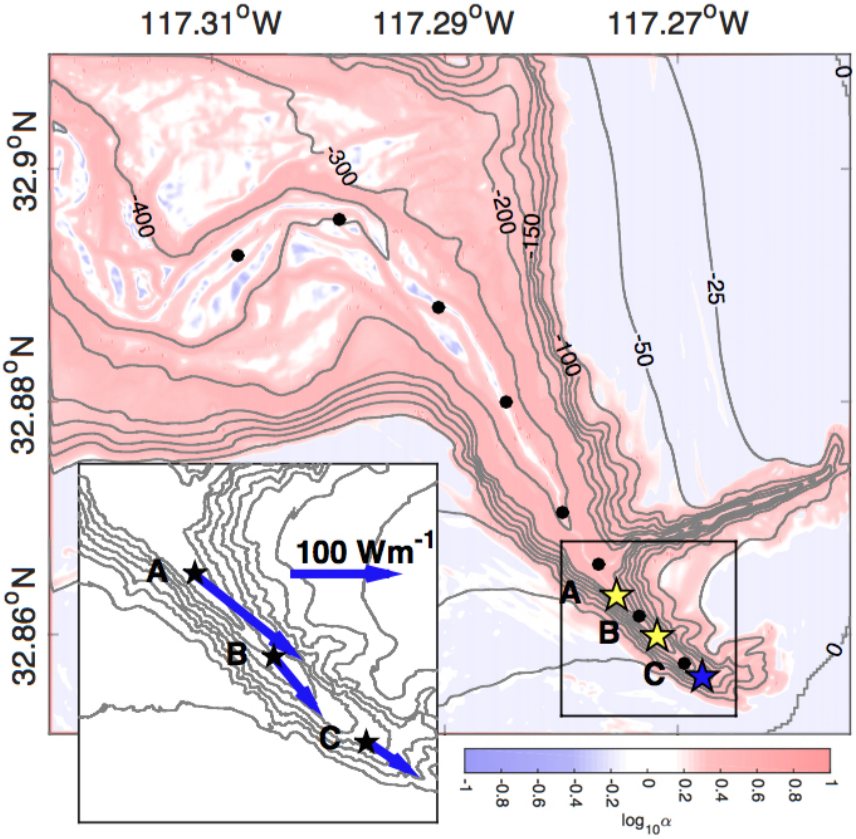

Figure 0.1: Criticality ($\log \alpha$) of the bathymetry in the greater LJCS. Positive (red) values indicate supercritical slopes, negative (blue) subcritical. Stars indicate the location of 25-hour shipboard stations (A and B, yellow) and the mooring (C, blue). Black dots indicate the location of single casts taken during the along-axis section. Bathymetry is contoured (grey) at 25 m intervals from 0 to 200 m and 100 m intervals thereafter. Inset: Vectors indicating the magnitude and direction of the depth- and time-averaged energy flux computed at each station.

moored observations have occurred in smaller or more "common" canyons until now.

From analyses of two sets of observations (one short pilot experiment focused on the main branch at the head of the LJCS, one extended study including 7 days of shipboard surveys, multiple weeks of coincident moored time series, and one full-year record at the canyon head), a detailed description of internal tide dynamics and their associated dissipation are presented. Results demonstrate that the mode-1 internal tide is partially standing throughout the observed time period. Internal tide waveforms steepen and become increasingly nonlinear approaching the canyon head. High strain regions occur on the trailing edge of plunging isopycnals, and enhanced

dissipation is concentrated in these mid-depth regions rather than being bottom-enhanced. Further offshore, where the slope of the canyon axis is less steep, depth-integrated dissipation is smaller and turbulent enhancement occurs primarily near the bottom in conjunction with up-slope flows.

Tidally-resolving spatial surveys are leveraged to assess a tidal energy budget for the system. Conversion from barotropic to baroclinic tides within the canyon is negligible relative to flux convergence and dissipation terms which balance one another over the canyon as a whole. By comparing simple energy budgets from all canyons with sufficient observations (6 in total), a similar balance is found for most canyons. The one exception is Juan de Fuca canyon, where such a balance is not expected due to the non-tidal nature of flows therein. These results suggest that internal tides incident at the mouth of a canyon system are dissipated within the system rather than leaking over the sidewalls or siphoning energy to other wave frequencies.

A novel year-long time series from the head of the canyon system reveals spring-neap cycles in depth-integrated energy, energy flux, stratification, and dissipation occur at times throughout the year. Depth-integrated chlorophyll fluorescence also demonstrates spring-neap variability over a strong seasonal cycle; maxima in [Chl] lag behind maxima in D_2 internal tide energy by 2-3 days. Phase offsets between the surface tide and harmonic fits to isopycnal displacement (η) are relatively constant, suggesting that the internal tide incident at the canyon mouth is generated nearby. At the head of the canyon the skill of a harmonic fit to η over a 90-day fit window is 49.7% – very high when compared to most other coastal mooring records that have been similarly assessed and indicating surprisingly high stationarity of the internal tide in the canyon. Long time series within canyon systems are rare, and this result could motivate an investigation into whether the skill of internal tide predications may be useful near canyon systems or steep topographic features more generally, and whether such regular tidal motions foster significant enhanced productivity nearby.

Chapter 1

Generation and propagation of nonlinear internal waves in sheared currents over the Washington continental shelf

1.1 Introduction

Nonlinear internal waves (NLIW) occur ubiquitously in the world's coastal oceans [*Perry and Schimke*, 1965; *Osborne and Burch*, 1980; *Holloway*, 1987; *Konyaev et al.*, 1995; *Klymak and Moum*, 2003; *Scotti and Pineda*, 2004; *Hosegood and van Haren*, 2004; *Filonov and Novotryasov*, 2005; *Shroyer et al.*, 2011; *Walter et al.*, 2016]. They induce large isopycnal displacements and velocities and have been observed to cause strong mixing [*Sandstrom and Oakey*, 1995; *MacKinnon and Gregg*, 2003; *Moum et al.*, 2007; *Shroyer et al.*, 2010a]. NLIW can thus play a key role in the coastal environment by impacting lateral mass transport and cross-shelf exchange [*Sandstrom and Elliott*, 1984; *Pineda*, 1991; *Scotti and Pineda*, 2007], vertical flux of energy, nutrients, and heat [*Shroyer et al.*, 2010b], and acoustic propagation [*Chiu et al.*, 2004].

In regions isolated from the open ocean or near strong internal tide generation sites,

locally generated NLIW are observed to be phase-locked to the barotropic tide [*Apel et al.*, 1985; *Hyder et al.*, 2005; *Lien et al.*, 2014]. This relationship suggests that NLIW may be generated by the release and subsequent evolution of lee waves formed on the ebb (barotropic) tide [*Maxworthy*, 1979; *Farmer and Smith*, 1980; *Farmer and Armi*, 1999; *Scotti et al.*, 2008]. On the other hand, NLIW observed in areas exposed to the open ocean do not exhibit a strong phase-locked relationship to the local barotropic tide, suggesting that their energy is provided instead by baroclinic tides of remote origin that are refracted by variable currents and stratification [*Inall et al.*, 2000; *Jeans and Sherwin*, 2001; *Moum and Nash*, 2008; *Shroyer et al.*, 2011; *Zhang et al.*, 2015]. The latter suggests another primary generation mechanism at play in the ocean: nonlinear steepening and transformation of the internal (baroclinic) tide impinging upon slope-shelf topography [*Lee and Beardsley*, 1974; *Gerkema*, 1995; *Zhao and Alford*, 2006; *Nash et al.*, 2012; *Alford et al.*, 2015].

Because these waves are ephemeral and their generation location and mechanism are sensitive to bathymetry, stratification, and forcing it has been difficult to measure the generation of NLIW directly in open-ocean coastal environments. Accordingly, the fraction of energy from a remotely generated internal tide that transforms into NLIW upon encountering a shelf break is not yet clear [see *Helfrich and Melville* [2006] and *Lamb* [2014] for reviews of the (largely numerical) work towards this problem]. Observations from strong generation regions suggest that around 85% of the energy converted from barotropic to baroclinic tides propagates away from its source and eventually reaches remote coastlines [*Klymak et al.*, 2006]. Whether this energy is dissipated, reflected, or transmitted onto the shelf at those locations is an area of active research [*Pinkel et al.*, 2015], with clear implications for determining the global energy budget and correctly parameterizing mixing in global circulation models [*Melet et al.*, 2013]. Understanding the nonlinear transformation of the internal tide into coastal NLIW is a crucial element of this problem.

In addition to the formation of NLIW, the details of how these waves propagate across

the shelf and where they dissipate their energy is of interest for several reasons. For example, they have been shown to induce significant cross-shelf transport of mass and particles such as the pelagic larval stages of coastal dwellers [*Lamb*, 1997, 2002; *Butman et al.*, 2006; *Scotti and Pineda*, 2007; *Shroyer et al.*, 2010b] and to induce strong mixing that can significantly alter local nutrient availability and oxygen [*Sandstrom and Elliott*, 1984; *Bogucki et al.*, 1997; *Colosi et al.*, 2001; *Schafstall et al.*, 2010]. However, physics of NLIW in temporally and/or spatially variable currents is not well understood. The vast majority of theoretical, numerical, and laboratory work has focused on two-dimensional, uni-directional waves [*Lamb*, 2014], and the effects of continuous stratification, background currents, and shear have been studied for only a handful of simple cases [*Stastna and Lamb*, 2002; *Choi*, 2006]. Only a few studies of NLIW in the ocean have been carried out in exposed coastal regions with variable mesoscale currents and remotely generated internal tides, and those that have suggest nuanced dynamics that warrant further investigation into the role of NLIW in such environments [*MacKinnon and Gregg*, 2003; *Shroyer et al.*, 2011; *Nash et al.*, 2012].

The continental shelf off of the Pacific Northwest is at the northern extent of the California coastal current system. In the summer, upwelling conditions prevail with northerly winds, a southward current along the shelf, and a shallow mixed layer. During this time, stratification is strong enough to support NLIW on the shallow pycnocline. At a location off the coast of La Push, Washington, NLIW that span more than half of the water column regularly pass by the location of a long-term research mooring (Cha'ba) [*Zhang et al.*, 2015]. The NLIW arrive semi-diurnally and are correlated with both the phase and the energy of the internal tide whose tidally-averaged energy flux is typically 80 Wm^{-1} to the NE [*Zhang et al.*, 2015]. (We here report a corrigendum to *Alford et al.* [2012] and *Zhang et al.* [2015], whose report of mean fluxes to the NNE should be rotated 34° clockwise as magnetic correction was applied incorrectly.) An abrupt "fall transition" from upwelling to downwelling conditions typically occurs some time during the month of October. Winds and shelf currents reverse direction, the mixed layer deepens,

and the stratification weakens. During this time, large-amplitude solitary waves are not regularly observed.

The Washington Waves experiment, described here, was executed just before the fall transition in 2014. The experiment captures evidence of partial reflection and transmission of an incident internal tide at the shelf break and subsequent steepening into NLIW observed inshore. It also provides a detailed description of wave propagation in the sheared current environment and shoaling bathymetry inshore of Cha'ba. The paper is organized as follows: Section 1.2 describes the details of the experiment and analysis methods. Section 1.3.1 describes the observed background conditions. Section 1.3.2 documents the generation of the waves, with reflection and transmission of the incident tide documented in 1.3.2 and an energy budget assessed in 1.3.2. Wave characteristics and energetics are described in section 1.3.3 with an individual case study examined in 1.3.3 and general trends described in 1.3.3. Section 1.3.3 provides comparison with a linear ray tracing analysis. Section 1.4 offers a discussion of the results and and section 1.5 contains conclusions.

1.2 Methods

1.2.1 Observations

Shipboard data for this experiment were collected between August 27 and September 2, 2014 in the vicinity of multiyear moorings NEMO Subsurface (NEMO-SS) and Cha'ba off the coast of La Push, WA (Fig. 1.1). These moorings measure temperature, salinity, and velocity with high vertical and temporal resolution and are described in detail by *Zhang et al.* [2015]. In addition to these multi-year moorings, an upward-looking, bottom-mounted 300kHz acoustic Doppler current profiler (ADCP; L1) was deployed near the shelf break in 250m water depth at the beginning of the experiment.

For shipboard surveys, the *R/V Oceanus* continuously operated a 300 kHz hull-mounted

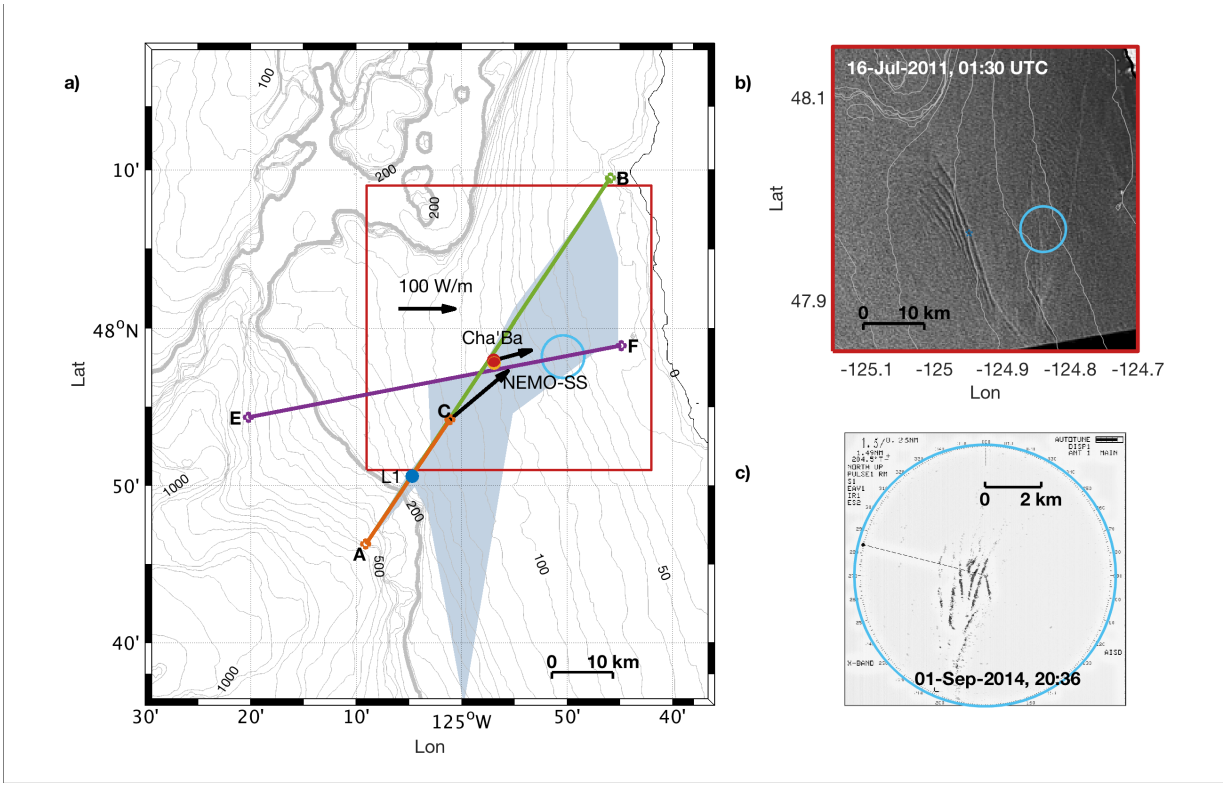

Figure 1.1: Study Region (a). Bathymetry is contoured in 10m intervals up to 200m and every 50m thereafter (grey lines, bold is 200m isobath). Mooring locations are indicated by circles: up-looking ADCP (L1, blue), Cha'ba (red), NEMO-SS (yellow). Line AB (green) and EF (orange) denote the main tracks followed during the wave chases. Line AC (orange) is the track occupied during the generation section. The blue cloud indicates the area covered by the ship throughout the experiment. Black arrows indicate the average D_2 internal tide energy flux seen at Cha'ba and at the eastern extent of AC. Waves often propagate to the ENE at Cha'ba as shown in the SAR image (b); they are observed propagating southeastward further east as shown in a shipboard X-band radar image (c). The locations of the images in (b) and (c) are shown in (a) using a red rectangle and light blue circle, respectively.

ADCP to measure currents within the upper ∼150m, a 120 kHz echosounder (BioSonics) to image vertical deflection of scattering layers caused by NLIW, and X-band radar to visualize the surface expression of NLIW. These tools, along with real-time data transmitted by Cha'ba, aided in locating and tracking NLIW that typically appear at Cha'ba once per semi-diurnal (D_2) tidal cycle (Fig. 1.2). The ship would "chase" a given train of waves, passing back and forth perpendicular to the crests at a speed of 1-2 kts (henceforth, "pass" refers to this maneuver), as it propagated from off- to on-shore. At each pass, one of two shipboard profiling packages took as

many full-depth profiles as possible through the waves. Seven waves were tracked in this manner. Five were sampled with the Modular Microstructure Profiler (MMP)—a loosely tethered body that measures temperature, conductivity, pressure, oxygen, and micro- shear and temperature as it free-falls vertically at 0.6 m s^{-1}. Two waves were sampled using the Shallow Water Integrated Mapping System (SWIMS)—a winch-driven heavy towed body that moves 1-2 m s^{-1} vertically and is equipped with up- and down-ward facing ADCPs, temperature, conductivity, pressure, oxygen, chlorophyll fluorescence, and turbidity sensors, and a "Chiometer" equipped with temperature and conductivity microstructure sensors. MMP and SWIMS complemented each other in that MMP measures shear microstructure directly at the cost of slower profiles and slower ship speeds, while SWIMS allows much faster sampling with lower resolution of the smallest scales of turbulence. Tracking operations commenced on line AB (Fig. 1.1), but after the first few waves propagated in a more eastwardly direction, operations switched to line EF (Figs. 1.1, 1.2).

SWIMS was also used to conduct a 36-hour survey at the hypothesized generation site (Fig. 1.1). During this time, the ship transited back and forth along cross-shelf line AC at 5 kts, capturing the 15-kilometer section once every 2.5-3 hours for a total of 16 occupations. The times and locations of all measurements are laid out in the Hovmöller diagram shown in Fig. 1.2.

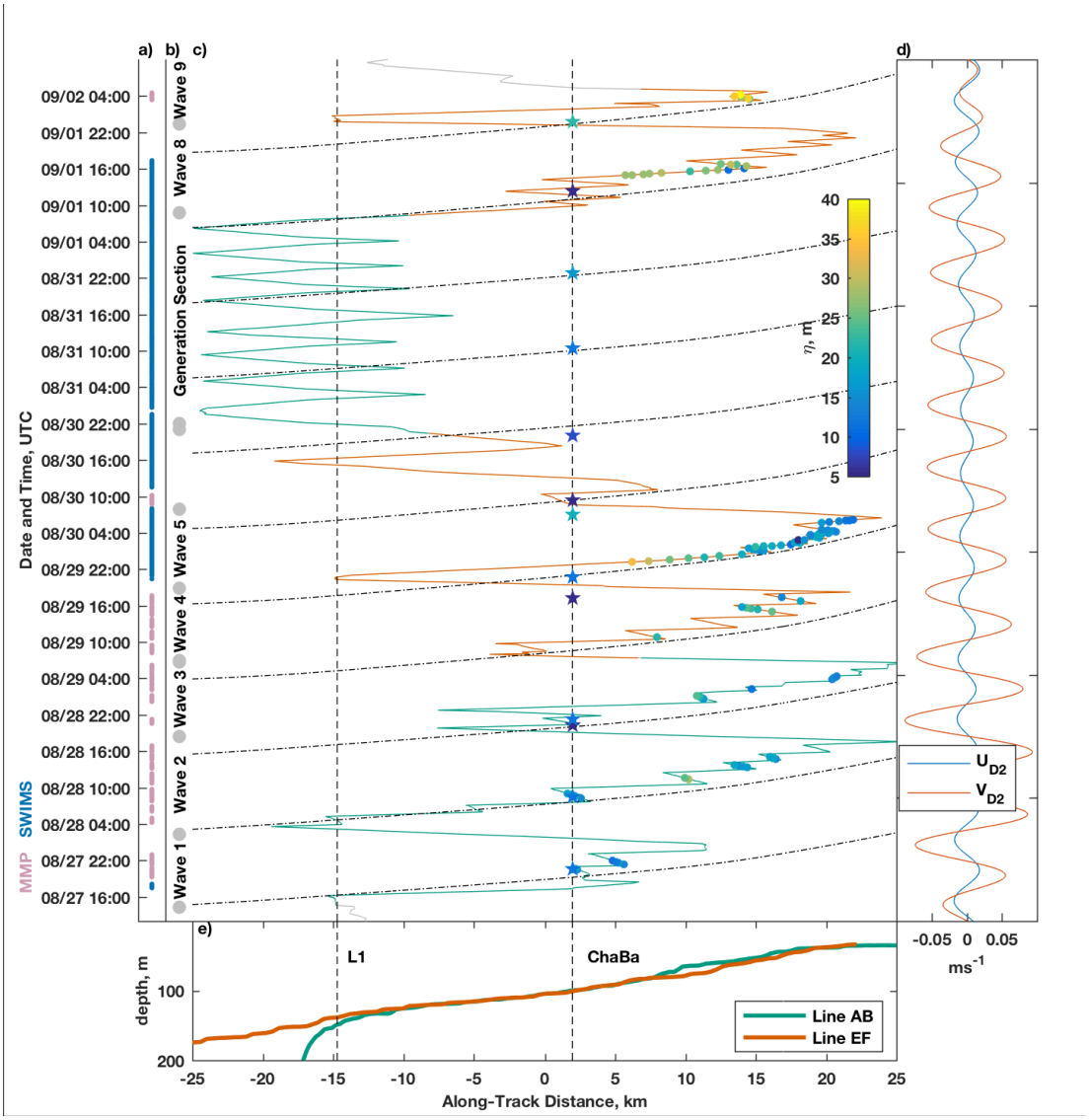

Figure 1.2: Experiment details laid out in a Hovmöller diagram. Bottom: Bathymetry along lines AB and EF. Vertical dashed lines indicate the locations of Cha'ba and bottom lander, L1. Top left: Times of SWIMS casts (blue) and MMP casts (pink). Top right: Along-track location of the ship. Green and orange colored lines differentiate between lines AB and EF, respectively. Colored dots indicate the times and along-track locations at which a wave crest was observed (color indicates the maximum amplitude). The along-track location and timing of mode-1 internal waves predicted from the data at Cha'ba are indicated with black dash-dotted lines. Colored stars indicate the time and maximum amplitude of NLIW events observed at Cha'ba.

1.2.2 Analysis

Generation Section

Shipboard surveys across the shelf break on line AC were used to investigate the spatial characteristics and energetics of the semi-diurnal internal tide. semi-diurnal motions at 24 along-track locations (stations) were isolated using harmonic analysis. For each measured profile, isopycnal displacement (η) was computed from the time mean density profile at that location. Then, semi-diurnal components of east- and north-ward velocity (u, v) and η were determined using least squares methods by fitting the data $A(x,z,t)$ to the model

$$A(x,z,t) = A_O(x,z)\sin[\omega_{D_2}t + \phi(x,z)] \tag{1.1}$$

where x is the along-track distance, ω_{D_2} is the D_2 tidal frequency, A_O is amplitude, ϕ is phase relative to a common reference time, and A represents either u, v or η. Hereafter, u, v, and η refer to the timeseries reconstructed from the model using the computed coefficients, and therefore represent only the semi-diurnal component of the total field.

Depth-integrated energy density (E) at each station was computed as the sum of available potential energy (APE)

$$APE(x) = \left\langle \frac{1}{2}\overline{\rho}\int_{-H}^{0} N^2(z)\eta^2(z)dz \right\rangle \tag{1.2}$$

and horizontal kinetic energy (HKE)

$$HKE(x) = \left\langle \frac{1}{2}\overline{\rho}\int_{-H}^{0} |\mathbf{u}^2(z)|dz \right\rangle \tag{1.3}$$

where ρ is density, the overline indicates vertical averaging, and H is the water depth.

semi-diurnal velocity perturbation, $\mathbf{u}'(z,t)$, baroclinic pressure perturbation, $p'(z,t)$, and energy flux $\langle \mathbf{F}(z) \rangle = \langle \mathbf{u}'p' \rangle$ were computed at each station according to the methods of *Kunze et al.* [2002] and *Nash et al.* [2005] where brackets indicate averaging over a tidal cycle. Uncertainty

associated with sparse temporal sampling was also computed for the fits at each depth and location following *Nash et al.* [2005].

Energetic quantities at each station were used to ascertain the progressive vs reflected character of the internal tide moving over the shelf break. The group speed (c_g) for a mode-1 D_2 internal wave was computed using the water depth and time-mean stratification at each station following *Alford and Zhao* [2007a]. In order to diagnose the reflective character of the internal tide, the ratio of $c_g E$ to F and APE to HKE was examined at each station. For a freely propagating wave, $c_g E = F$ and the ratio $r \equiv HKE/APE = (\omega^2 + f^2)/(\omega^2 - f^2) = 3.88$ for D_2 internal waves at this latitude. If the wave is partly standing, $c_g E > F$ and $r < 3.88$. Because these indicators are more accurately computed mode by mode, the reconstructed fields were also decomposed into orthogonal modes to compute the observed and theoretical group speed (c_g^{obs} and c_g^{th}, respectively) for each mode following *Alford and Zhao* [2007a] and *Martini et al.* [2007].

The generation section survey was also used to assess a cross-shelf energy budget to estimate the proportion of energy lost to dissipation or other frequency bands. The steady cross-shelf baroclinic energy balance for vertically integrated, tidally-averaged quantities is given by

$$\frac{dF_{D_2}}{dx} = -\frac{dF_{HF}}{dx} + P - \overline{\rho} \int_{-H}^{0} \langle \varepsilon \rangle \, dz, \;\; [\mathrm{Wm}^{-2}], \tag{1.4}$$

where x is cross-shelf distance, P is a production term, and subscripts indicate energy flux in the semi-diurnal and high frequency wave bands. In order to assess the budget, it was assumed that the production term P arises from the conversion of semi-diurnal surface and internal tide components and was computed at each location following the methods of *Kunze et al.* [2002] and *Kelly et al.* [2010] as

$$P(x) = \int_{-H}^{0} \Big(C_T(x) + C_S(x) \Big) dz = \int_{-H}^{0} \Big(-H_x U p' \big|_{z=-H} - \zeta_t p' \big|_{z=0} \Big) dz, \;\; [\mathrm{Wm}^{-2}] \tag{1.5}$$

where C_T and C_S are conversion terms due to internal pressure disturbances and surface dis-

placements, respectively, U is the onshore barotropic velocity, and ζ_t is the time derivative of the surface displacement. Along line AC only the semi-diurnal component of the energy flux was resolved by the sampling pattern such that an apparent reduction in D_2 energy may have been due to dissipation or to a transfer of energy to the high frequency NLIW band. As we did not operate MMP during this survey, dissipation rate (ε_{OT}, Fig. 1.5c) was inferred from density overturns greater than 0.5m in each profile following the methods of *Thorpe* [1977] and *Dillon* [1982]. Thorpe scales were chosen in this region because density depended heavily on salinity in deeper water rendering chiometer measurements unusable. During other surveys conducted in this experiment, ε_{OT} agreed reasonably well with concurrent measurements of ε from shear probes on MMP (Appendix).

Wave chases

Shipboard data inshore of line AC were used to examine the propagation and evolution of NLIW over the shelf. Continuous measurements from shipboard ADCP and BioSonics were used to identify all wave crests in a given pass. (Henceforth, "crest" is used to refer to the deepest point on a wave of depression and the shallowest on a wave of elevation). Profiles of the background velocity, $\vec{u}_{BG}(z)$, for each pass were determined by averaging data from the nearest 10-15 minute interval without waves. Wave velocities, u_w and v_w were computed by removing $\vec{u}_{BG}(z)$ along isopycnals [*Chang et al.*, 2011]. Due to the lower temporal resolution of profiles from towed instruments (especially MMP), density profiles were not available for every crest and profiles through background conditions are infrequent. Therefore, vertical profiles of isopycnal displacement were estimated from BioSonics data following *Shroyer et al.* [2011] by differencing the depth of the thermocline before and during the passage of a crest (Δz_{max}) and interpolating linearly from Δz_{max} at the depth of the wave crest to displacements of zero at the top and bottom. Propagation direction (θ_w) for each crest was computed as $\theta_w = \tan^{-1}\left(\frac{\overrightarrow{v_w}}{\overrightarrow{u_w}}\right)$ where arrows indicate vector averaging over points in the upper layer.

At each pass, phase speed (c_p) was computed as $c_p = \frac{\Delta x}{\Delta t}$ by determining the difference in time (Δt) and along-track distance (Δx; distance in meters along a track oriented in the direction of wave propagation) between observations of the wave's leading crest. The velocity of the ship relative to the wave caused Doppler shifting in the observed sections, so a wave coordinate (x_w) that accounts for this shifting was used to compute the properties of each wave crest. A start and end time for each crest (t_s and t_e) was determined by the times at which isopycnal displacement rises above and then falls below 10% of the maximum displacement observed within the packet. Wave amplitude (η_w) represented the maximum isopycnal displacement observed for each crest. The wavelength (L_w) of each crest was then computed as $L_w = x_w(t_e) - x_w(t_s)$, and x_w was computed in the direction of θ_w by accounting for the ship's speed in that direction. Uncertainty in the computed wave direction propagates accordingly into these estimates.

Uncertainty in the computed propagation direction for each crest was estimated by accounting for several possible sources. An uncertainty of 1-2 degrees was estimated for crests lacking density measurements by subsampling 20 well-sampled crests and computing wave velocities using the isopycnal displacements computed from Biosonics data, sparsely sampled density, and fully-resolved profiles. For each crest, three methods were used to extrapolate velocity measurements into the upper 10m not measured by the shipboard ADCP for both background and wave velocities, and the minimum and maximum coordinate of the thermocline were varied $\pm$1, 3, and 5 meters. Uncertainty associated with using a background state $>$10 minutes before the crest was estimated at 0.1 degrees per minute of separation by shifting the time period used to compute the background state for 5 passes for which a background state was well sampled and then fitting a trend. Uncertainty was determined by re-computing propagation direction for each of these 45 cases and compounding uncertainty from all the identified sources.

Kinetic energy (KE_w) for each crest was computed as

$$KE_w = L_w \frac{1}{2} \rho_o \left\langle \int_{z=-H}^{z=0} (u_w(z,t)^2 + v_w(z,t)^2) dz \right\rangle, \tag{1.6}$$

where $\rho_o = 1026\text{kg m}^{-3}$, and brackets indicate averaging over all profiles within a crest. For all crests through which profiles were made using SWIMS or MMP, available potential energy (APE_w) was computed as

$$APE_w = L_w \left\langle \int_{z-\zeta}^{z} g[\rho(z) - \rho_{BG}(z')]dz' \right\rangle, \tag{1.7}$$

where ζ is vertical displacement of a fluid parcel, and ρ_{BG} is background density. For these same crests, integrated dissipation (ε_w) is computed as

$$\varepsilon_w = L_w \rho_o \left\langle \int_{z=-H}^{z=0} \varepsilon(z,t)dz \right\rangle. \tag{1.8}$$

By designating the timescale (ΔT) as time elapsed between observations and assuming that the observed dissipation persisted between passes, dissipation was compared directly to the change in energy ($\frac{\Delta E_w}{\Delta T}$) from pass to pass for a given crest.

Moorings

Data from the moorings were used to provide context and to examine NLIW properties and internal tide energetics evolving over the course of the experiment. Tidally-averaged energy flux in the NLIW band was computed as

$$\langle F_w \rangle = \langle cE_w \tau_w \omega \rangle \tag{1.9}$$

where c is the phase velocity determined from shipboard observations, E_w is the wave energy, τ_w is the wave duration, ω is 12.4^{-1} hr^{-1}, and brackets indicate averaging all wave events over a tidal period. τ_w was defined as the period of time for which isopycnal displacement is greater

than 10% of the wave amplitude. Tidally-averaged D_2 energy flux

$$\langle F_{D_2} \rangle \equiv \langle \vec{u}_{D_2} p_{D_2} \rangle, \tag{1.10}$$

was computed following standard methods using bandpassed baroclinic velocity, $\vec{u}_{D_2}(z,t)$, and pressure, $p_{D_2}(z,t)$, computed from moored density measurements [*Alford et al.*, 2012]. Uncertainty in the measured D_2 fluxes at Cha'ba is estimated as 14% of the measured signal following the methods of *Nash et al.* [2005]. In computing uncertainty in NLIW energy fluxes, an uncertainty of approximately 10% in measured phase speed is assumed due to uncertainty in the propagation direction, and this uncertainty propagates into wave energy and energy flux accordingly leading to an overall uncertainty of 21-30%.

Ray tracing

Linear ray tracing analysis was employed to determine whether the behavior of the propagating NLIW was well-described by linear theory. The Taylor-Goldstein equation

$$(U-c)\left(\frac{d^2}{dz^2} - k^2\right)\hat{\psi} - \frac{\delta^2 U}{\delta z^2}\hat{\psi} + \frac{N^2}{U-c}\hat{\psi} = 0, \tag{1.11}$$

where $U(z)$ is the background velocity in the direction of the wave propagation, c is the phase speed, k is the wavenumber, and $\hat{\psi}$ is the streamfunction, was used to compute the phase speed of linear internal waves in a grid of 200m by 200m in the study region using realistic bathymetry averaged over each box [*Kundu et al.*, 2012]. Where available, the observed stratification and velocity profiles were binned and averaged; otherwise, stratification from the box nearest in distance and depth was assigned. Beginning at Cha'ba, straight wave crests of 10km breadth with starting angles varying between 30° and 120° true were tested under three scenarios: case 1) without currents (phase speed changes due to changes in bottom depth and stratification only), case 2) with the observed barotropic currents, and case 3) with both barotropic currents and

vertical shear.

1.3 Results

1.3.1 Context

NLIW observed during the Washington Waves experiment were relatively weak ($\eta \approx$ 10-15 m, compared to 30-40 m typical for this time of year) as can be seen in Fig. 1.3; however, most (but not all) waves still appeared at the leading edge of the onshore phase of the internal tide as is typically observed [*Alford et al.*, 2012]. In 2014, the "fall transition" from summer (upwelling) to winter (downwelling) conditions occurred quite early when on August 28 winds and along-shore barotropic currents at Cha'ba reversed (Fig. 1.3). Shortly thereafter, tidally-averaged D_2 energy flux at Cha'ba rotated from NNE towards ESE. During this time period, the magnitude and direction of $\langle F_w \rangle$ tracked $\langle F_{D_2} \rangle$ suggesting a correlation between the two in spite of changing internal tide direction.

1.3.2 NLIW generation at the shelf break

Partial reflection of the incident internal tide

Shipboard data collected along the generation section (line AC) demonstrated partial reflection and partial transmission of the incident internal tide. Harmonic analyses of 24 virtual stations (Fig. 1.4a,b) explained 55-70% of the total baroclinic velocity variance (Fig. 1.4c). Low-mode signals offshore became dominantly mode 1 inshore of the shelf break. Animations of the semi-diurnal solutions (supplementary material) showed a pulse of eastward phase propagation near the surface. After that pulse reached the shelf break region, a westward propagating signal at 150-200m depth was apparent. The pattern was consistent with partial reflection of incident signals at the shelf break and forward transmission onto the shelf.

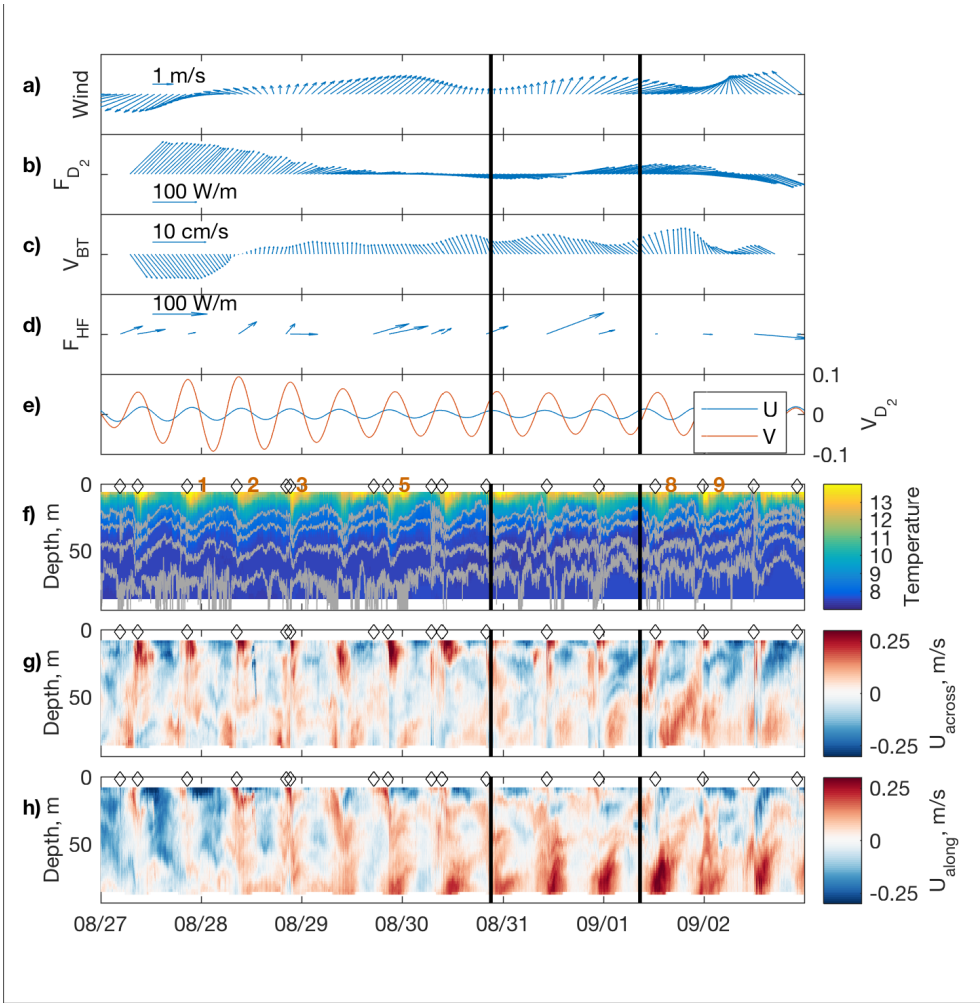

Figure 1.3: Mooring observations, including (a) 3-day winds from LaPush and (b) tidally-averaged D_2 energy flux, (c) barotropic velocities, and (d) NLIW energy fluxes, and (e) barotropic tidal currents from Cha'ba. (f) Temperature with isopycnal contours, and (g,h) across- and along-shelf velocities are shown with black diamonds to indicate NLIW events at Cha'ba. Black solid lines bracket the time period during which line AC was occupied. Orange numbers indicate the waves observed in wave chases.

To quantify this qualitative result, tidally-averaged, depth-integrated energy flux density, F and $c_g E$ at each location were compared (Fig. 1.5a). Group speeds of $c_g = 0.27\text{m s}^{-1}$ offshore decreased to $c_g = 0.17\text{m s}^{-1}$ on the eastern end of the line. Moving over the shelf break, the ratio of F to $c_g E$ increased sharply, suggesting a transition from partly standing to progressive waveforms there. Results of the mode-by-mode calculation suggested the same: offshore, the ratio of c_g^{obs} to c_g^{th} was for all modes much less than one; onshore, the ratio was 1 ± 0.2 for all

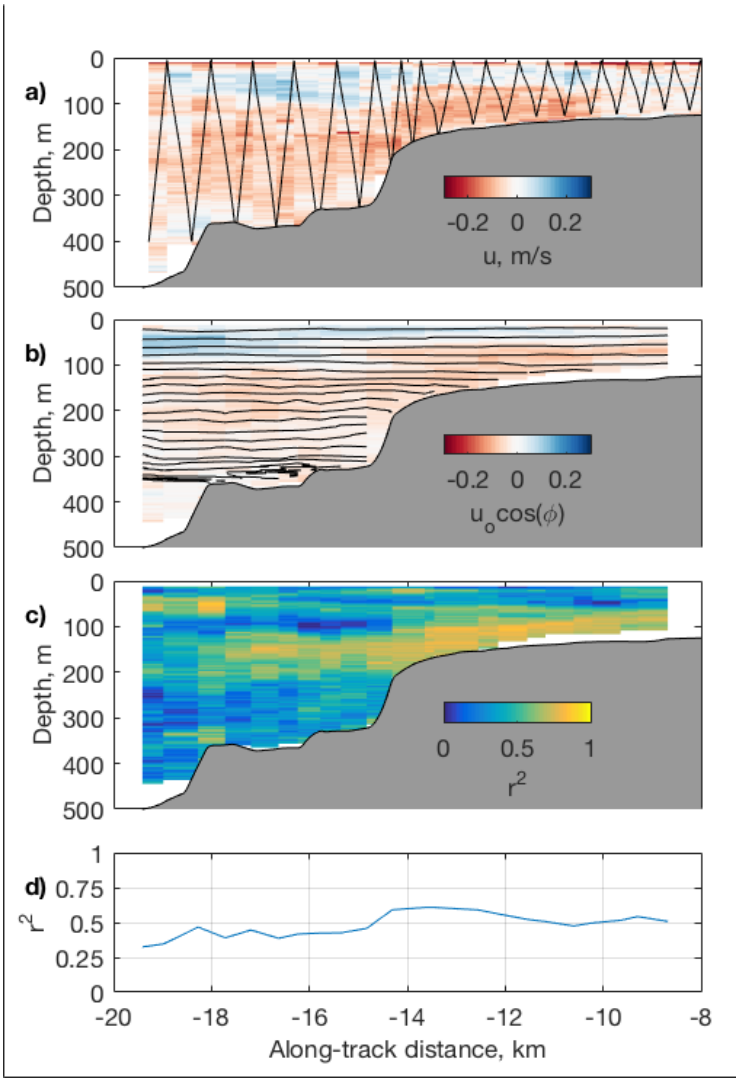

Figure 1.4: Harmonic analysis of line AC. Raw velocity data from a single section with SWIMS sampling tracks is shown in (a). Panel (b) shows the D_2 velocity reconstructed from harmonic fits for the phase of the internal tide corresponding to the observations shown in (a). Average percent variance explained by the harmonic fits at each location is shown in (c).

modes (not shown) except for mode 2 whose ratio was 0.7±0.3. In addition, the ratio of HKE to APE at each offshore station was well below the theoretical ratio (3.88) for progressive linear D_2 internal waves at this latitude, but the ratio increased to closer to the expected value beyond the shelf break (Fig. 1.5c) suggesting progressive waveforms there [*Hall et al.*, 2014]. Taken together, these results provide the first clear evidence that the incident internal tide is partially

reflected, leading to lower net flux and partly standing waveforms offshore and progressive tidal waveforms over the shelf.

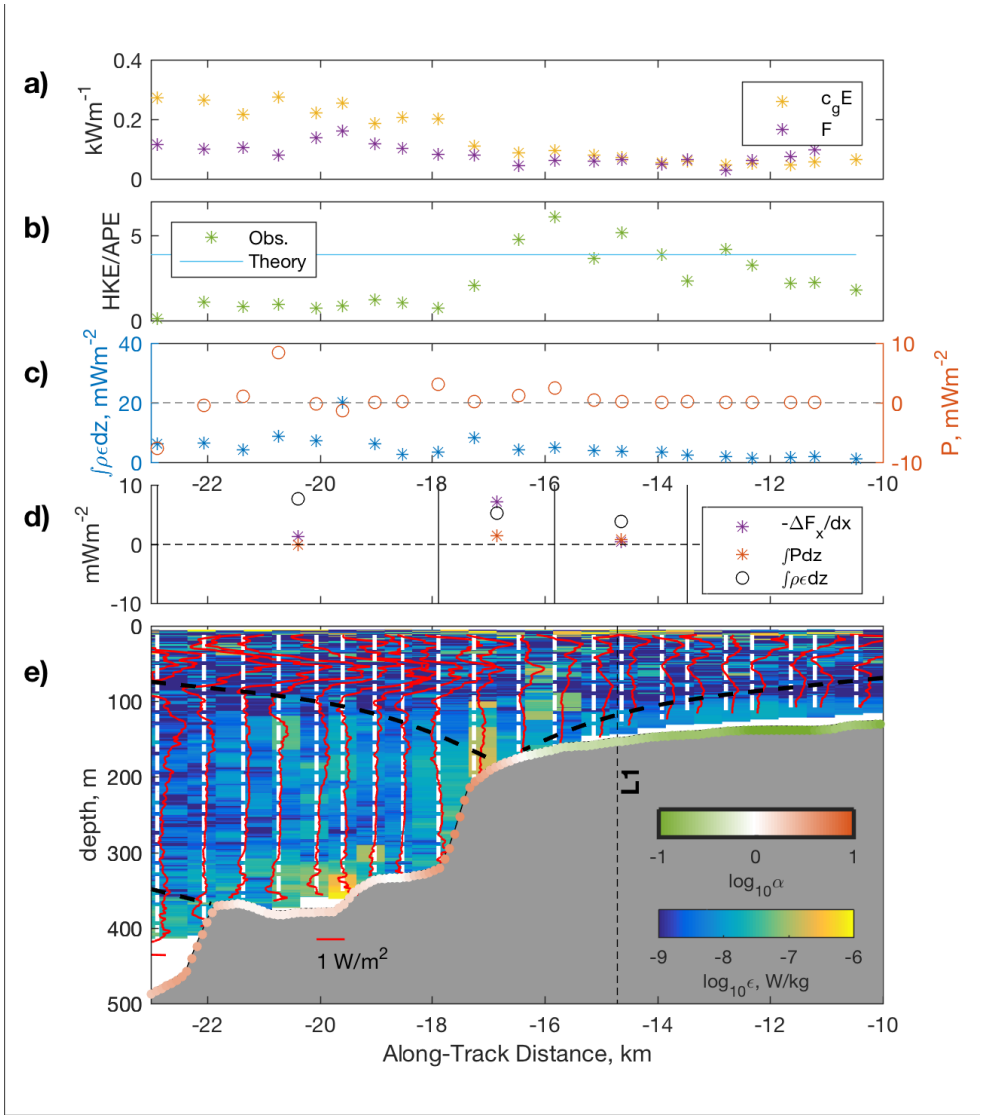

Figure 1.5: Generation section. (a) c_gE and F; (b) HKE/APE; (c) Depth-integrated dissipation and production; (d) along- and across-shelf flux convergence, production, and dissipation of TKE integrated over depth and one D_2 tidal cycle and over the control volumes indicated with vertical black lines; (e) Profiles of on-shore tidally-averaged cross-isobath energy flux (red lines), D_2 internal wave characteristics (thick dashed black), tidally-averaged dissipation inferred from Thorpe scales (background color), location of L1 (black dashed), and criticality of the bathymetry along line AC (colored dots).

Shelf-break energetics

Semi-diurnal signals along line AC were also used to assess a cross-shelf energy budget and to estimate the proportion of incident D_2 energy transferred to the NLIW frequency band. Vertical profiles of the observed cross-shore energy flux, $\langle F_{xs} \rangle$, are shown for each location in Fig. 1.5e. Flux is generally surface-intensified as expected. Over the shelf flux is onshore with more complicated structure to the west. Time mean dissipation (Fig. 1.5e) shows some near-bottom turbulence near kilometer -20 and near the shelf break (km -15-16), giving peaks in depth-integrated dissipation at those locations (Fig. 1.5c).

The measured terms in the cross-shelf energy budget (Eqn. 3.7) are shown in Fig. 1.5d for three segments of line AC (loosely "offshore," "shelf break," and "shelf," delineated by vertical black lines). Crossing the shelf break, net flux decreases from 106 ± 19 Wm^{-1} to 62 ± 11 Wm^{-1}, and dissipation approximately balances the flux convergence transiting the shelf. Offshore and shelf dissipation exceeds the small flux convergence, which implies that dissipation had other causes (e.g. mean and/or near-inertial flows).

Flux increases to a value of 133 ± 52 Wm^{-1} at the far east end of the generation section. Assuming that along-crest NLIW fluxes are uniform and that crests roughly align to follow isobaths, this value may be considered as the tidal energy flux available for the generation of NLIW. During this period at Cha'ba, the sum of the tidally-averaged cross-isobath component of D_2 energy flux ($\langle F_{D_2} \rangle = 65 \pm 9$ Wm^{-1}) and in the NLIW band ($\langle F_{HF} \rangle = \langle c_g E_w \rangle$ = 36 ± 11 Wm^{-1}) is slightly less than the D_2 energy flux seen at the eastern extent of line AC, consistent with nonlinear transformation of the shoaling internal tide as a generation mechanism. As a fraction of the semi-diurnal energy flux available at the generation site, approximately 30% of the transmitted energy is transferred into the high frequency NLIW band.

Connection to inshore NLIW observations

Information from the generation section was also used to contextualize the eventual appearance of NLIW and their phasing relative to the internal tide (Fig. 1.6a). As mentioned above, little phase propagation in flux was observed west of the shelf break, but it was evident to the east. The phase propagation continued as indicated in upper-layer velocity (Fig. 1.6a, orange lines), where the maximum onshore velocity at Cha'ba lags 2.5 hours behind that at L1, approximately consistent with propagation at the linear mode 1 speed computed from the local depth and stratification (blue dashed). Only one weak NLIW was seen west of Cha'ba, with most waves occurring at the time of onshore upper-layer flow there and propagating eastward at nearly the mode 1 speed. Though the shipboard sampling (gray dots) was purposely biased toward the portions of NLIW-containing phase space, no waves were seen at times other than ± 2 hours from the expected arrival time (blue dashed) extending from the Cha'ba maximum shallow flow time. The phasing was consistent with formation through steepening of the internal tide, as is found in other regions with the same generation mechanism [*Zhao and Alford*, 2006].

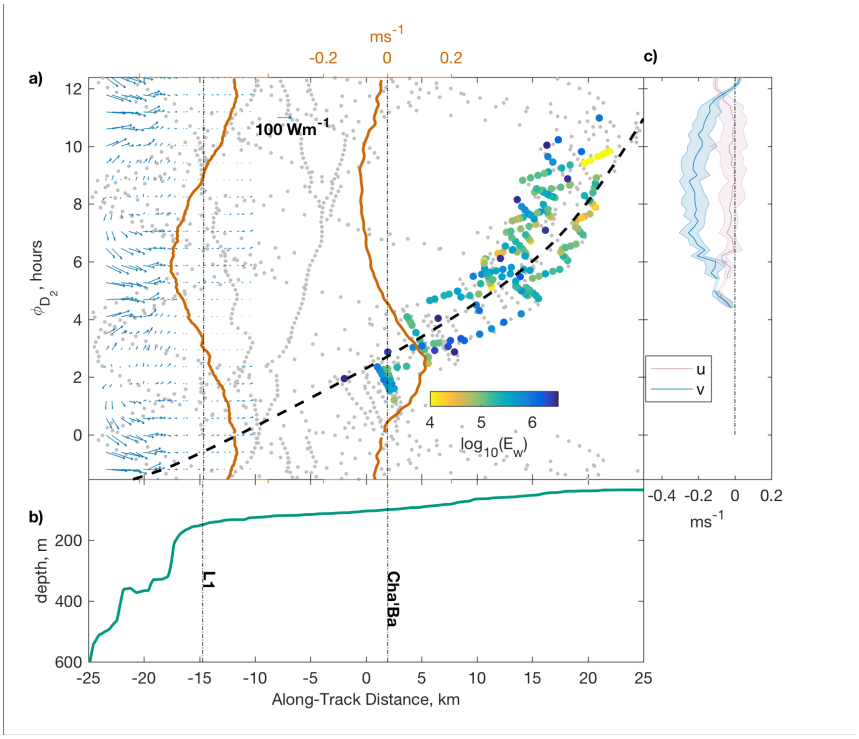

Figure 1.6: Wave properties in space and time. (a) Composite plot of cross-shelf location vs phase (ϕ_{D_2} = baroclinic internal tide at Cha'ba) for each set of wave observations. Colors indicate the energy of each crest. Solid orange lines denote phase-averaged surface currents observed at L1 (left; 0-60m) and Cha'ba (right; 0-40m) over the course of the experiment. The dashed black line is the projected path for a mode-1 linear internal wave in the observed stratification and is offset in phase space to fit the observations. Blue arrows indicate the magnitude and direction of the D_2 energy flux along line AC (determined from harmonic fits). Grey dots indicate the ship's location and coverage of phase space. (b) Bathymetry along line AB. (c) The average (lines) and standard deviation (shading) of all barotropic currents observed east of 15km are plotted versus D_2 phase.

1.3.3 NLIW propagation and dissipation over the shelf

Inshore of the generation section, data from shipboard surveys were used to examine the characteristics and evolution of NLIW transiting across the shelf. Five waves were followed, and their evolution was documented beginning with detection at the Cha'ba mooring. Prior to discussing general aspects of their evolution, Wave 5, which was sampled with SWIMS, is first presented as an example.

Case study: Wave 5

As it passed Cha'ba, Wave 5 appeared as an undular bore propagating at 60° true, with five oscillations of 500-800m wavelength (not shown). By the time the ship made its first pass through the leading edge (17km from Cha'ba), these 5 irregular undulations had steepened and formed a rank-ordered wave train, with higher-amplitude crests at the leading edge. On the second pass, the train encountered a southward background current that increased in both strength and shear moving onshore (profiles, Fig. 1.7c,d) and was in part due to the barotropic tide (demonstrated below). By pass 3, additional wave crests began to appear. Moving inshore of the 40m isobath, wave amplitudes became increasingly less ordered, and individual waves became difficult to distinguish from one another. A wave of elevation was observed beyond pass 5. Over the observed lifetime of the wave, its propagation direction rotated clockwise from ~60° to ~120° true (Fig. 1.7f). This southeastward propagation direction was also observed for Wave 9, during which time surface conditions allowed for radar imaging of the crests as shown in Fig. 1.1c.

Turbulent dissipation estimated from temperature microstructure (Appendix) within the wave (Fig. 1.7e) was concentrated near the sheared interface, as *Zhang and Alford* [2015] found for most waves using Thorpe scales, and in a series of sheared layers below the primary interface—a newly observed phenomenon. The wave itself did not induce additional shear layers; rather, these layers were subducted from an already sheared background state. As strong turbulence was not observed at the sheared interfaces before the waves passed, it seems that the additional

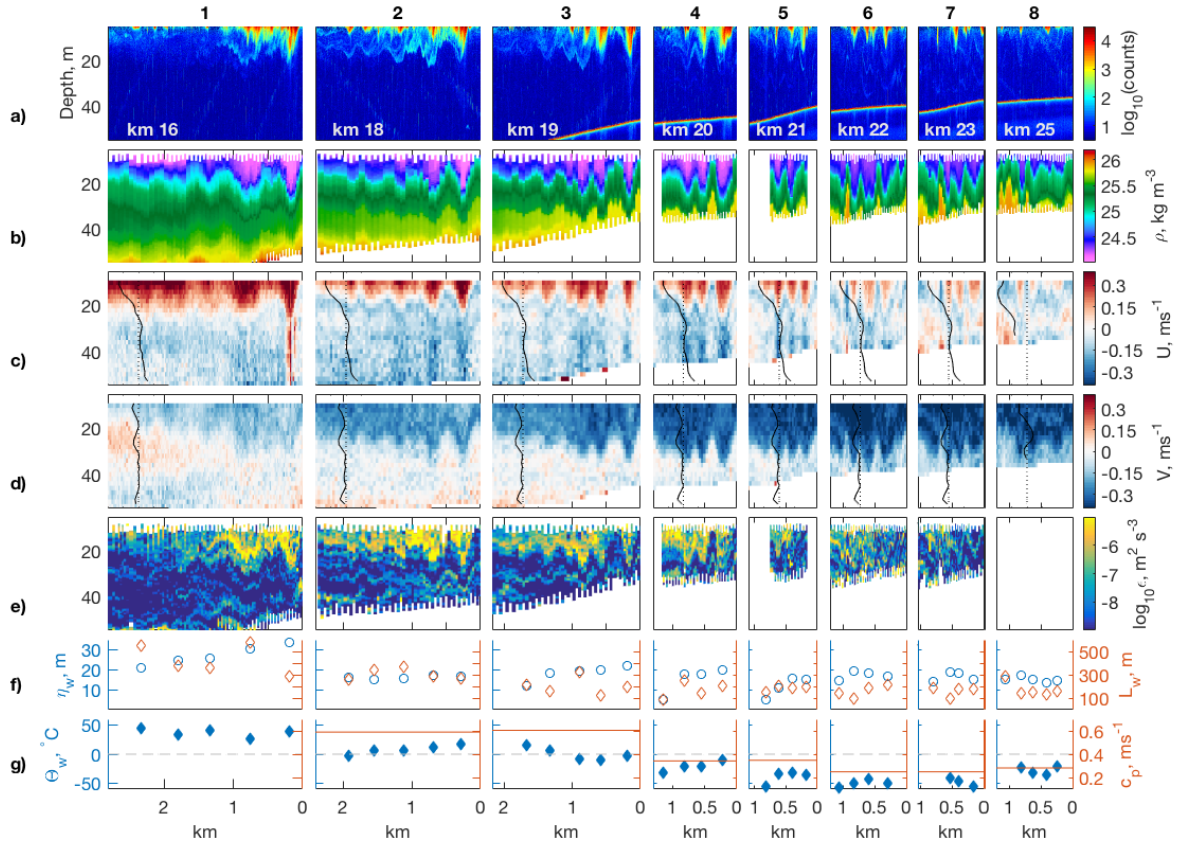

Figure 1.7: Wave 5 properties. Sections of (a) echo-intensity, (b) density, (c) zonal and (d) meridional velocity, and (e) dissipation. Panels (a), (c), and (d) are from shipboard instruments; (b) and (e) are taken from SWIMS. The bottom panels shows amplitude (f; blue circles), wavelength (f; red diamonds), and propagation direction (e; blue diamonds) for each crest. For each pass, the phase speed (e; red line) and background velocity profiles from the nearest 10-15 minute time period without wave crests (c,d; black lines) are shown. Distances on the x-axis are in units of kilometers from the leading edge; distances labeled in panel (a) represent along-track distance as indicated in Fig. 1.2.

strain caused by compression of opposing layers led to instability and breaking. Turbulence for Wave 5 appeared to be strongest in the second wave in the train, though it was not the largest, and generally decreased moving eastward as the wave amplitude and shear decreased.

In concert with the decreasing trend in the crests' amplitudes and wavelengths, integrated wave energy tended to decrease as the wave propagated onshore (grey lines; Fig. 1.8c). From the first pass to the second, the energy of each crest decreased (Fig. 1.8d; colored circles), and the

overall decrease in energy was closely balanced by the integrated dissipation (Fig. 1.8d; colored stars). However, after the second pass the energetics became more complicated. Some crests gained while other crests lost energy, and the observed dissipation for a given crest was frequently much greater or much less than that needed to account for its change in energy. That the overall energy generally decreased from pass to pass while individual crests gained energy suggests energy exchange occurred between the crests, along the crest, or with the ambient flow. Passes 6 and 8 both saw an overall increase in energy. Since our track was not aligned perfectly with the propagation direction, along-crest variations in energy created uncertainty—a problem that was common to all wave chases.

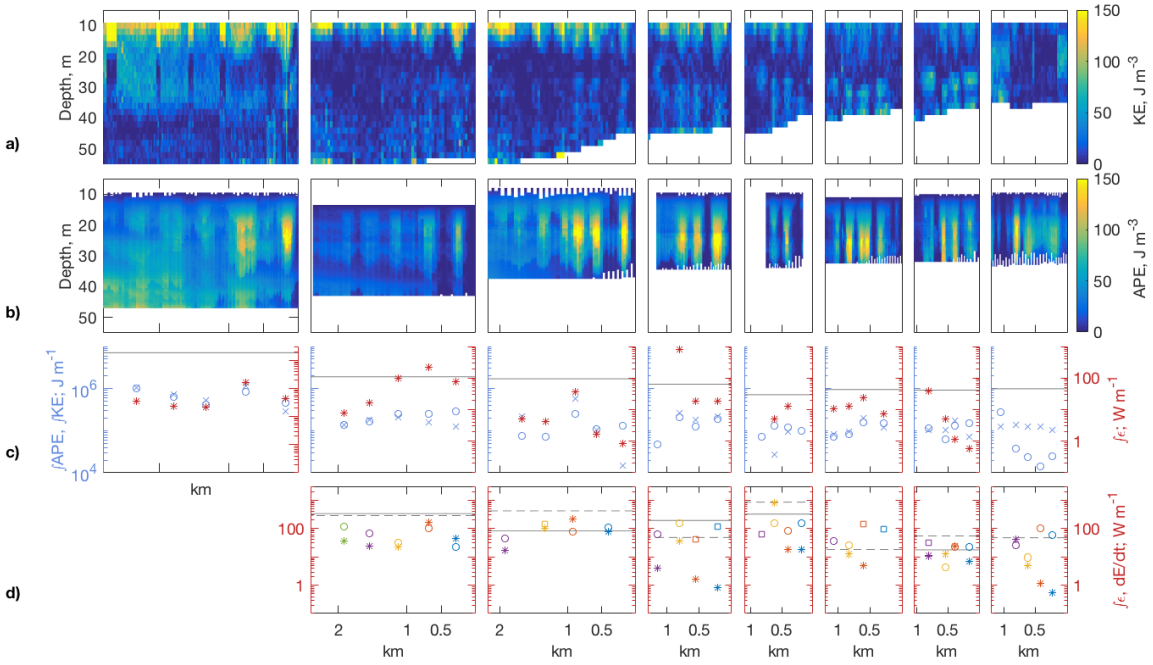

Figure 1.8: Wave 5 energetics. Sections of (a) kinetic and (b) available potential energy and (c) each crest's integrated APE (blue cross), KE (blue circle), dissipation (red star), and the sum of APE and KE for all crests in a given pass (solid grey line). Panel (d) compares pass-to-pass change in energy (circles indicate convergence $-\frac{dE}{dt}$; squares indicate divergence) and the integrated dissipation (stars) for each crest. Each wave is assigned a color that is consistent for each panel in row (d). The solid and dotted grey lines show the total decrease in energy ($-\frac{dE}{dt}$) and integrated dissipation, respectively, from pass to pass. If no solid line is present, the total energy increased from the previous pass.

Evolution over the shelf: wave composite

Having considered Wave 5 in detail as a case study, the properties of all observed waves are next viewed in aggregate. Moving eastward from their apparent formation near Cha'ba, seven waves were tracked, as shown in Fig. 1.2. Of these, five were able to be followed inshore of the 60m isobath. These waves were qualitatively distinct from each other, but they largely fell into categories of "bore-like" and "train-like" waves. Waves 2, 3, and 5 were train-like, but Wave 2 did not exhibit rank-ordered behavior. Waves 4 and 8 began as undular bores, and abruptly lost much of their high-frequency, undular character at the 80m and 40m isobath, respectively. Despite these differences, several patterns were apparent. As was the case with Wave 5, train-like waves 2 and 3 generally lost energy and rotated southward moving onshore. Waves 4 and 8, which began as undular bores and remained qualitatively bore-like, did not rotate noticeably or lose energy. The lack of an observable decrease in wave energy moving onshore for these waves may stem from difficulties in defining the "end" of a bore.

These findings were summarized by binning energy, amplitude, wavelength and propagation direction versus distance for bore-like (Fig. 1.9, red) and train-like waves (blue). Energy and amplitude decreased moving onshore and did so much more dramatically for train-like waves (Fig. 1.9a,b). Wavelengths decreased from 400-800 m (near Cha'ba) to less than 100 m (20 km inshore) for trains, with only a slight decrease for bores (Fig. 1.9c). (The undular front end of the bores gave artificially low wavelengths for some of them in this calculation). Finally, wave trains turned clockwise from a mean direction of about 30° N of E to about 30° S of E over the 20-km tracking range, while bores did not measurably turn (Fig. 1.9d). A median (mean) uncertainty of 16° (21°) was determined for the waves' propagation direction.

Although the conditions experienced by each wave packet varied between events, a vertically sheared, southward current was reliably observed at the eastern end of each occupation of lines AB and EF. Southward barotropic velocity increased moving onshore. Part of this apparent nearshore strengthening was the barotropic tide aliased onto our spatial sampling; southward flow

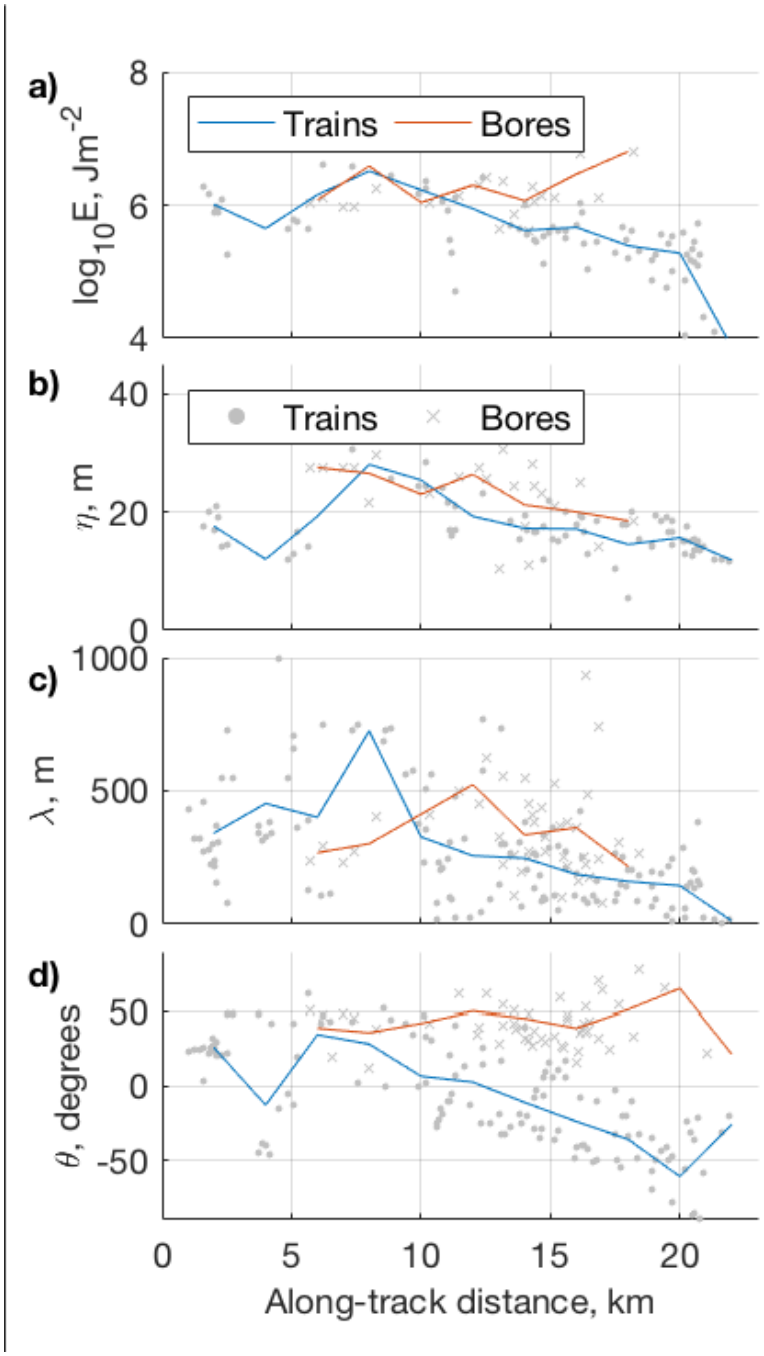

Figure 1.9: (a) Energy E, (b) amplitude η, (c) wavelength λ and (d) direction θ versus onshore distance for all wave crests (gray; dots are trains, x's are bores). Averages over 2-km bins for bore- (red) and train-like waves (blue) are also shown.

always appeared to the eastern end of our lines since the ship was always there at that phase of the tide as it tracked the NLIW. Phase-averaged barotropic velocity inshore of x=15km was southward

and sinusoidal in appearance (Fig. 1.6c); however the strength of the meridional flow inshore was stronger than that measured concurrently at Cha'ba or L1 (not shown) suggesting that a portion of the apparent increase in velocity was due to laterally sheared barotropic currents. This lateral shear occurred to the waves as a spatial gradient in their propagation medium, causing them to veer clockwise slightly in analogy to shoaling surface waves approaching a beach. Vertical shear also augmented the spatially variable barotropic flow. Offshore the upper layer flowed roughly in the direction of wave propagation such that wave speed was expected to increase and the crests to narrow [*Choi*, 2006] as observed (Fig. 1.6). Because vertical shear acts on the waves in a plane parallel to their propagation direction, as waves rotated and propagated onshore into different background flow conditions, the effects of vertical shear were also spatially variable and impacted the waves' propagation somewhat.

Comparison to linear ray tracing analysis

In order to consider whether observed changes in background velocity and shear could explain the observed clockwise rotation of the waves moving onshore, linear ray tracing was employed (Fig. 1.10). Without currents, waves were, on average, refracted minimally from their incident angle ($\pm 5^\circ$); the small amount of apparent rotation acted to steer waves slightly towards a direction perpendicular to isobaths in individual examples, but the effect was generally small. Barotropic currents caused some refraction of waves entering the flow at an oblique angle (-8°). Including shear induced slightly more clockwise rotation, but not enough to explain the observed veering (-11°; Fig. 1.9d).

1.4 Discussion

We here find that approximately 30% of the internal tide energy transmitted onto the shelf subsequently transforms into NLIW by assuming that the D_2 energy flux at the eastward end of

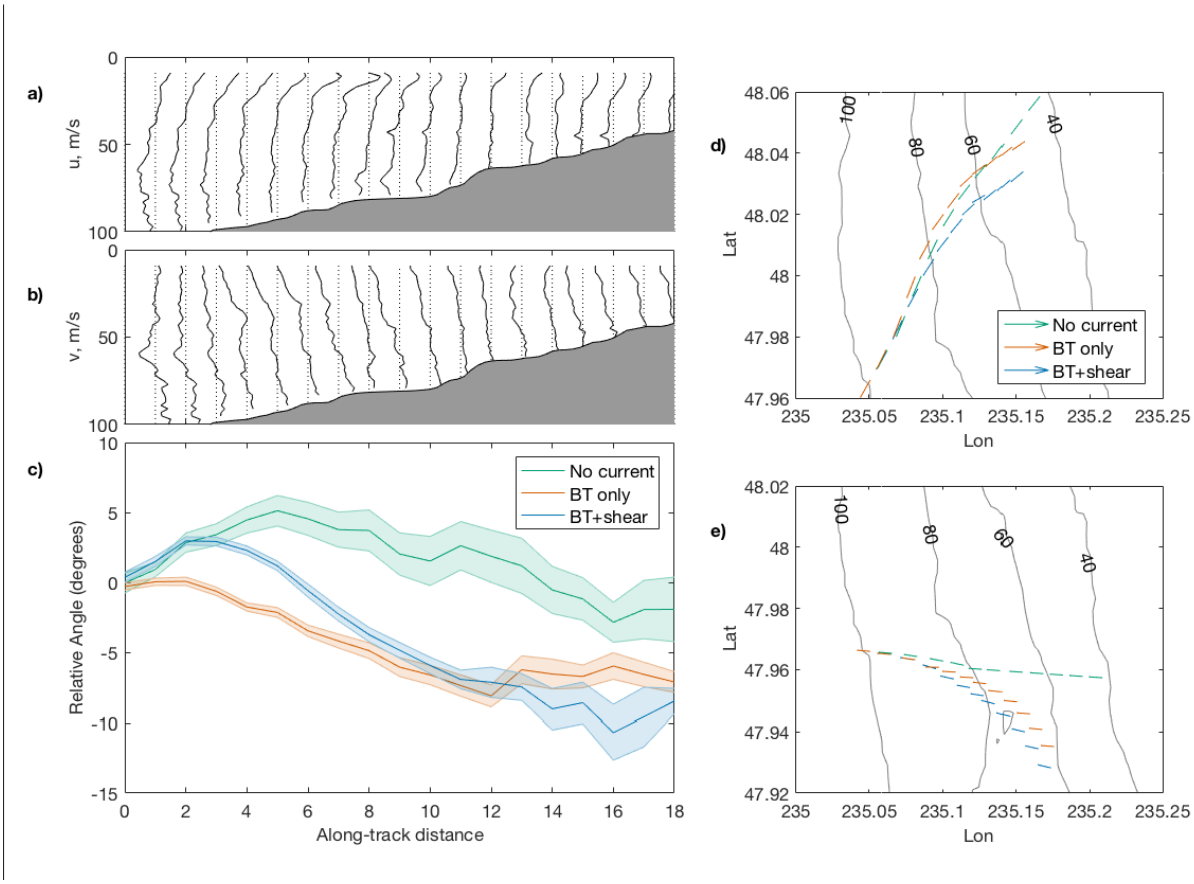

Figure 1.10: Results from Taylor-Goldstein analysis. Mean (a) eastward and (b) northward velocity profiles encountered by waves and (c) deviation from initial angle for all cases plotted versus along-track distance. Colored lines represent the mean rotation observed with realistic bathymetry and the observed stratification (no currents, green), with the barotropic component of the flow (orange), and with both the observed shear and current field (blue). Error bars indicate the standard error resulting from testing waves with 39 different starting angles for each case. For all three cases, vectors indicating the midpoint and direction of wave crests with an initial propagation angle of (d) 45° and (e) -5° N of E changing over 12 hours.

the generation section was available for transformation into the high frequency NLIW band. This assumption is in part based on the fact that the onshore energy flux over the shelf increases to a maximum at the eastward end, but it is important to note that uncertainty is larger here due to poorer coverage of phase space at the ends of line AC. The apparent flux increase may also be due to the interaction of barotropic and baroclinic tides which can alter time-mean isopycnal

displacements at a fixed location as discussed by *Stephenson et al.* [2016]. However, at this location the tidal excursion length scale (defined as the ratio of the amplitude of the barotropic tide to the speed of the baroclinic tide) is very small ($\approx$0.08) so that this interaction and thus the impact on the results of harmonic analyses should be small.

Although the 36-hour time series undertaken in this study provides only a single offshore snapshot, offshore stratification that alters the reflectivity of the shelf-break could govern the IT energy available to NLIW and thus their inshore properties. Changes in offshore stratification (such as the anomalous "blob" conditions observed in Autumn 2014-2015 [*Bond et al.*, 2015]) would alter both the wave guide and the reflectivity of the coastline and control both the source and magnitude of the transmitted IT energy.

Although slight rotation of onshore propagating NLIW has been observed using an array of pressure sensors inshore of Stellwagen Bank in Massachusetts [*Thomas et al.*, 2016], at this location waves rotate 60° or more over the course of 20 kilometers as seen in imagery (Fig. 1.1c) and in situ (Fig. 1.7g). Although the sense of the rotation matches that determined from linear ray tracing analysis, the majority of the observed veering is not accounted for and so the result warrants further discussion.

One scenario possible in this environment is that waves propagate into the study region from a different source. Given the serpentine nature of the shelf break in this region (Fig. 1.1; 200m isobath, for guidance) and the finding that NLIW arise from nonlinear transformation of the internal tide impinging upon it, we might expect waves to propagate in different directions depending on the piece of shelf-break at which they formed. The shelf break curves inward to the north and south, so it is possible that waves generated at a later time and at a different location propagate shoreward over a shorter distance to interfere further inshore with those that have passed by Cha'ba. For example, some SAR images reveal NLIW propagating southward from the Juan de Fuca Canyon $\sim$10 km north of Cha'ba. The SAR image shown in Fig. 1.1, too, contains some crests nearer to shore that are oriented in a more southward direction than the

main wave packet. This explanation would account for waves arriving at Chaba out of phase with the local baroclinic internal tide, but only two irregular events were recorded at Cha'ba during this experiment, and both passed by the mooring several hours *before* the tracked waves. Given that we tracked each wave from the mooring shoreward, the interference of a wave from another source would be unlikely.

Since we were unable to determine our along-crest position on all but one wave event, a more likely scenario is that the ship actually slid laterally along wave crests as they propagated inshore. Such a sampling pattern would have captured both temporal evolution and along-crest variability rather than temporal evolution of the wave train at a given along-crest location. This could have caused waves with strong curvature to show up as rotating crests. Based on historical satellite imagery, the range in propagation direction at different locations along a given NLIW crest is on the order of 30° so that this could explain the observed veering within error bars [*Liu et al.*, 1985; *Jackson and Apel*, 2004]. However, because our ship track was aligned in a direction more northerly than the propagation direction of the waves observed at Cha'ba, the effect of sliding laterally should have resulted in computed propagation directions turning more and more to the *north* moving inshore—not to the south. If lateral sliding did occur, we could also expect that wave properties such as amplitude would decrease with along-crest distance from the crest's midpoint, and that the observed wave energy would not be particularly useful for computing pass-to-pass wave energy budgets as examined in this work. However, the intriguing finding that the decrease in wave energy was balanced by dissipation from pass 1 to pass 2 through Wave 5 appears valid given that at this point the ship was still roughly aligned with the propagation direction (Fig. 1.7).

Reflecting on the details of Wave 5's evolution leads to further speculation on the mechanisms leading to the observed veering of wave trains. During these first two occupations the wave-train was well-behaved and rank-ordered. However, as the wave approaches the "turning point" (where bottom depth is less than twice the amplitude of the leading wave) at the 45m

isobath around pass 3, the energetics of individual wave crests are much less straightforward with some crests gaining and others losing energy from pass to pass. Both laboratory and numerical experiments investigating NLIW evolution over shoaling bathymetry have demonstrated that the "turning point" should complicate a wave train by spawning additional crests or reversing the wave's polarity [*Helfrich and Melville*, 2006], but none have done so in 3 dimensions such that along-crest exchange of energy is permitted. If such along-crest exchanges occurred and thereby altered the amplitude and phase speed at different points along the wave crest, they could induce veering. Intuitively it seems that such exchanges would act to align crests with the isobaths, but the sheared background state complicates the matter. That significant rotation is only observed for train-like (and not bore-like) NLIW is noteworthy and may fit with this theory in that bores (with their shock-like wave fronts followed by a turbulent head) may not be subjected to the same along-crest (or crest-to-crest) energy exchanges that accompany wave-train evolution over a shelf with slowly varying depth.

That in this study three-dimensional exchanges would have a greater affect on propagation direction than bathymetric steering may be due to the particularly flat nature of the WA continental shelf. In regions with steeper bathymetric gradients, refraction by oblique currents and the influence of vertical shear on slowly evolving wave trains may be less influential than bathymetric steering. For example, a high resolution 3D model of NLIW in a long, narrow domain demonstrates how NLIW are readily refracted by steep sidewalls and topographic features (*Boegman and Dorostkar* [2011]). However, understanding the relative importance of parameters such as bathymetric gradients, lateral and vertical shear, lateral changes in stratification, and three-dimensional effects will rely on the validity of the available models; as yet, the behavior of strongly nonlinear waves in sheared currents is not well described.

1.5 Conclusions

This work describes the generation and spatial characteristics of nonlinear internal waves in the complex flow environment off of Washington state. The conditions during the study period are not "typical" of summer conditions during which large NLIW (with amplitudes around half the water depth) are regularly observed. While internal tide energy fluxes are similar to the summertime mean, their direction changes during our sampling with the onset of the fall transition. Despite this change, NLIW continue to appear at the leading edge during the onshore phase of the internal tide and have energy correlated with and initial direction similar to that of the internal tide adding to the growing body of evidence that many coastal NLIW arise from nonlinear transformation of remotely generated internal tides impinging upon the slope. Observations made near the hypothesized generation region suggest that the incident baroclinic tide is partially reflected and partially transmitted at the shelf break. Approximately 30% of the transmitted energy is transformed into NLIW observed further inshore.

Waves are tracked as they propagate into a complex laterally and vertically sheared southward current over the continental shelf. Bore-like waves lose less than 10% of their initial energy observed at Cha'ba and propagate at a nearly constant angle. Train-like waves, on the other hand, lose 80% or more of their energy as they propagate inshore. As they enter the sheared southward current, crest-to-crest energy exchange becomes complicated, additional waves spawn, and the train rotates clockwise. Some trains rotate over 60° over the course of the onshore propagation. The rotation is not consistent with bathymetric steering, and a linear ray tracing analysis to incorporate the effects of lateral gradients in the barotropic flow and vertical shear explain only a fraction of the observed rotation. It is likely that in this relatively flat coastal environment with complex currents, dynamics in three dimensions are required to explain the observed behavior and understand the influence of NLIW over the continental shelf.

1.6 Acknowledgements

This chapter, in full, is a reprint of the material as it appears in Journal of Geophysical Research: Oceans, 2018. Hamann, Madeleine M.; Alford, Matthew H.; Mickett, John B., 2018. The dissertation/thesis author was the primary investigator and author of this paper.

Funding for this work was provided by the Office of Naval Research under grants N00014-15-1-2284 and N00014-13-1-0390. The considerable hardware and instrumentation comprising the surface and subsurface moorings were purchased on a generous grant from the Murdock Charitable Trust. The captain and crew of the R/V Oceanus and the technical skills of Mike Goldin, Dave Winkel, Sam Fletcher, and Jonathan Ladner were instrumental in the success of this field campaign. We thank the Captain and crew of the R/V Thomas G. Thompson for deploying and servicing the moorings; Eric Boget, Mike Carpenter, Sam Fletcher, Mike Kenney, Trina Litchendorf, Keith Magness, Tim McGinnis, Nick Michel-Hart, Zoe Parsons, Chris Siani, and Tim Wen for the design and construction of the NEMO systems; and especially John B. Mickett for his incredible efforts and energy in developing and maintaining them. We also thank the U.S. Coast Guard station in La Push, Washington, for their hospitality and willingness to host our shore data station; Quileute for their tribal support in onshore loading; Jennifer Hagen for her contribution during cruises to deploy/ recover ChaBa; and the Olympic Coast National Marine Sanctuary for their assistance and cooperation in buoy logistics.

The code used to process temperature microstructure from the Chiometer was modified from code provided by Johnathan Nash, for which the authors are deeply thankful. J. Nash, Emily Shroyer, and Shuang Zhang also provided helpful discussions and input that greatly enhanced the quality of this manuscript. We thank Chris Jackson for locating and sharing the SAR imagery shown here. We appreciate the time and effort of two anonymous reviewers and their comments that greatly enhanced the quality and clarity of this work.

Shipboard data for this experiment can be found at DOI:10.7284/900720 and mooring

data can be found at www.nanoos.org/nvs.

Chapter 2

A reflecting, steepening, and breaking internal tide in a submarine canyon

2.1 Introduction

Submarine canyons are common features along the ocean's margins, incising up to 20% of the global coastline [*Hickey*, 1995]. They are natural conduits that connect the open ocean to shallow waters, acting as pathways for enhanced cross-shelf exchange and channelling nutrient-rich waters into coastal ecosystems [*Allen and Hickey*, 2010]. These waters fuel elevated local primary production as demonstrated by numerous observations of an abundance of life at a range of trophic levels within and around canyons [*Bosley et al.*, 2004; *De Leo et al.*, 2010; *Vetter*, 1994].

Complex topography in canyons hosts dynamical processes on a variety of scales – enhancing upwelling, channelling sediment-laden gravity flows, forcing hydraulic jumps over abrupt bends, and focusing internal waves, to name a few [*Hickey*, 1995]. Many of these processes are associated with small-scale turbulence so that canyons are also "hotspots" of mixing that set the properties of onshore flows [*Alford and MacCready*, 2014; *Carter and Gregg*, 2002; *Lee et al.*,

2009].

In the small number of canyons studied to date, observed turbulent dissipation rates (ε) and diapycnal diffusivities (κ) are up to 10^3 times greater than those observed in the open ocean [*Kunze et al.*, 2002; *Lee et al.*, 2009; *Zhao et al.*, 2012; *Wain et al.*, 2013]. Similar levels of dissipation are anticipated for the many canyons that have not been directly observed, implying canyon-induced mixing is an important contributor in the energy budget and circulation of the global ocean. *Kunze et al.* [2012] extrapolate from their measurements that canyons contribute to diapycnal transport 2-3 times that of the open ocean (with an open ocean diffusivity of 10^{-5} m^2 s^{-1}), or 10% of that required to balance the rate of bottom water formation at the poles.

The distribution of canyons and associated diapycnal transport along coastlines is highly heterogeneous [*Harris and Whiteway*, 2011]. *Friedrich et al.* [2011] and *Melet et al.* [2013] demonstrate that global stratification, meridional overturning circulation, atmospheric circulation and primary productivity in global models are highly sensitive to distributions of parameterized mixing at the margins. In addition to the lateral heterogeneity that canyons induce, the wide variety of processes that arise in canyons, generating turbulence at different depths, may alter the *vertical* distribution of mixing along the continental shelf. Changes in this vertical distribution cause the greatest discrepancies in model results [*Melet et al.*, 2016]. Despite their likely influence, incorporating canyons into global models remains elusive. The grid size of such models is too coarse to resolve the scales at which canyon-related dynamics act, and our understanding of such dynamics is as yet insufficient to provide usable parameterizations.

One aspect of canyon dynamics that is of interest is the interaction of internal waves (IW) and tides with canyon topography and the associated turbulent activity. Upon encountering an obstacle, an IW's behavior depends upon both its characteristic slope (S_w) and the slope of the impacted feature (S_b). A steep obstacle ($\frac{S_w}{S_b} < 1$) is considered to be "supercritical" and causes the wave to reflect backward, leading to standing wave patterns. Gentle bathymetric slopes ($\frac{S_w}{S_b} > 1$, subcritical) allow the wave to reflect forward. Critical slopes ($S_w = S_b$) are generally

associated with breaking and near-bottom vertical mixing [*Ivey and Nokes*, 1989]. While the slope of bathymetric features remain fixed, the characteristic slope of IWs are set by their intrinsic frequency, ω, the Coriolis parameter, f, and the ambient stratification, N^2. Inherent variability of these parameters can affect changes in IW behavior. For example, *Zhao et al.* [2012] and *Hall et al.* [2014] demonstrate that in a single location, IWs of the same frequency transition between progressive and partially standing due to varying stratification. Similarly, S_w changes betweens IWs as ω varies, so that distinct frequency bands can interact with a single feature differently.

In a simplified sense, theory predicts that the steep walls of canyons should reflect incident waves toward the sea floor [*Hotchkiss and Wunsch*, 1982]. Along the canyon axis, if the slope is subcritical to the internal wave it should reflect forward, allowing energy to shoal and focus towards the canyon head where it may dissipate due to wave breaking. Such incident internal waves include the diurnal (D1) and semidiurnal (D2) tides (the combination of the K1/O1 and M2/S2 constituents, respectively). For example, in Monterey Canyon (whose axis during upwelling conditions is subcritical to the most prevalent internal wave frequency – D_2), observed ratios of horizontal kinetic energy (HKE) to available potential energy (APE) are consistent with a progressive D_2 internal wave [*Zhao et al.*, 2012]. Furthermore, turbulent mixing is enhanced, especially near the canyon head [*Carter and Gregg*, 2002; *Kunze et al.*, 2002; *Wain et al.*, 2013]. In canyons where bottom slopes along the axis are steep (supercritical), incoming internal waves should reflect back towards the open ocean. Instead of focusing energy towards the canyon head to dissipate, this reflection creates standing wave patterns with nodes of velocity and isopycnal displacement offset in space [*Martini et al.*, 2007; *Zhao et al.*, 2012]. The result is a spatially variable HKE/APE ratio. However for standing and partially-standing waves, lower wave-mean HKE/APE ratios are expected compared to the theoretical prediction for freely propagating internal waves. It should be noted that this simple description of IW dynamics is instructive but incomplete: time-varying stratification and the angle of incidence of a given wave also govern its reflection, and IW dynamics in canyons are correspondingly complicated [*Zhao et al.*, 2012].

To date, only one study has attempted to observe turbulence in a supercritical canyon. It was conducted during the spring tide in Ascension Canyon. There, *Gregg et al.* [2011] observed turbulent dissipation rates that were elevated, but were only half that of the fortnightly average observed in the nearby Monterey canyon. Observations found that dissipation was most often an insignificant term in the energy budget compared to large energy flux convergences and divergences along the canyon's axis. By contrast, results from a complementary modeling study found that dissipation (considered as the residual between temporal changes in energy storage, production, and flux divergence terms) was the most important term in the canyon's energetics. Reality is likely somewhere in between these two extremes. With limited time and a goal of discovering the spatial distribution of mixing and energy fluxes within Ascension Canyon, *Gregg et al.* [2011] obtained one profile at any given station approximately once every nine hours. They concluded that neither the temporal resolution of the observations nor the spatial resolution of the model were adequate to resolve all of the relevant dynamics.

In this work, we use new observations to investigate the interaction of internal tides with topography and associated mixing in the La Jolla Canyon (LJC) branch of the La Jolla Canyon System (LJCS) off San Diego, CA. The LJC is a straight, narrow canyon whose slope is almost entirely supercritical to the D_2 internal tide (Fig. 3.1). Historical observations in the region suggest an energetic internal wave field [*Shepard et al.*, 1974; *Inman et al.*, 1976], making it an excellent site from which to expand our understanding of how canyons impact internal wave energy fluxes and turbulence. In what follows, we describe the results of the La Jolla Internal Tide experiment (LaJIT), where observations at several points along the canyon axis revealed the characteristics of the internal tide and patterns of dissipation. Measurements with high temporal resolution capture nonlinear dynamics and intermittent turbulence and allow for the estimation of energy flux and a rough assessment of the tidal energy budget.

2.2 Experiment and Techniques

This experiment was conducted over three days (December 5-8, 2014) and consisted of a shallow mooring, two shipboard profiling stations, and a Conductivity-Temperature-Depth (CTD) section along the canyon axis. The locations of these are laid out in Fig. 3.1. Two 25-hour shipboard stations were completed along the canyon axis at A and B ($\sim$0.7 and $\sim$1.5 km from the canyon head, respectively). The CTD rosette was supplemented with lowered Acoustic Doppler Current Profiler (L-ADCP; 300 kHz). Water depths of 200 m and 160 m at A and B allowed average sampling rates of 4 and 5 profiles per hour, respectively. The CTD rosette was lowered at a speed of no more than 13.3 m/min. For at least 75% of each time series at stations A and B, combined shipboard and L-ADCP observations covered the water column from 12 m below the surface to within 5 m of the bottom. For CTD data, this range of good coverage begins at 12 m from the surface for both stations, and reaches to 12 m above the bottom for Station A, 24 m above the bottom for Station B. A moored wave-powered profiler (Wirewalker; WW; [*Rainville and Pinkel*, 2001; *Pinkel et al.*, 2011]) and bottom-mounted ADCP (300 kHz) were deployed at 100 m depth at station C near the head of the canyon. The WW was equipped with CTD, oxygen, and fluorescence sensors and sampled at a rate of 3-6 profiles per hour for 54 hours. ADCP data were collected in 8 m vertical bins at 1 Hz and averaged over 30 seconds. Finally, 7 CTD profiles were taken moving offshore from C on a 5 km section along the canyon axis (locations in Fig. 3.1; measurements in Fig. 2.1).

The criticality of the LJCS shown in Fig. 3.1 was computed as

$$\alpha = \frac{s_b}{s_w} = \frac{\nabla H}{\sqrt{(\omega^2 - f^2)/(N^2 - \omega^2)}} \tag{2.1}$$

where f is the local inertial frequency, H is the water depth, $N^2 = 10^{-5}$ s^{-2} is the minimum near-bottom stratification observed, and $\omega = 12.4$ hr^{-1} is the incident internal wave frequency (D_2). The supercritical nature of the LJC is apparent both in this map and by comparing the

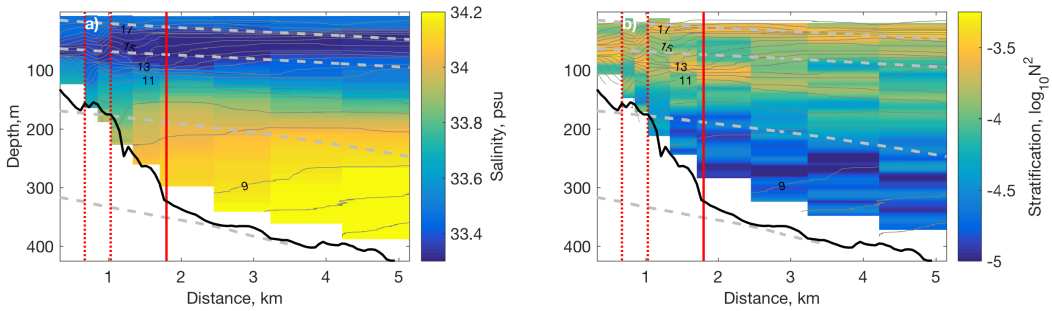

Figure 2.1: a) Salinity and b) stratification contoured with isotherms observed during the offshore section. The x axis represents distance along the thalweg from the head of the LJC. The solid black line represents the depth of the canyon axis. Dotted grey lines overlaid on both plots represent characteristics of the M_2 internal tide for the observed stratification. Dotted red lines indicate the locations of the two CTD stations (left to right, B and A). The solid red line indicates the extent of the LJC branch of the LJCS.

slope of the canyon axis to the slope of the D_2 characteristics (both shown in Fig. 2.1). It should be noted that although the LJC itself (which extends 1.8 km from the head of the system) is supercritical, the slope of the axis of the LJCS offshore of about 2 km is approximately critical, or subcritical. Increasing the assumed near-bottom stratification makes the canyon increasingly supercritical to the D_2 internal tide.

Baroclinic pressure perturbation $p'(z)$, velocity perturbation $\mathbf{u}'(z)$, and energy flux $\overline{\mathbf{F}(z)} = \overline{\mathbf{u}'p'}$, where the overbar indicates ensemble averaging over an integral number of semidiurnal periods, were calculated following the methods of *Kunze et al.* [2002], *Althaus et al.* [2003] and *Nash et al.* [2005].

Baroclinic kinetic energy density

$$HKE = \frac{1}{2}\rho_o \int_{-H}^{0} |\mathbf{u}^2(z)| dz \tag{2.2}$$

and available potential energy density

$$APE = \frac{1}{2}\rho_o \int_{-H}^{0} N^2(z)\eta^2(z) dz \tag{2.3}$$

were calculated at each station, where H is the water depth, ρ_o is the time- and depth-averaged density, $N^2(z)$ is the buoyancy frequency at the station and η is isopycnal displacement from the tidally averaged density profile.

The vertical structure of the waves was decomposed into discrete vertical modes using the observed profiles of N^2. These modes are a solution to the equation and boundary conditions

$$\frac{\delta^2}{\delta z^2}\eta(z) + \frac{N^2(z)}{c_n^2}\eta(z) = 0, \;\; \eta(0) = \eta(H) = 0, \tag{2.4}$$

where H is the water depth and c_n is the eigenspeed for a given mode, n. Modal velocities ($\mathbf{u}_n(z,t)$) and displacements ($\eta_n(z,t)$) were computed for the first four modes.

Table 2.1: Energy ratios and group speeds

	HKE/APE		Observed and Theoretical c_g							
	D_2	**Total**	$c_{g,n}^{obs}$	c_g^{th}	$c_{g,n}^{obs}$	c_g^{th}	$c_{g,n}^{obs}$	c_g^{th}	$c_{g,n}^{obs}$	c_g^{th}
Station A	0.82	**0.38**	**0.71**	2.46	**0.35**	1.23	**0.22**	0.82	**0.17**	0.62
Station B	0.51	**0.28**	**0.62**	2.11	**0.31**	1.05	**0.20**	0.71	**0.14**	0.53
Station C	0.05	**0.04**	**0.49**	1.85	**0.31**	0.92	**0.19**	0.62	**0.15**	0.46
			$n=1$		$n=2$		$n=3$		$n=4$	

Following the methods of *Martini et al.* [2007] and *Zhao et al.* [2012], the observed group speed for each mode was computed as

$$c_{g,n}^{obs} = \frac{\langle F_n \rangle}{\langle E_n \rangle}, \tag{2.5}$$

where $\langle F_n \rangle$ and $\langle E_n \rangle$ are tidal averages of the depth-integrated energy flux and energy (the sum of APE and HKE), respectively, attributed to a given mode, n. The theoretical group speed at each station was computed as

$$c_{g,n}^{th} = \left(\frac{\overline{N}H}{n\pi}\right)\frac{\sqrt{\omega^2 - f^2}}{\omega}. \tag{2.6}$$

Ratios of HKE to APE and observed and theoretical group speeds for the first four modes are given in Table 2.1.

Table 2.2: Displacement and along-canyon velocity from harmonic analysis. Parentheses indicate depth-average percentage of the total observed variance.

	Displacement RMS amplitude (m), (% variance of data)					Along-canyon velocity RMS amplitude (cm/s), (% variance of data)				
Frequency	D_2	$2D_2$	$3D_2$	D_1	**Total**	D_2	$2D_2$	$3D_2$	D_1	**Total**
Station A	17.3 **(58)**	7.2 **(17)**	3.6 (3)	5.8 (10)	34 **(88)**	7.5 **(43)**	4.4 **(17)**	2.3 (5)	2.3 (5)	17 **(70)**
Station B	14.7 **(45)**	7.9 **(19)**	2.3 (1)	9.4 (19)	34 **(84)**	6.7 **(28)**	5.4 **(20)**	2.8 (6)	2.8 (6)	18 **(60)**
Station C	13.7 **(44)**	8.4 **(17)**	2.5 (2)	4.9 (7)	29 **(70)**	2.6 **(18)**	1.6 **(7)**	1.3 (6)	1.7 (8)	7 **(39)**

Harmonic fits of u' and η at each station were calculated for the D_1, D_2, $2D_2$, and $3D_2$ tidal constituents. Due to the shortness of the time series at each station, K_1/O_1 and M_2/S_2 tidal constituents cannot be distinguished from one another, and so we analyze their respective combinations D1 and D2. Table 2.2 summarizes root-mean-square amplitudes and the fraction of observed variance accounted for by the harmonic fits. Each value of amplitude and fraction of variance in Table 2.2 is an average over the depths for which at least 80% of the time series contains data. For along-canyon velocity, these depths are $12-200$ m, $12-156$ m, and $6-110$ m for stations A, B, and C, respectively. For η, the corresponding depth ranges are $20-152$ m, $20-124$ m, and $19-77$ m. This excludes the surface and bottom depths, where the harmonic fits accounted for little variance. To facilitate comparison between the mooring and shipboard stations, harmonic analysis at station C was based on velocities that were binned by 15 minutes, approximately the average cast interval of stations A and B.

Depth-dependent uncertainty in $\overline{\mathbf{F}(z)}$ was computed as the standard error of the residual between observed, time-dependent energy flux and the energy flux calculated using the harmonic fits of $\mathbf{u}'$ and p'. This method was chosen as the residual quantifies the variance due to random noise and high-frequency motions not described by the harmonics while the standard error additionally accounts for incomplete coverage in time at some depths.

To calculate the energy flux convergence, first the energy flux was assumed to be uniform in the cross-canyon direction because fluxes were measured at a single point across the canyon at each station. Using the time-mean, along-canyon energy flux profile measured at each station

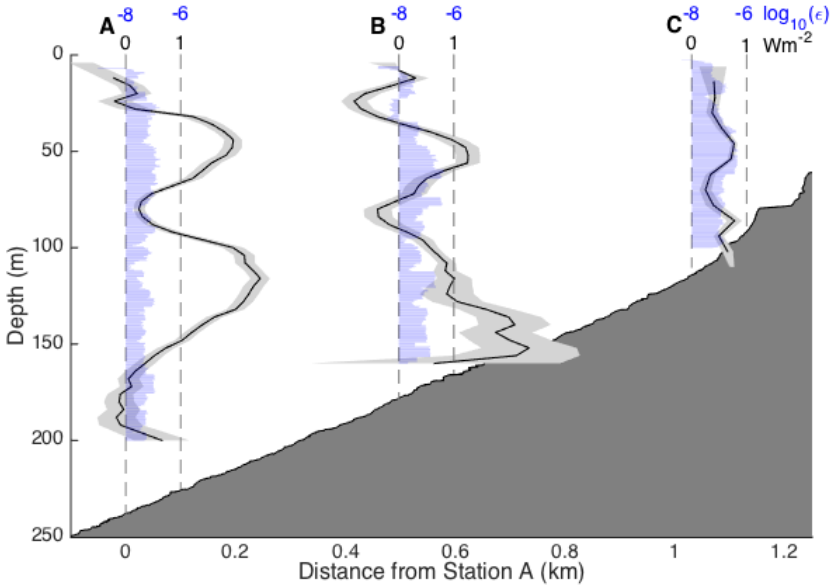

Figure 2.2: Along-canyon section showing vertical profiles of time-mean, along-canyon energy flux, $\overline{F_{ac}(z)}$ (W m^{-2}), at stations A, B and C (black curves with error estimates shaded in grey) and time-averaged estimates of turbulent dissipation ($\log_{10}$(W kg^{-1})) from Thorpe scale analysis at stations A, B and C (blue bars).

($\overline{F_{ac}(z)}$, Fig.3.8), the total along-canyon energy flux,

$$\overline{F_{total}} = \frac{1}{H}\int_{-H}^{-h} \overline{F_{ac}(z)} \cdot l(z)\, dz = \frac{1}{H}\sum_{z=-H}^{-h} \overline{F_{ac}(z)} \cdot l(z)\delta z, \tag{2.7}$$

in units of W m^{-1}, was calculated by multiplying ($\overline{F_{ac}(z)}$) at each depth by the canyon width at the corresponding depth, ($l(z)$), then integrating vertically from the seafloor (-H) to the canyon rim (-h). This method takes into account the decrease in the canyon cross-sectional area from station A to station C. Flux convergence, $-\frac{d\overline{F_{total}}}{dx}$, in units of W m^{-2}, was found by dividing the difference between $\overline{F_{total}}$ between each station by the lateral distance (dx) between each station.

Dissipation of turbulent kinetic energy (TKE) is estimated from observed density overturns following the Thorpe scale method described in *Thorpe* [1977], *Dillon* [1982], and *Gargett and Garner* [2008] (Fig. 2.5). Although these methods are indirect, past studies have shown that because most dissipation is associated with large overturns, time-averaged values of dissipation

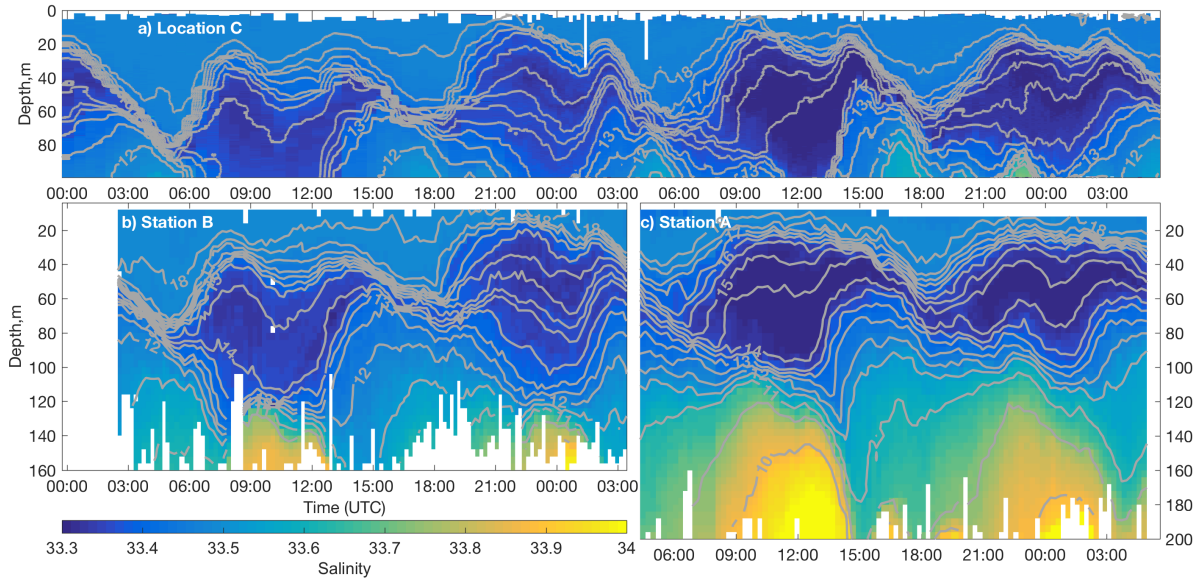

Figure 2.3: Time series of salinity contoured with isotherms spaced every 0.5 degrees between 10 and 18 °C. Panel a) represents the 54-hour time series obtained at location C. Panels b) and c) are from measurements at shipboard station B and A, respectively. The panels are oriented so that simultaneous measurements are vertically aligned.

measured by microstructure shear profilers agree well with those inferred from Thorpe scales [*Ferron et al.*, 1998; *Alford et al.*, 2006]. A very small value of background dissipation ($\varepsilon_o = 10^{-10}$ W kg^{-1}) is assumed in locations without overturns, which may bias the estimates slightly low [*Frants et al.*, 2013; *Koch-Larrouy et al.*, 2015]. 4-m shear ($S = \delta u/\delta z$) was computed at stations A and B (though not at C due to coarse vertical resolution of the ADCP there), and was used to compute the 4-m Richardson number ($Ri \equiv \frac{N^2}{S^2}$) in order to assess the role of shear instability or reduced stratification in the observed dissipation.

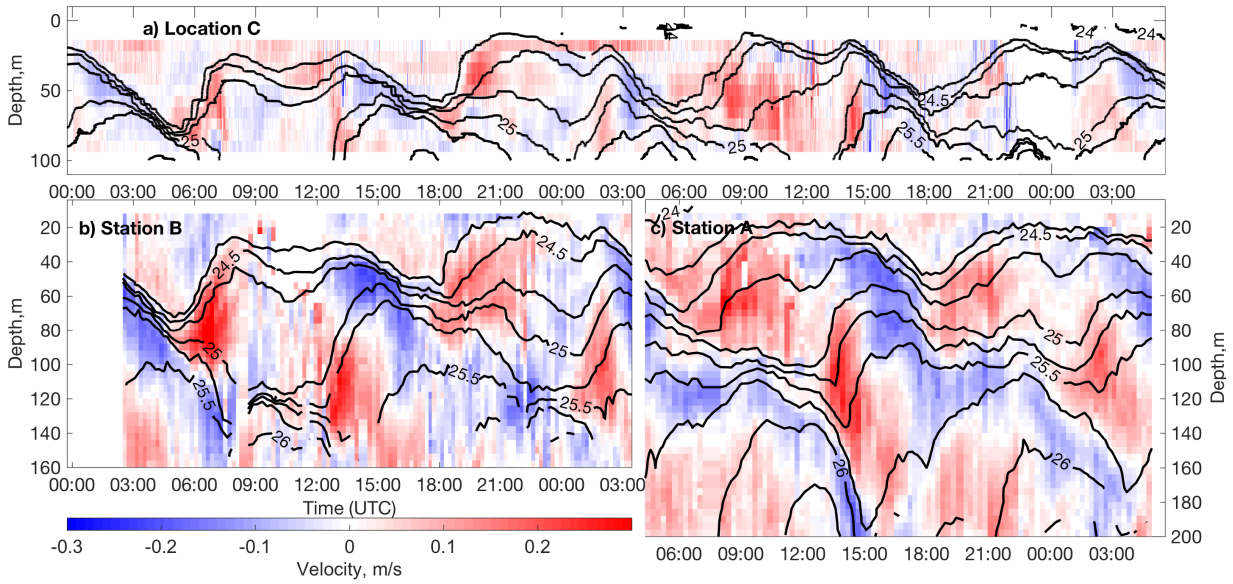

Figure 2.4: As in Figure 2.3, but showing along-canyon velocity contoured with isopycnals spaced every 0.25 units between 1024 and 1026.5 kg m^{-3}. Positive values (red) indicate flow towards the canyon head. The along-canyon coordinate is defined as 144, 140 and 124 degrees true at stations A, B and C, respectively

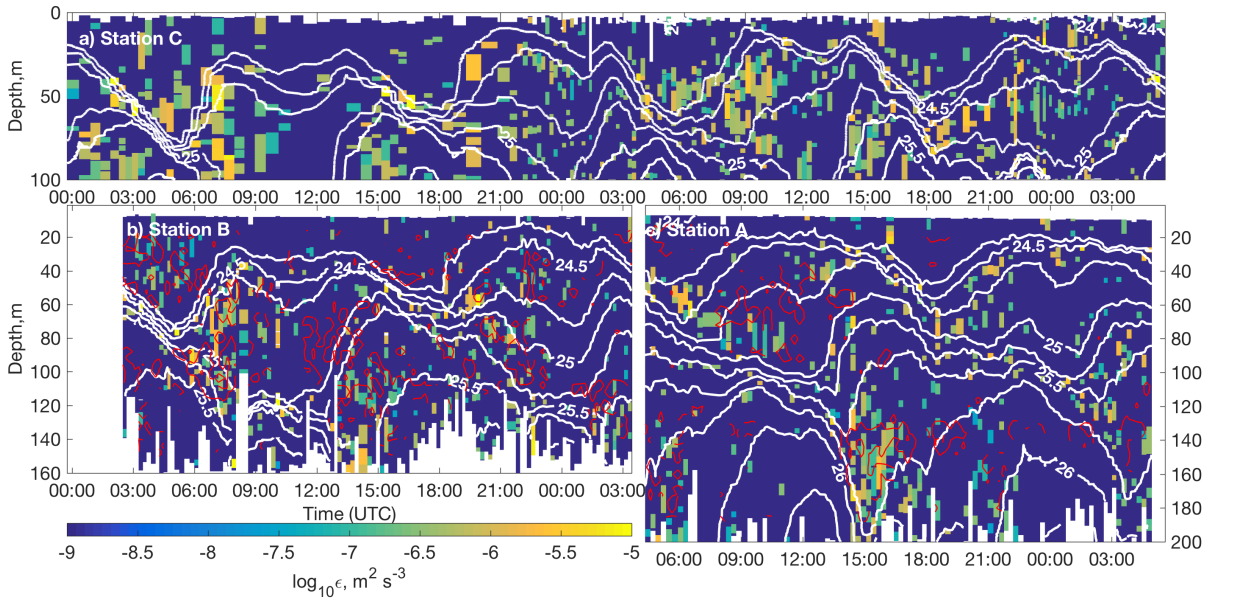

Figure 2.5: As in Figure 2.3, but showing dissipation, ε, inferred from Thorpe scale overturns. Isopycnals are contoured every 0.25 units between 1024 and 1026.5 kg m^{-3}. 4-m shear richardson number for Ri = 1 is contoured in red (panels b-c).

2.3 Results

2.3.1 Phenomenology

Over two diurnal cycles, CTD observations at stations A, B, and C revealed energetic internal wave motions (Figs. 2.3, 2.4, 2.5). Oscillations in density were large, with mid-depth vertical isopycnal displacements exceeding 50 m fluctuations in 100 m water depth at station C. Mid-depth oscillatory flow (Fig. 2.4) associated with the events advected a layer of low-salinity water from offshore to onshore and back. The same mid-depth, low salinity water extended offshore of the study area, as confirmed by the hydrographic section along the canyon axis (Fig. 2.1a).

High isopycnal strain events occurred once per semi-diurnal tidal cycle at both a deep ($\sim$140 m) and shallow ($\sim$50 m) location in the water column with a distinct pattern of high strain alternating between the two mid-depth locations (Figs. 2.4, 2.5). Enhanced dissipation ($O(10^{-7} - 10^{-5}$ m^2 s$^{-3})$) coincided with these high strain regions (Fig. 2.5), as also found by *Alford and Pinkel* [2000b] and *Levine and Boyd* [2006]. Within these regions, *Ri* fell below unity (Fig. 2.5b,c), indicating that additional shear at finer vertical scales may lead to instability and breaking.

HKE/APE ratios at all stations were significantly less than that expected for freely-propagating linear D_2 internal waves at this latitude (HKE/APE = 1.92; *Gill* [1982]; *Petruncio et al.* [1998]; *Zhao et al.* [2012]) (Table 2.1). In addition, the observed group speed for each mode was significantly less than the theoretical value. As anticipated, these results suggest partial reflection of the D_2 internal tide.

2.3.2 Harmonics

Harmonic fits to displacement and along-canyon velocity confirmed the presence of a prominent D_2 component (Table 2.2), but a fit using only the primary tidal constituents D_2 and D_1

left a large portion of variance unaccounted for. Including higher harmonics of D_2 ($2D_2$ and $3D_2$) improved reconstruction of the signal significantly, such that 84-88% of variance in isopycnal displacement and 60-70% in along-canyon velocity was described by these four constituents at A and B. Additionally, the $2D_2$ tidal constituent explained an equal or greater amount of the total variance compared to D_1 for both quantities at all stations.

The amplitude and fraction of variance explained by the D_2 signal decreases from offshore to onshore (from A to B to C; Table 2.2), and the same evolution is visually apparent in p' (Fig. 2.6a-c). The observed waveform changes from a semi-diurnal oscillation with high-frequency variability superimposed on top at Station A (Fig. 2.6a) to a waveform that is dominated by the higher harmonics of D_2 at Station C (Fig. 2.6c). This evolution of the waveform from semi-diurnal to high frequency suggests that the energy in the D_2 frequency band was either dissipated due to breaking or was siphoned into its higher harmonics through nonlinear interactions. The depth-integrated energy flux due to the D_2 harmonics of $\mathbf{u}'$ and p' also explain less variance as waves move up canyon (Fig. 2.6d-f). The other harmonics and the interaction between these constituents are necessary to capture the temporal variability of the observed depth integrated energy flux at all stations.

2.3.3 Energetics

Time-averaged, vertically integrated energy flux vectors (Fig. 3.1, inset), calculated using the methods described in Section 2.2, were oriented up-canyon at all three stations. The energy flux decreased toward the canyon head from 182 ± 18 W m^{-1} at A to 46 ± 5 W m^{-1} at C. The magnitude of these fluxes was small compared with fluxes found in Monterey [*Kunze et al.*, 2002] or Gaoping Canyons [*Lee et al.*, 2009], but greater than fluxes found in the similarly-sized, supercritical Ascension Canyon of $O(10$ W m$^{-1})$ [*Gregg et al.*, 2011].

The vertical time-averaged along-canyon energy flux profiles, $\overline{F_{ac}(z)}$, at stations A and B (Fig. 3.8) had a double peaked structure, indicating that the energy flux is not dominated by

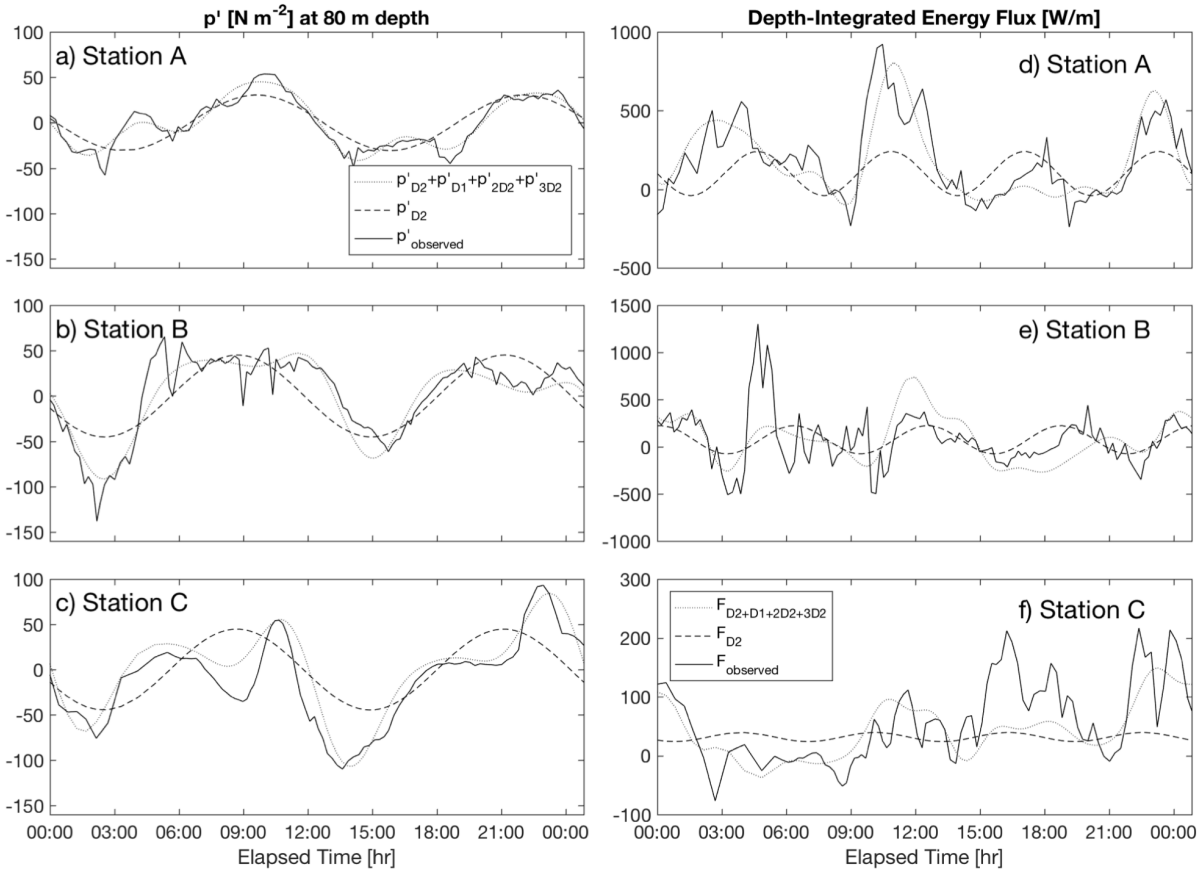

Figure 2.6: The observed baroclinic pressure pertubation (p') [N m^{-2}] at 80 m depth (solid line) over two semi-diurnal tidal periods for a) Station A, b) Station B and c) Station C. The dashed line shows the hamonic fit of p' for the D_2 tidal constituent while the dotted line shows the hamonic fit of p' for the D_2, D_1, $2D_2$, and $3D_2$ tidal constituents. The observed depth-integrated energy flux [W/m] (solid line) over two semi-diurnal tidal periods for d) Station A, e) Station B and f) Station C. The dashed line shows depth-integrated energy flux calculated from the D_2 harmonics of u' and p' while the dotted line shows the depth-integrated energy flux calculated from the D_2, D_1, $2D_2$, and $3D_2$ harmonics of u' and p'. Panels are arranged from the most offshore station on top to the most nearshore station on bottom. For each station the same time periods are shown for p' and depth-integrated energy flux.

mode-1 like in other observational studies (e.g. *Nash et al.* [2006]), but includes significant contributions from higher baroclinic modes. Peaks at 50 m and 120 m corresponded with the depths of the two strong, twice-daily isopycnal strain events apparent in Figure 2.4, and a minimum at $\sim$70 m depth corresponded with the mid-depth node in isopycnal displacement. The distinct double-peaked vertical structure of the energy flux broke down towards the canyon head at C. Time-averaged vertical profiles of dissipation (Fig. 3.8) show enhanced mid-depth dissipation, and there is a noticeable correspondence between elevated dissipation and peaks in along-canyon energy flux, particularly at Station C. The up-canyon energy flux convergence, $-d\overline{F_{total}}/dx$, was 0.27 ± 0.19 W m^{-2} between A and B and 0.15 ± 0.16 W m^{-2} between B and C. Additionally, assuming a no-flux boundary at the shoreward end of the canyon yielded a flux convergence of 0.26 ± 0.10 W m^{-2} between station A and the canyon head.

2.4 Discussion

Although the time-series presented here are short, they represent the first tidally resolved measurements within a supercritical canyon. They reveal strong yet intermittent turbulence in concert with large isopycnal strain and low Ri within the LJC. Enhanced dissipation is associated with steep, nonlinear internal tides and occurs in mid-depth maxima.

Recent work by *Waterhouse et al.* [2017] suggested a similar phenomenology towards the head of Eel canyon – a 30 km long sinuous canyon whose thalweg is largely subcritical to the D_2 internal tide. There, semidiurnal internal tides that propagated freely through the largely subcritical canyon partially reflected from the steep bathymetry at the head of the canyon and led to enhanced dissipation at mid-depths–but only at locations close to the head of the canyon. The results from *Waterhouse et al.* [2017] and the current work suggest that the vertical distribution of dissipation within supercritical canyons differs from that of their subcritical counterparts, and that reflection near supercritical slopes at canyon heads generates mid-depth dissipation

that may efficiently dissipate incident D_2 energy. Previous work in subcritical canyons such as Monterey found enhanced dissipation near the bottom primarily due to bottom-trapped bores or topographically controlled hydraulic flows [*Wain et al.*, 2013; *Carter and Gregg*, 2002]. However, in the reflective LJC we observed elevated dissipation and periods of weak stratification at mid-depths. This suggests a different mechanism where the superposition of incident and reflected waves gives rise to mid-column rather than near-bottom mixing.

The finding that HKE/APE ratios and groups speeds for all modes at all stations within the LJC are lower than those of a freely propagating D_2 internal wave suggests that the steep canyon walls reflect the incident internal tide as anticipated. However, the reflection is complex and not complete. One complexity is that a standing or partially-standing wave has a HKE/APE ratio that varies in space. Repeated observations over a spatial extent on the order of the horizontal wavelength is necessary to confirm the exact nature of the wave-wave interaction. Such reduced HKE/APE ratios however are a promising indicator of a partially standing waveform. Additionally, two waves of equal amplitude and frequency traveling in opposite directions along the same axis produce energy fluxes with zero net flux along the axis, bands of positive and negative cross-axis flux at quarter wavelength intervals, and energy flux peaks near the surface and bottom [*Nash et al.*, 2004]. A *partially* standing wave gives rise to constant along-axis flux in the direction of the dominant constituent wave and energy peaks at depths which depend upon the phasing of the constituent waves [*Martini et al.*, 2007]. Our observations show fluxes in the up-canyon direction that vary in amplitude over a wavelength (Fig 2.6), and very weak and nearly constant cross-canyon fluxes (not shown). We also see peaks in energy flux at mid-depths at all stations. Our observations align more, but not completely, with the description of a *partially* standing wave. Given the complexity of the canyon bathymetry and the possibility of reflection from angled sidewalls complicating the energy flux patterns, 1-D models of reflection are not sufficient for understanding the waveform within the canyon system. Observations with higher spatial coverage and an accompanying modeling effort would be required to fully describe the reflective

characteristics of IWs in LJC.

The significant convergence of up-canyon energy flux indicates that there is an energy sink within the canyon. Measured dissipation rates, however, were a factor of 5 lower than that required to close the energy budget. Some modeling studies show there can be significant variation in the across-canyon direction, with the largest along-canyon energy fluxes near the canyon axis [*Hall and Carter*, 2011]. The assumption that along-canyon energy flux is uniform in the cross-canyon direction used here, then, may lead to an overestimation of flux and convergence. Prior studies have also suggested that dissipation rates are stronger near the sidewalls of canyons, and it is equally likely that measurements at a single location missed a majority of the mixing processes occurring in the LJC [*Wain et al.*, 2013]. In order to determine the contribution of incident energy flux, local conversion, and dissipative processes to the total energy budget, further observations are required.

Our results demonstrate that narrow, steep canyons like LJC, despite their size and reflective character, host processes that greatly enhance energy dissipation at mid-depths. Regionally, this dissipation is critical for mixing of tracers including heat, carbon and nutrients. In particular, mid-depth mixing near the nutricline may significantly alter the local nutrient distribution, with important but understudied impacts on local ecology. Additionally, enhanced mixing within the many small canyons impinging the coastline worldwide may be important on the scale of global energy budgets. Because canyons such as the LJC are much smaller in scale than the current resolution of climate models, a parameterization is neccessary to incorporate the associated mixing in global simulations of climate, circulation, and biological productivity. To do so will require an understanding of the dynamics at play within various canyon archetypes, as well as a catalogue of where those types of canyons exist. To date, neither of these goals have been addressed sufficiently.

The temporal span and spatial scope of the results of this experiment were limited, and further work is needed to investigate the mechanisms characteristic of canyon systems. The

finding that D_2 internal waves accounted for less variance moving up-canyon suggested that nonlinear interactions generate higher harmonics amid the supercritical topography. The slope of the canyon approaches critical for the steeper characteristic slopes of these higher harmonics of the D_2 internal tide, whose interaction with critical topography may then lead to enhanced wave breaking and near-bottom mixing. In the future, modeling work and longer time series that better characterize variability are needed to determine the mechanisms leading to enhanced dissipation in small, narrow canyons.

♢ ♢ ♢

2.5 Acknowledgements

This chapter, in full, is a reprint of the material as it appears in Journal of Geophysical Research: Oceans, 2017. Alberty, Marion S.; Billheimer, Samuel; Hamann, Madeleine M.; Ou, Celia Y.; Tamsitt, Veronica; Lucas, Andrew J.; Alford, Matthew H., 2018. The dissertation/thesis author was the primary investigator and author of this paper.

The ship time required for the work described in this manuscript was provided by the University of California Ship Funds Program, and the authors gratefully acknowledge the opportunity provided by the program as well as support from the captain and resident technicians of the R/V Sproul. We thank Jonathan Nash and his group at Oregon State University for the use of χ-pods and the time spent preparing them for this experiment. The authors thank Eric Kunze and three anonymous reviewers who provided comments and suggestions that greatly improved this work. This manuscript resulted from a course in proposal writing and observational oceanography at Scripps Institution of Oceanography. The students thank the course instructors, M.H. Alford and A.J. Lucas, for many hours of support and advice. All student authors contributed equally to this manuscript. Shipboard CTD and ADCP data used for this analysis can be found at https://doi.org/10.7284/124414 and https://doi.org/10.7284/116646.

Chapter 3

Reflected internal tides in a shelf-incising submarine canyon: dynamics, turbulence, and context

3.1 Introduction

Submarine canyons are common along continental margins worldwide [*Allen and Durrieu de Madron*, 2009; *Harris and Whiteway*, 2011]. They exhibit an array of geometries and configurations – some are straight and narrow, others are wider and meandering; some extend to and incise the continental slope region (slope canyons), others are confined to the shelf (shelf canyons). Wherever they occur, they act as conduits that connect the shallower shelf to deeper waters offshore. Because a canyon's characteristic length scale is around an order of magnitude smaller than that of the adjacent shelf, canyons tend to cause ageostrophic flows that enhance cross-shelf exchange and strengthen wind-driven up- and down-welling flows [*Klinck*, 1989; *Hickey*, 1997; *Allen and Hickey*, 2010]. Breaking of focused internal waves, hydraulic control over ridges and bends, and enhanced ageostrophic flows all lead to small-scale turbulent processes

such that canyons are known to be hotspots of enhanced turbulent dissipation and diapycnal diffusivity [*Carter and Gregg*, 2002; *Lee et al.*, 2009; *Gregg et al.*, 2011; *Alford and MacCready*, 2014; *Waterhouse et al.*, 2017; *Alberty et al.*, 2017].

The classical theory of turbulence driven by internal waves in canyons is presented by *Hotchkiss and Wunsch* [1982]. Considering typical canyon geometry, they theorize that internal waves incident at a canyon's offshore extent (mouth) reflect downward off of steep sidewalls and towards its nearshore terminus (head) over an axis (thalweg) that slopes gently in the along-canyon direction. Wave focusing leads to energy convergence and high velocities near the canyon floor and head that generates turbulence in these locations. Waves that encounter an axis slope close to their own angle of propagation are also expected to scatter and break near the bottom. In the handful of canyons in which turbulence has been observed to date, the expected patterns of enhanced turbulence near the bottom and head of a canyon do occur [*Petruncio et al.*, 1998; *Kunze et al.*, 2002; *Carter and Gregg*, 2002; *Lee et al.*, 2009; *Kunze et al.*, 2012; *Wain et al.*, 2013; *Hall et al.*, 2014], but so do patterns of turbulent enhancement at mid-depths and in other regions of the canyon [*Gregg et al.*, 2011; *Zhao et al.*, 2012; *Hall et al.*, 2014; *Waterhouse et al.*, 2017; *Aslam et al.*, 2017; *Alberty et al.*, 2017].

Several studies of internal waves in canyons have reported patterns of energy partitioning consistent with partially standing waveforms in canyon systems [*Petruncio et al.*, 1998; *Zhao et al.*, 2012; *Hall et al.*, 2014; *Waterhouse et al.*, 2017; *Alberty et al.*, 2017]. Many canyons steepen approaching their nearshore terminus or have sharp bends that can reflect incident waveforms. Stratification changes can also alter the criticality of slopes that are less steep and lead to reflection during periods of increased stratification near the bottom [*Zhao et al.*, 2012]. As suggested by observations made by *Alberty et al.* [2017] and ray tracing models by *Nazarian and Legg* [2017], the superposition of incident and reflected waves may set the stage for elevated shear, strain, and breaking events at mid-depths.

Observations and studies of internal wave reflection from steep topography in canyons

are limited, but studies of reflection from steep continental slopes show that a low-mode incident wave is accompanied by back-reflection and scattering to higher modes. *Thorpe* [2001a] presents an analytical treatment of reflection from a rough slope, and finds that the shear in scattered waves scales with steepness and roughness of the slope. In his follow-up work, *Thorpe* [2001b] finds that the scale of a reflected wave groups sets the vertical scale of dissipative regions over the slope. Observations by *Nash et al.* [2004] over a corrugated continental slope in the mid-Atlantic Bight show that the convergence of low-mode semi-diurnal onshore energy flux is balanced by high-mode offshore flux; they postulate that enhanced near-bottom mixing offshore of the steep topography and enhanced diffusivity extending over the bottom ˜1000m are a direct consequence of the reflection process.

With steep sidewalls and thalwegs that generally steepen approaching the canyon head, submarine canyons are prime locations in which reflection and scattering of low-mode incident waves may give rise to dissipative dynamics. If the mechanism by which incident waves dissipate their energy in a reflective canyon is via instability during mid-depth strain events rather than critical near-bottom breaking, the time-averaged profile of ε would be enhanced throughout the water column rather than increasing towards the bottom. Understanding this time-averaged distribution of dissipation is a fundamental piece in our understanding of the role of submarine canyons in mixing on both global and regional scales.

The observations presented here were collected in the La Jolla Canyon System (LJCS), a shelf-incising canyon located just offshore of Scripps Institution of Oceanography in La Jolla, California USA. Unlike previously studied systems like Monterey Canyon (MC) and Eel Canyon (EC) that extend over the shelf and incise the continental slope, the LJCS is largely confined to the shelf region. Where previously studied "slope canyons" often contain, connect to, and foster mixing along deep isopycnals relevant for the overturning circulation of the deep ocean [*Kunze et al.*, 2012], "shelf canyons" like the LJCS are impactful for regional dynamics and interactions with the inner shelf and nearshore regions. Turnover rates, circulation patterns, and sediment

transport in nearshore waters are affected by nearby canyon topography and the surface wave refraction associated with it [*Shepard and Inman*, 1950; *Hickey et al.*, 1986]; connection to deep, nutrient rich waters influences biological productivity within canyons and in canyon-adjacent shallows [*Vetter*, 1994; *Vetter and Dayton*, 1999; *Allen et al.*, 2001; *Vetter et al.*, 2010; *Alford and MacCready*, 2014; *Kavanaugh et al.*, 2015]; sediments along the shelf adjacent to canyon systems have a tendency to flow towards canyon incisions and offshore [*Liu et al.*, 2002; *Puig et al.*, 2003]. The dynamics of shelf-incising canyons interact with every facet of the nearby biogeochemical environment.

Understanding the dynamics at play within shelf-incising canyon systems both informs our ability to parse out these complicated multidisciplinary puzzles and expands our understanding of canyon physics in general. Comprehensive measurements can be made in these shallower and more easily accessible systems to examine the effects of variable stratification and forcing, and the physical intuition can be applied and generalized to submarine canyons throughout the ocean.

3.2 Experiment Layout

The La Jolla Canyon System (LJCS) is a shelf-incising canyon that terminates in the La Jolla Cove just offshore in La Jolla, CA. The greater LJCS is 24km long, 3km wide, and 1000m deep at its furthest offshore extent. Between 8km and 14km from its head the canyon meanders to the south. Two kilometers from its head, the LJCS bifurcates into two branches: the La Jolla Canyon (LJC) extends to the south parallel to the direction of the main canyon axis while the Scripps Canyon (SC) branches off to the north in a direction nearly perpendicular to LJC. Located 1.6 km away, the headland of Point La Jolla sits south of the canyon head blocking strong alongshore flows in the vicinity.

The La Jolla Internal Tide Experiment II (LaJIT2) was carried out in the LJCS in September, 2016 (Fig. 3.1). The experiment consisted of 7 days of shipboard surveys and 3 months of

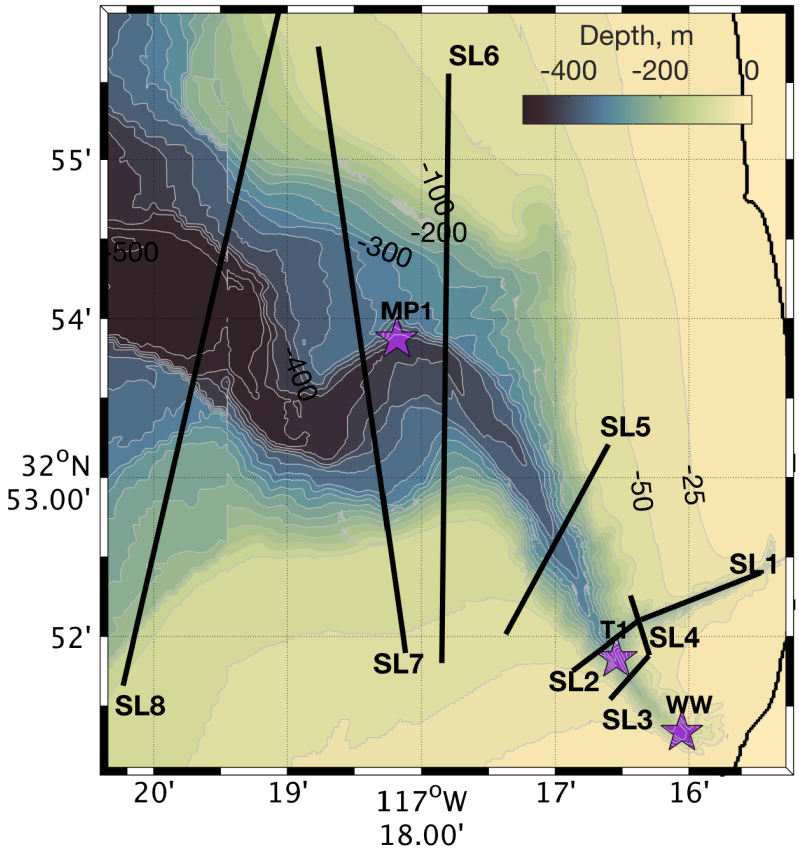

Figure 3.1: Study region. Bathymetry contoured in 50-m intervals (grey lines) with a thick black contour to indicate the coastline. Straight black lines represent the tracks occupied during the SWIMS surveys. Purple stars indicate moorings deployed along the canyon axis.

moored data collected from three locations. On September 10, the moorings were deployed at locations along the axis of the canyon. The deepest mooring (MP1) was located at 415m depth just onshore of the meander and consisted of a downward-looking 75kHz Workhorse Acoustic Doppler Current Profiler (ADCP) and a McLane moored profiler that carried a SeaBird (SBE) 37 CTD and acoustic current meter (ACM) and made full-depth profiles every 15 minutes. Just onshore of the bifurcation point, mooring T1 reached 240m depths and consisted of 36 SBE56 thermistors and two SBE37 CTDs spaced 3-8m apart (denser spacing near the thermocline) and a downward-looking 75kHz Workhorse ADCP. At the head of the canyon in 105m depth, station

WW consisted of a Wirewalker wave-powered profiler [*Rainville and Pinkel*, 2001; *Pinkel et al.*, 2011] that carried a sideways-looking Aquadopp ACM, as well as temperature, conductivity, pressure, oxygen, chlorophyll fluorescence, and backscatter sensors . Stations MP1 and T1 were recovered on December 14, 2016 while WW remained in place transmitting data from its surface float in real time through September of 2017. The McLane on MP1 stopped profiling after 5 weeks, and the ACM on WW experienced intermittent failures due to power supply issues.

From September 10-17, the R/V *Gordon Sproul* repeatedly occupied eight cross-canyon lines (SL1-8) for 25-36 hours apiece to resolve semi-diurnal signals and towed the Shallow Water Integrated Mapping System (SWIMS). These are detailed in Table 3.2. SWIMS is a 300 kg towed body that is winched up and down at 1-2ms^{-1} while resolving measurements with 0.5m spacing in the vertical and 10-610 m horizontally depending on water depth (details in Table 3.2). SWIMS carries up- and down-ward looking 300 kHz ADCPs capable of resolving velocities near the bottom near steep canyon bathymetry as well as temperature, conductivity, pressure, oxygen, chlorophyll fluorescence, and turbidity sensors [*Alford et al.*, 2006; *Wain et al.*, 2013]. The *Sproul* also continuously operated a 300kHz narrow band hull-mounted ADCP and measured currents in the upper ≈150m of the water column.

Table 3.1: SWIMS lines SL1-SL8 details. From left to right, the line number, start time, duration, length, maximum depth, number of occupations, maximum spacing between profiles, and energy and flux adjustment factor is shown for each line.

Line	Start Time	Duration (hr)	Length (km)	H_{max} (m)	N	Δx_{max} (m)	Δt_{avg} (hr)	$F_{adj.}$
SL1	9-13-16 23:00	25.25	1.5 km	200	16	120	1.55	1.18
SL2	9-13-16 23:00	25.25	1.0 km	300	17	175	1.55	1.18
SL3	9-13-16 23:00	25.25	0.7 km	225	16	100	1.55	1.18
SL4	9-13-16 23:00	25.25	0.7 km	225	16	105	1.55	1.18
SL5	9-12-16 08:23	38.37	2.5 km	300	38	270	1.01	1.26
SL6	9-16-16 04:10	25.33	6.8 km	400	21	375	1.21	0.87
SL7	9-11-16 06:30	25.52	7.1 km	425	14	415	1.82	1.26
SL8	9-15-16 02:00	25.92	8.1 km	525	15	610	1.73	1.00

In addition to the moorings deployed specifically for LaJIT2, data from nearby long-

term monitoring stations were used to provide regional context for the canyon measurements. The Del Mar mooring (DM), located 2 km north of the canyon on the 100m isobath, provides measurements at 10-minute intervals from 9 CTDs, 3 dissolved oxygen sensors, 2 Chlorophyll fluorescence sensors, and an upward-looking 300 kHz ADCP. These data were available until November 16 when it was recovered for servicing. We also use hourly sea surface height data from the *National Oceanic and Atmospheric Administration* [2016-2017] and wind data from the *Coastal Data Information Program* [2016-2017] collected from the pier at Scripps Institution of Oceanography.

3.3 Analysis Methods

3.3.1 Isolating the Semi-diurnal Internal Tide

Shipboard surveys across the canyon (SL1-8 Fig. 3.1; see Fig. 3.2 for example data) were used to diagnose the spatial characteristics and energetics of the semi-diurnal internal tide. Each line was divided into a set of locations (stations) corresponding to the variable spacing (between 100m and 600m) expected for a single SWIMS profile to be made at that water depth given an average tow speed of 3 kts and fall rate of 1.5 ms^{-1}. For each station, all profiles falling within half the distance between the adjacent stations were concatenated, and semi-diurnal motions were isolated from the reconstructed time series using harmonic analysis. For each profile, isopycnal displacement (η) was calculated relative to the average isopycnal depth at that station. Semi-diurnal components of east- and north-ward velocity (u,v) and η were then determined by fitting the data $A(x,z,t)$ to the model

$$A(x,z,t) = A_O(x,z)\sin[\omega_{M_2}t + \phi(x,z)] \tag{3.1}$$

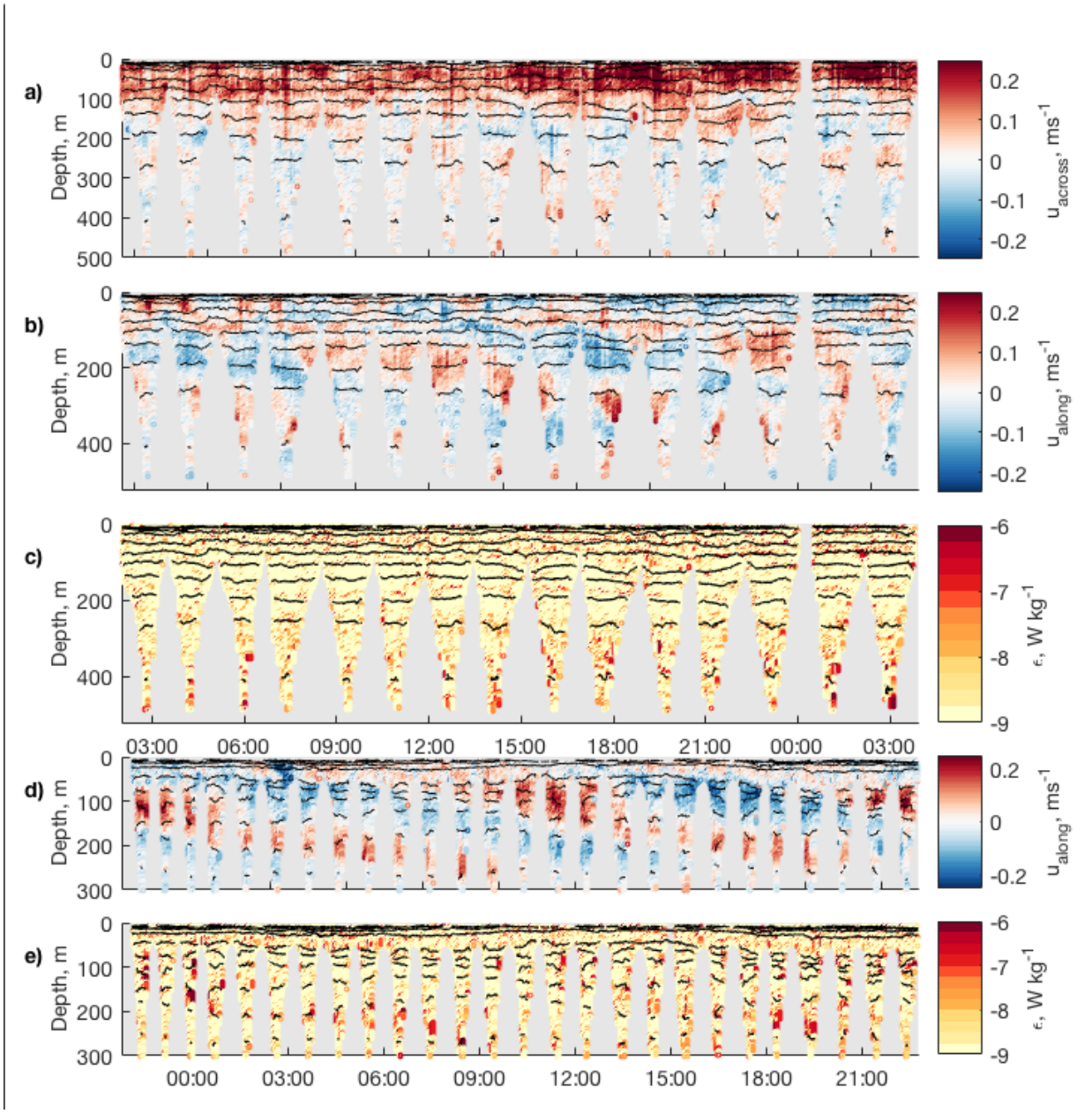

Figure 3.2: Observations from SWIMS during the occupation of line SL8 (a-c) and SL5 (d-e). (a) Across-canyon velocity, (b,d) along-canyon velocity, and (c,e) dissipation; isopycnals (black) are contoured every 0.25 kg/m^3.

where x is the along-track distance, ω_{M_2} is the M_2 tidal frequency, A_O is amplitude, ϕ is phase relative to a common reference time, and A represents either u, v or η.

Semi-diurnal signals from data at each of the moorings were isolated by standard band-

passing methods. A fourth-order Butterworth filter with zero-phase response, a center frequency $\omega = 12.4$ hr^{-1} and quarter-power points at 10 hr^{-1} and 14.8 hr^{-1} was designed to minimize filter ringing. Profile data from the McLane profiler were first linearly interpolated onto a grid with a constant timestep of 10 min before filtering. Hereafter, u_{M_2}, v_{M_2}, and η_{M_2} refer to time series reconstructed either from the harmonic fits (for SL1-8) or from bandpassed data (MP1, T1, DM).

3.3.2 Energetics

Available potential energy (APE) and horizontal kinetic energy (HKE) were computed for each station and mooring as

$$APE(z,t) = \frac{1}{2}\rho N^2(z)\eta^2(z) \tag{3.2}$$

and horizontal kinetic energy (HKE)

$$HKE(z,t) = \frac{1}{2}\rho|\mathbf{u}^2(z)| \tag{3.3}$$

where ρ is density, H is water depth, $\mathbf{u}$ is the horizontal components of velocity, and the overline indicates vertical averaging. Total energy (E) is taken as the sum of HKE and APE at any given location and time.

Baroclinic pressure perturbation is calculated as

$$p'(z) = \overline{\rho}\int_{-z}^{0}\eta(z')N^2(z')dz' - \overline{p} \tag{3.4}$$

, where the overline indicates the mean $\overline{p} = \overline{\rho}\int_{-H}^{0}\eta(z')N^2(z')dz'$.

Semi-diurnal velocity perturbation, $\mathbf{u_{M_2}}'(z,t)$, and energy flux $\mathbf{F}(z,t) = \mathbf{u}'p'$ were computed by standard methods following *Kunze et al.* [2002] and *Nash et al.* [2005]. Uncertainty

due to sparse temporal sampling and/or incomplete coverage of the water column was computed following *Nash et al.* [2005].

Wave-averaged quantities $\langle APE \rangle$, $\langle HKE \rangle$, and $\langle \mathbf{F} \rangle$ were also computed for each location and mooring. For SWIMS stations, a single vertical profile of each quantity was computed from the available data spanning 2 full tidal cycles. For moorings, $\langle APE \rangle$(z,t), $\langle HKE \rangle(z,t)$, and $\langle \mathbf{F} \rangle(z,t)$ were computed from the running mean spanning a single tidal cycle at each depth.

3.3.3 Modal Decomposition and Reflection

The vertical structure of internal tides can be described as vertical modes that depend only on $N(z)$. These modes are the solutions to the equation

$$\frac{\partial^2}{\partial z^2}\eta(z) + \frac{N^2(z)}{c_n^2}\eta(z) = 0 \tag{3.5}$$

with boundary conditions $\eta(0) = \eta(H) = 0$, and where n is mode number, c_n is eigenspeed, and H is water depth. The eigenspeed c_n is the geometric mean of the phase speed (c_n) and group speed (c_g), $c_n^2 = c_g c_p$ [*Alford and Zhao*, 2007b]. This method is applied to obtain the first five vertical modes for u_{M_2}, v_{M_2}, and η_{M_2}, after which HKE, APE, and $\mathbf{F}$ are computed for each mode [*Gill*, 1982].

It should be noted that this formulation of modal structure assumes that vertical motion cannot occur at the surface or bottom and is valid rigorously only over a flat bottom [*Wunsch*, 1968; *Haney*, 1991; *LaCasce*, 2017]. Over bathymetric features (like a canyon), the bottom boundary condition should allow for vertical and horizontal velocities that are coupled over the slanted bottom. The resulting velocity modes, then, are surface intensified with weaker horizontal (cross-isobath) flows near the bottom [*Rhines*, 1970; *Charney and Flierl*, 1981]. In the limit of very steep topography (where horizontal flows are assumed to be zero at the bottom), the gravest mode is not a depth-invariant horizontal flow, but a bottom-intensified topographic wave.

With these issues in mind, we proceed cautiously with the above decomposition (Eqn. 4.4) as a diagnostic tool.

For a progressive wave, the expected ratio of HKE to APE (for each individual mode as well in total) is

$$\frac{HKE}{APE} = \frac{\omega^2 + f^2}{\omega^2 - f^2} = 1.92 \tag{3.6}$$

at this latitude [*Gill*, 1982]. If the wave is reflected (or partially reflected), the vertical component of the motion of the interface becomes larger so that this ratio decreases below the expected value. We assessed HKE/APE for all computed modes in order to diagnose reflection, by mode. *Martini et al.* [2007] use a similar by mode diagnostic of reflection, but use the ratio $c_g E/F$ as an indicator of progressive wave behavior for each mode (as suggested by *Alford and Zhao* [2007b]). For a progressive wave, the ratio of the observed energy flux (F) to the theoretical group speed times observed energy ($c_g E$) should equal 1; for a partially standing wave that ratio is less than 1 [*Alford et al.*, 2006; *Alford and Zhao*, 2007a]. Here, the two diagnostics produce qualitatively similar results.

3.3.4 Quantifying and Qualifying Turbulence

The dissipation rate (ε) of turbulent kinetic energy (TKE) was estimated using overturns in density profiles measured by SWIMS and at the McLane profiler following the Thorpe scale method [*Thorpe*, 1977; *Dillon*, 1982]. Although no microstructure sensors were used during LaJIT2, measurements of microstructure shear were made in the LJCS during a subsequent field campaign in February 2017. These measurements were used to assess the validity of the Thorpe scale method in this region. This validation is presented in Appendix A.

Quantities useful in diagnosing the processes that give rise to elevated dissipation were computed at all stations using unfiltered data. 4-m vertical squared shear was computed from velocity profiles as $S^2 = \frac{\delta u^2}{\delta z} + \frac{\delta v^2}{\delta z}$. Richardson number was computed from 4-m shear and

stratification as $Ri = \frac{N^2}{S^2}$ [*Miles and Howard*, 1964]. Eulerian strain was computed as $\frac{N^2(z,t)}{\langle N^2 \rangle} - 1$ where angle brackets indicate averaging over a tidal cycle [*Pinkel et al.*, 1991].

3.3.5 Canyon energy budget

Data collected along lines SL2-8 are used to compute a canyon-wide energy budget. Following *Gregg et al.* [2011], the energy budget for tidally-averaged quantities is given by the equation

$$\frac{dE_A}{dt} = -\frac{dF_A}{dx} + C_A + D, \tag{3.7}$$

where x is along-canyon distance, C is a production term, D is a dissipation term which includes both dissipation by turbulence kinetic energy and energy transfers to different frequencies, and the subscript A indicates that each quantity is integrated over the cross-width area of the canyon at each line. For energy flux, only the component parallel to the axis of the canyon is considered. The terms on the right-hand side of equation 3.7 can be computed directly from the measurements made by SWIMS. The production term C_A was computed at each location following the methods of *Kelly et al.* [2012] as

$$C = -\left(\frac{dh}{dx}U_{BT} + \frac{dh}{dy}V_{BT}\right)p'_b, \tag{3.8}$$

where dh/dx and dh/dy are east-west and north-south bottom slopes and U_{BT} and V_{BT} are barotropic velocities in the east and north directions computed as the depth average of the measured SWIMS velocity at each station, and p'_b is pressure perturbation (as defined in equation 3.4) at the bottom, $z = H$.

The left-hand side of equation 3.7 accounts for unsteady variability in the energy of the system which, in this experiment, is affected by the transition from neap to spring tide that occurs during the period of shipboard observations. In order to account for this variability, time series of E and F in the semi-diurnal band observed at MP1 are leveraged following *Alford et al.* [2011]

and *Wain et al.* [2013]. For each time step, a scale factor (S) for energy and flux is computed as

$$S(t) = \frac{E_{max} - E_{lp}(t)}{E_{max}}, \tag{3.9}$$

where E_{max} is the maximum value observed during the survey period and E_{lp} is the 3-day low-passed time series of E. The same is done for F, and the relevant scale factor is applied to measurements of E and F along SL1-8 for the corresponding time. These adjusted values (Tab. 3.2) are used to examine the patterns and budget in what follows.

3.4 Results

3.4.1 Low frequency currents and tidal flow structure

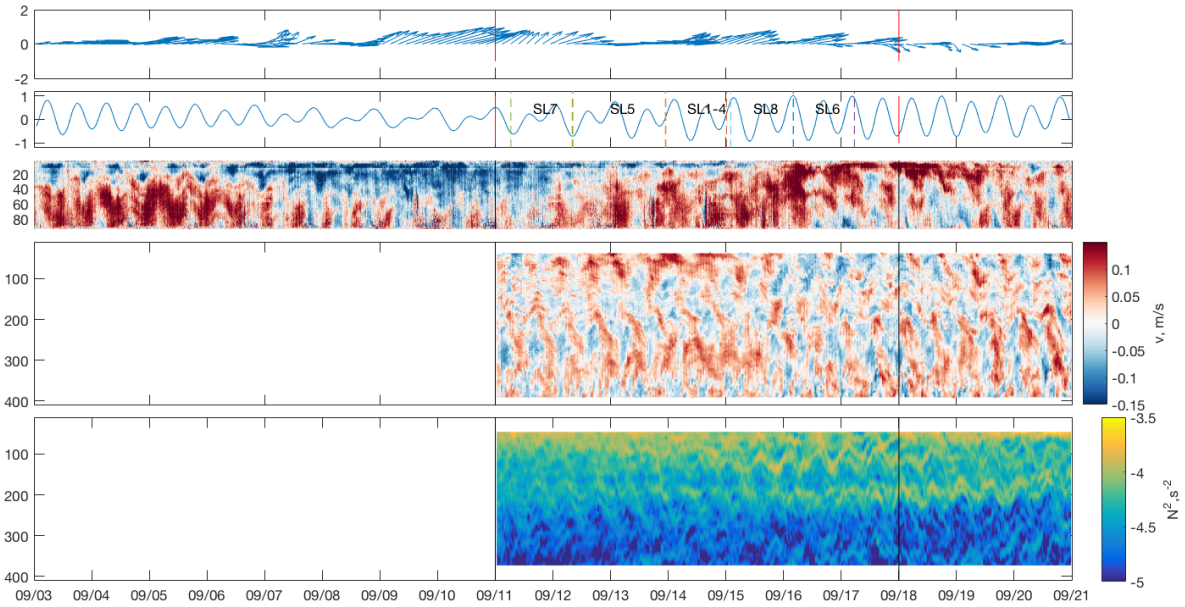

Figure 3.3: Context. (a) Two-day low-passed wind speed and direction measured at Del Mar, (b) tidal height at Scripps pier, (c) northward velocity at Del Mar, (d) northward velocity at MP1, (e) stratification at MP1. Vertical black and red lines indicate the period of shipboard observations.

Leading up to the LaJIT2 field campaign, sustained southwesterly winds blew over the

study region, and a surface-intensified southward current was observed at the Del Mar mooring (DM; Fig. 3.3). In the middle of the experiment (after Sep. 15) winds began to relax and reverse weakly. The direction of the barotropic velocity observed at DM also transitioned from south- to north-ward mid-cruise, but preceded the shifting winds by 3 days. Correlations between wind forcing and current direction was minimal, consistent with prior observations over the Southern California Shelf [*Lentz and Winant*, 1986]. Measurements of surface tides from the pier 1.5 km north of LJC indicate that the 7-day shipboard experiment spanned a transition from neap to spring tide.

At DM, the observed velocity signals are typically dominated by either a barotropic or mode-1 structure. The amplitude of semi-diurnal current oscillations is comparable to that of the sub-tidal along-shore currents. This is qualitatively quite different from those observed at MP1 (located within the canyon walls) where barotropic currents are relatively weak, the amplitude of tidal currents exceeds the sub-tidal flow, and the currents exhibit multiple zero-crossings throughout the water column (Fig. 3.3).

Depth-averaged velocities over the LJCS are weak everywhere except at the offshore extent (SL8) where a strong northward surface current is observed (Fig. 3.2a). Barotropic tides are also weak over the canyon axis but strengthen moving away from the canyon axis towards the canyon rim–particularly on the southern flank (not shown). Internal tides visibly dominate the velocity signal at depths below the canyon rim where downward phase propagation of oscillations of semidiurnal (12.42 hour) period is clear (Fig. 3.2b,d). At all stations, the baroclinic velocity structure is higher mode in character, with 2 or more zero crossings (Fig. 3.2b,d).

3.4.2 Energy flux

Depth-integrated energy fluxes (Fig. 3.4a) in the LJCS are, in general, relatively weak (O(100W m^{-2})) compared to MC and other canyons [*Petruncio et al.*, 1998; *Kunze et al.*, 2002; *Lee et al.*, 2009; *Gregg et al.*, 2011; *Wain et al.*, 2013; *Waterhouse et al.*, 2017]. Depth-integrated

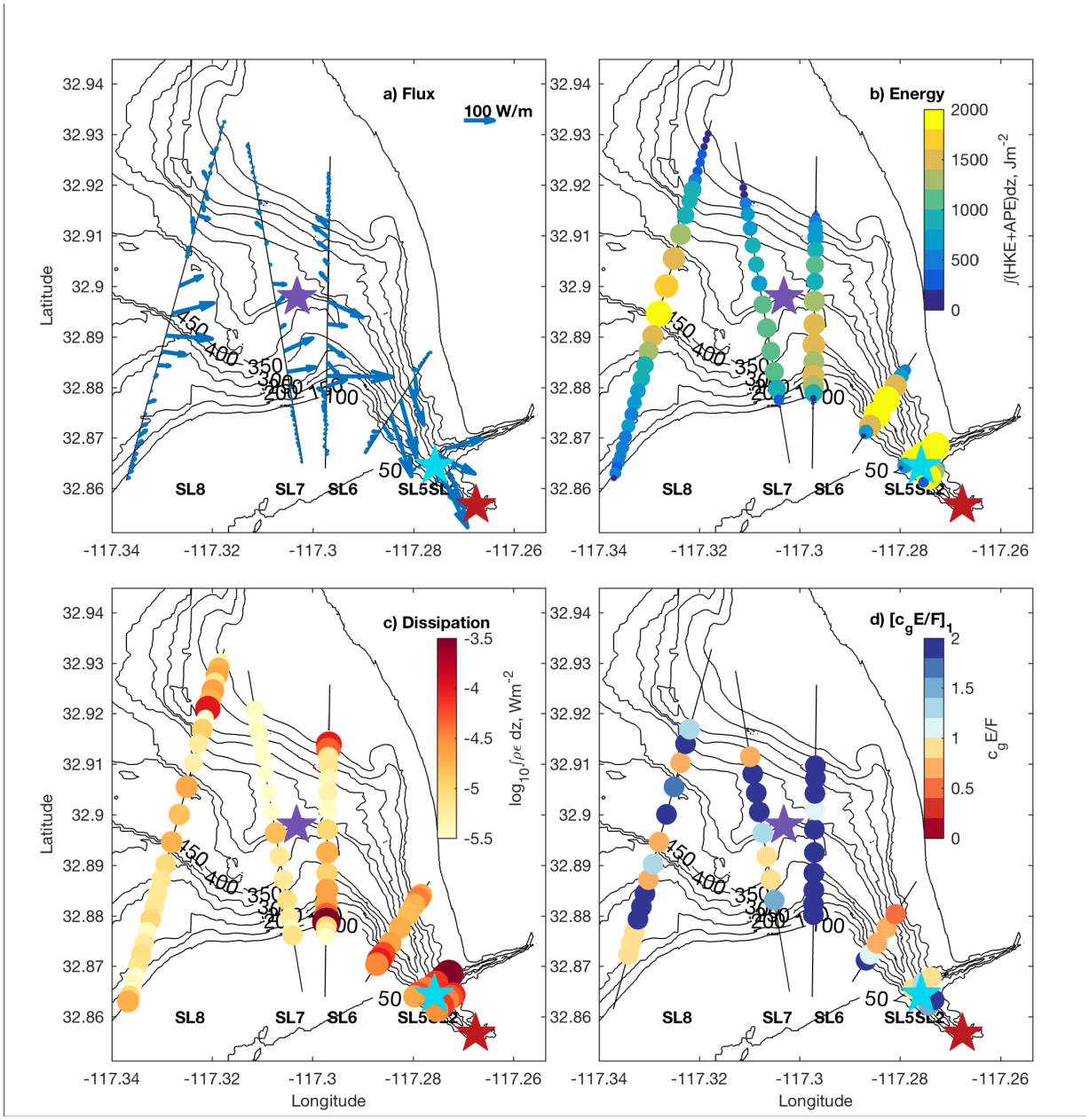

Figure 3.4: Spatial patterns of tidally-averaged (a) semi-diurnal energy flux F, (b) integrated energy E, (c) integrated dissipation ε, and (d) mode 1 $c_g E/F$ ratio computed for data collected along SWIMS lines SL2-3 and SL5-8.

energy flux is mostly oriented towards the canyon head (up-canyon) with a maximum near the canyon axis. Very small energy flux towards the canyon mouth (down-canyon) is observed over the sidewalls on the north side of the canyon (Fig. 3.4a). Energy flux is elevated in one

or more mid-depth swaths on all lines (Fig. 3.5); up-canyon flux on lines SL2, SL3, and SL5 is concentrated in a single swath just below the canyon rim. This vertical structure is not as anticipated for mode-1 waves where the expectation is little energy flux in the middle of the water column and maxima at the top and bottom (Fig. 3.5). Nevertheless, computing energy flux by mode reveals that mode 1 contains the majority of the flux, with an exception near the bifurcation point where the energy flux in mode 2 exceeds that in mode 1 (not shown).

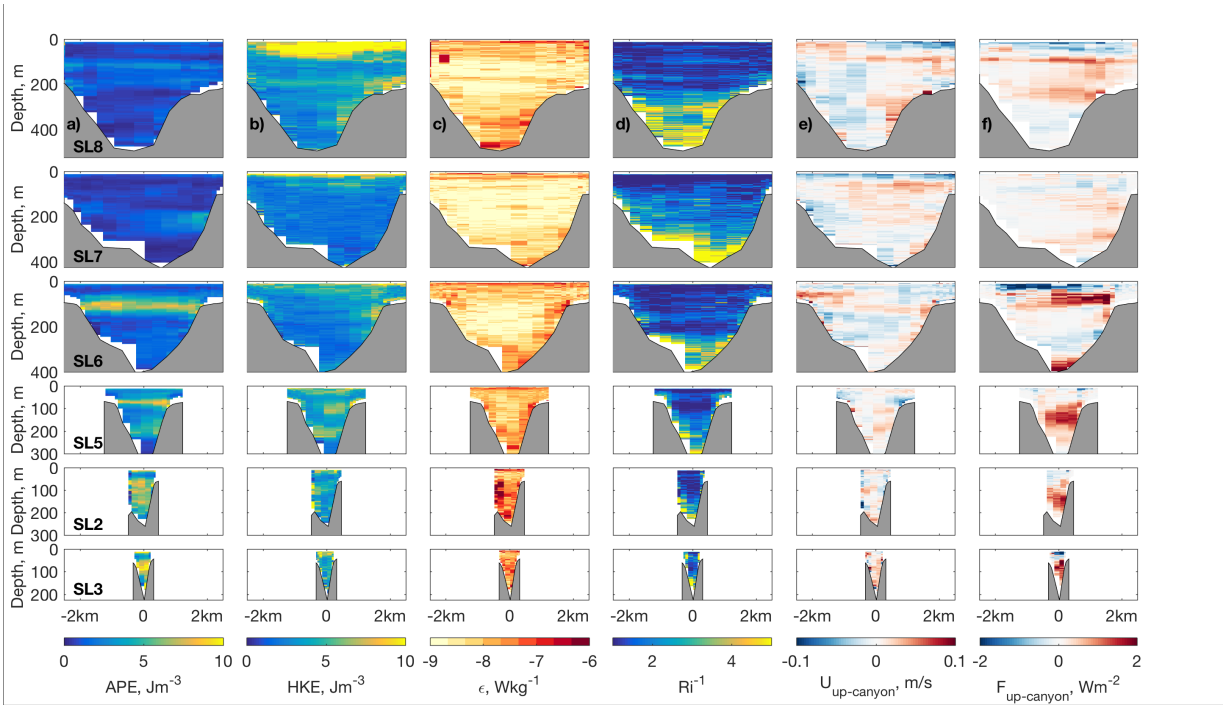

Figure 3.5: Section Average Properties. Tidally-averaged (a) potential and (b) kinetic energy, (c) dissipation, (d) inverse Richardson number, (e) up-canyon velocity, and (f) up-canyon energy flux. Top to Bottom: SWIMS lines from west to east along the main branch of the LJCS. Orientation of the panels is such that the southern end of each line is towards the right.

3.4.3 Diagnosing reflection: energy and energy partitioning

In order to diagnose patterns in the reflectivity of the internal tide in LJCS we first consider quantities computed from the total measurement at each location. *APE* is elevated along the canyon axis while *HKE* is higher over the sidewalls (not shown). Total energy E increases moving

towards the canyon head (Fig. 3.4b) due to a corresponding increase in APE. The increase in energy moving towards the canyon head is expected as flux, not energy, is conserved in a systems without energy sources or sinks.

The relative increase in APE moving towards the canyon head lowers the ratio of HKE/APE such that offshore of the meander (on lines SL7-8) the ratio falls above that expected for a freely propagating M_2 wave at this latitude ($>$1.92, indicating a progressive wave), while onshore (lines SL2-3;SL5-6) the ratio is lower ($<$1.92, indicating reflection).

Changes in the ratio of APE to HKE point are a useful initial diagnostic tool, but in order to assess internal tide reflection mode by mode, we also examine the ratio of $c_g E/F$ where values greater than 1 indicate reflection. For mode 1 (Fig. 3.4d), this metric shows a mix of progressive and reflective waves throughout the canyon system; line SL6 exhibits reflection everywhere, while SL5 shows primarily progressive waves (except on the southern canyon wall). Moving up-canyon from SL5, $c_g E/F$ increases and approaches unity. If conversion from barotropic to baroclinic motions within the canyon is negligible (as these observations suggest and is shown below), this pattern suggests that an incident mode 1 internal tide is partially reflected at the meander between SL6 and SL5, and the portion not reflected continues up-canyon where it undergoes a second reflection off of the canyon head.

Evaluating these energetic quantities by mode (Table 3.2) shows that on offshore lines SL6-SL8 APE is dominated by mode 1, while inshore APE is contained primarily in mode 2. Everywhere (except on line SL8) mode-1 APE exceeds HKE. Examining the higher modes, more complicated patterns are apparent. Compared to APE, a greater proportion of HKE is contained in modes 2 and 3, especially on nearshore lines SL2-5. For modes 2-5, depth-integrated energy tends to increase moving towards the canyon head. $c_g E/F$ ratios for each mode indicate significant reflection for modes 1 (Fig. 3.4d) and 2 (except on lines SL5 and SL8, where mode 1 waves are progressive), while for the higher modes $c_g E/F$ is closer to unity throughout the system suggesting that high-mode waves may be more progressive in character than their low-mode

counterparts.

Table 3.2: Modal break down of average depth-integrated energy flux (F_n, W/m), energy (E_n, J/m), kinetic energy (HKE_n, J/m), and potential energy (APE_n, J/m) and theoretical group speed ($c_{g,n}$, m/s) and $[c_gE/F]_n$ from the location nearest the canyon axis (n indicates mode number).

	SL2	SL3	SL5	SL6	SL7	SL8
F_1	102	110	176	76	181	106
F_2	19	67	43	18	32	16
F_3	71	5	13	28	17	3
F_4	11	1	12	9	3	2
F_5	3	1	1	2	2	1
E_1	258	370	265	580	401	177
E_2	600	600	613	90	119	126
E_3	283	165	162	130	85	85
E_4	115	28	42	121	39	24
E_5	20	8	10	33	30	16
$c_{g,1}$	0.52	0.41	0.54	0.58	0.70	0.61
$c_{g,2}$	0.26	0.21	0.27	0.29	0.35	0.31
$c_{g,3}$	0.17	0.14	0.18	0.19	0.23	0.20
$c_{g,4}$	0.13	0.10	0.13	0.14	0.17	0.15
$c_{g,5}$	0.10	0.08	0.11	0.12	0.14	0.12

	SL2	SL3	SL5	SL6	SL7	SL8
$[c_gE/F]_1$	1.6	1.7	0.8	4.4	1.5	1.0
$[c_gE/F]_2$	8.3	1.8	3.8	1.4	1.3	2.4
$[c_gE/F]_3$	0.7	1.2	1.2	0.9	1.2	1.1
$[c_gE/F]_4$	1.4	3.0	0.8	0.8	1.3	1.5
$[c_gE/F]_5$	0.8	1.0	1.0	1.5	2.5	1.2
HKE_1	34	51	102	30	43	85
HKE_2	98	206	116	66	42	82
HKE_3	109	32	69	54	32	55
HKE_4	31	13	23	59	14	17
HKE_5	8	4	4	20	8	12
APE_1	224	326	155	288	375	80
APE_2	488	349	411	35	76	40
APE_3	174	87	145	71	64	23
APE_4	84	14	19	55	17	11
APE_5	11	4	6	9	11	5

At MP1, which is located at the meander just offshore of line SL6 where $c_gE/F > 1$ indicates a partially standing wave (Fig. 3.4d), the diagnostics for reflection suggest a pattern similar to that discovered in the modal analysis of SL1-8. During the time period corresponding to shipboard observations, $c_gE/F < 1$ for mode 1, in mode-2 c_gE/F transitions mid-week from being close to 1 to being less than 1, and in the high modes c_gE/F hovers around 1 (Fig. 3.6). Where the lowest modes exhibit the characteristics of a partially standing wave, high mode waves are largely progressive.

High mode waves are not only robustly progressive, but they show a robust pattern in that their energy fluxes are directed down-canyon while mode-1 energy fluxes are directed up-canyon. Similar to findings by *Nash et al.* [2004] over the continental shelf, at this location energy flux in mode 1 is directed *up-canyon*, while higher-mode fluxes are directed *down-canyon* (Fig. 3.6, roseplots). This pattern is consistent throughout the full 5-week span of measurements at MP1, and is indicative of reflection of low mode waves and scattering into high modes.

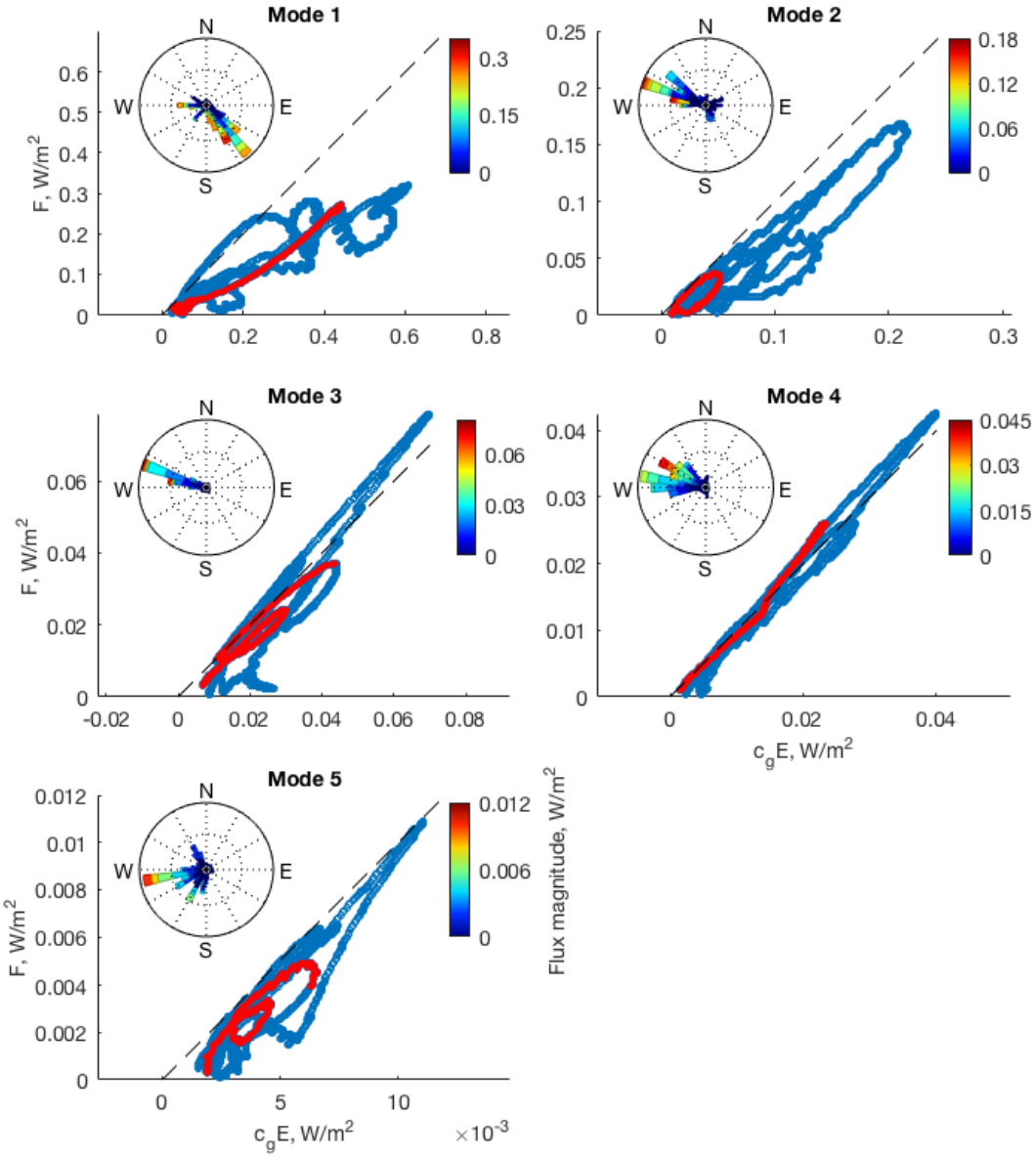

Figure 3.6: Modal analysis at MP1. (a-e) c_gE vs. F for modes 1-5 (blue dots). Red dots indicate measurements taken during the period of shipboard sampling. (f-j) Roseplots of energy flux amplitude and direction for mode 1-5. Note the difference in scale bars between the plots.

3.4.4 Turbulence

Over the LJCS as a whole, dissipation was elevated with an average depth-averaged value $\varepsilon = 3.4 \times 10^{-8}$ Wkg^{-1} for all data below the canyon rim; diffusivity ($\kappa_\rho = \varepsilon/N^2$) was

$1.7\times10^{-3}\mathrm{m}^2\mathrm{s}^{-1}$. The spatial distribution of depth-integrated, time-averaged dissipation (ε; Fig. 3.4c) shows that ε increases moving towards the canyon head and is particularly strong near the mouth of the Scripps canyon where the LJCS bifurcates and over the canyon axis at the head of the system.

Examining the vertical structure of tidally-averaged dissipation (Fig. 3.5), two major patterns are apparent. On the offshore lines (SL6-8), ε is enhanced primarily near the bottom and over the sidewalls of the canyon (Fig. 3.2c, Fig. 3.5a-c), and enhanced dissipation occurs primarily in conjunction with strong up-canyon flows. Very little dissipation was observed during the occupation of line SL7, which was sampled at the beginning of the experiment during neap tide and likely represents a lower bound for tidally-driven turbulence at that location.

In the following sections we discuss several processes that may explain the turbulence patterns apparent in Fig. 3.2c,e.

Internal tide breaking near local generation

Depth-integrated ε was also enhanced over the sidewalls of the canyon, particularly near the depth of the canyon rim. On lines SL5 and SL6 that sidewall enhancement was skewed with stronger dissipation over the Southern rim; on line SL6 there was an order of magnitude more depth-averaged dissipation over the southern flank ($2.5\times10^{-7}\mathrm{W\ kg}^{-1}$) compared to the northern flank ($3.3\times10^{-8}\mathrm{W\ kg}^{-1}$). At locations above the canyon rim, the highest values of ε near the bottom occurred in conjunction with velocities oriented in the up-slope direction and consistent with conditions for conversion from surface to internal tides. Nearfield turbulence due to turbulent boundary layers, breaking waves, and internal hydraulic jumps is often observed when tides interact with topography, as studies by *Pinkel et al.* [2006]; *Klymak et al.* [2008]; *Nakamura et al.* [2010] have shown.

The observed asymmetry between dissipation over the northern and southern flanks of the canyon agrees with the sense of asymmetry *Zhang et al.* [2014] report from hydrostatic

models of idealized shelfbreak canyons forced with alongshore-uniform barotropic M_2 tidal boundary forcing. In their study, they find that cross-canyon distributions in tidal conversion are asymmetrical due to multiple-scattering effects on one side of the canyon rim. The rotation of the direction of barotropic tidal currents creates phase variation in spatially distributed internal-tide sources. The curvature, then, of the right hand (in this case, southern) side of the canyon creates resonant internal-tide generation. Because the generation process is generally associated with localized dissipation, an asymmetry in the strength of turbulent dissipation would be expected to be asymmetric in the manner that was observed here.

Internal wave shear and strain

In a tidally-averaged sense, the vertical structure of dissipation on nearshore lines (SL2, SL3, & SL55) exhibited enhanced ε throughout the water column (Fig. 3.5d-f). In time series from SWIMS, we observe downward phase propagation of the semi-diurnal tide and a mid-depth patch of dissipation that moves downward with the phase of the internal tide and in conjunction with up-canyon flows in a mid-depth layer. A relationship between velocity shear and enhanced dissipation is visually apparent in the raw time series data (Fig. 3.2d,e).

The association between dissipation and strain is clearly demonstrated by probability density functions (as in *Alford and Pinkel* [2000b]; Fig. 15) that are skewed more towards higher strain values and up-canyon velocity (e.g. Fig. 3.7b,d) when considering overturning regions and high values of ε. On all lines wherever 4-m Ri fell below 0.25 (the threshold value below which shear instability is possible), ε was 2-5 times greater than the average value on that line. As expected, values of Ri falling below 0.25 are more probable when considering overturning regions and high values of ε than for the dataset as a whole (Fig. 3.7a). The PDF of shear is also skewed slightly towards higher values when considering only overturning regions (Fig. 3.7c) indicating that isopycnal strain as well as some shear are primarily responsible for creating conditions for enhanced dissipation, as first found by *Alford and Pinkel* [2000b].

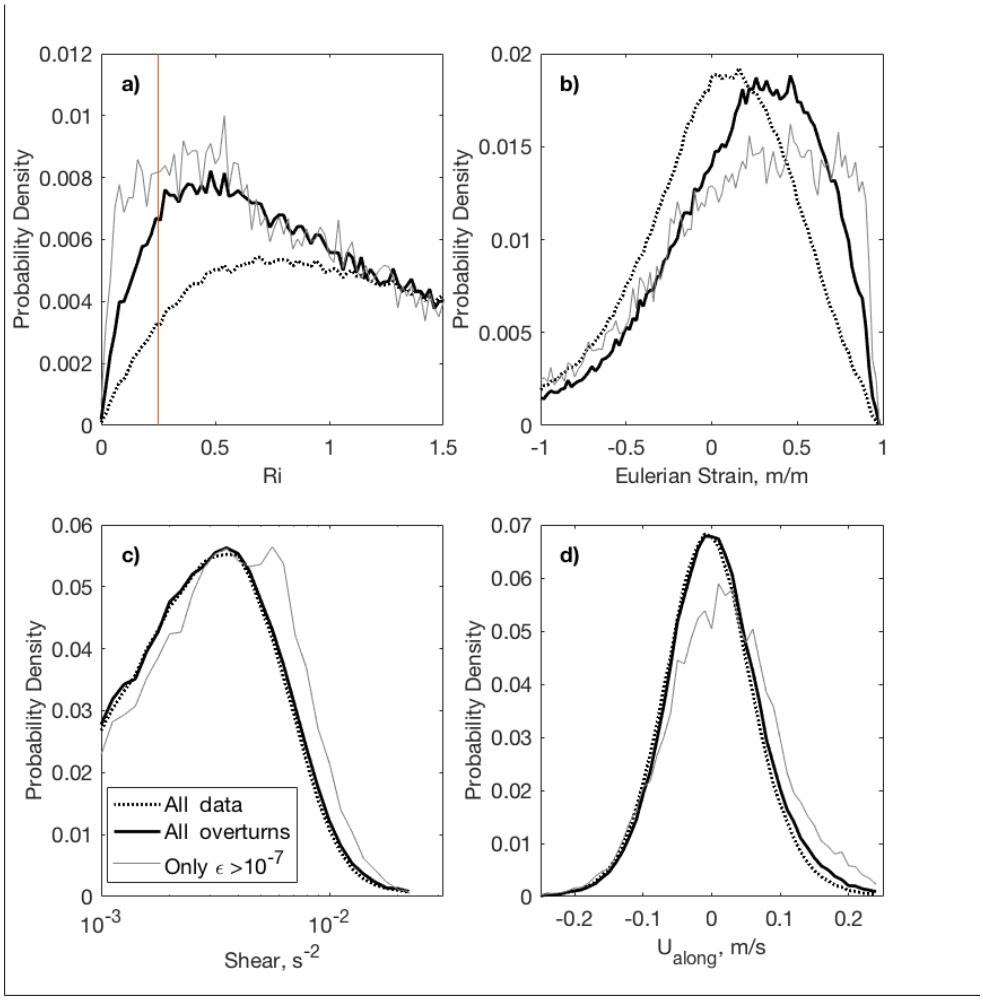

Figure 3.7: Normalized probability distribution functions for (a) 4-m Richardson number, (b) strain, (c) 4-m squared shear, and (d) up-canyon velocity. The dotted line is for all data collected along line SL5, the solid black line represents only data associated with detected overturns, and the thin grey line is only for data associated with a value of dissipation higher than $\varepsilon = 10^{-7}$ W/kg. The red line in (a) is the threshold value (Ri=0.25) below which shear instability is expected.

3.4.5 Canyon Energy Budget

After adjusting terms 2-4 of equation 3.7 for spring-neap changes in overall energy in the system, the along-canyon energy budget is assessed. In general, area-integrated semi-diurnal energy flux decreases from off- to on-shore (Fig. 3.8a), except that there is a jump in up-canyon energy flux along SL5. Conversion is computed both from the observed bottom pressure

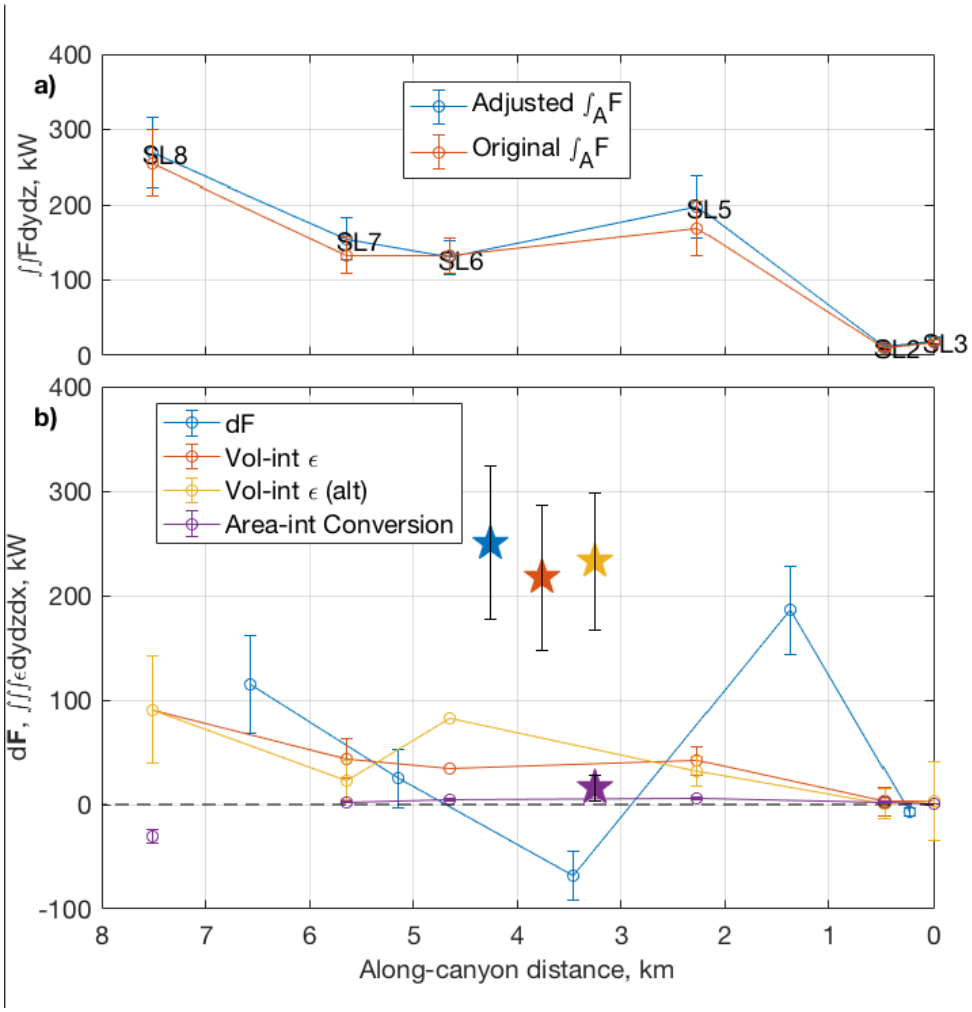

Figure 3.8: Energy budget for the La Jolla Canyon System. Top: Semi-diurnal energy flux integrated over the canyon cross section calculated from observed values (blue line) and values adjusted to account for temporal changes in energy storage (red lines). Bottom: Along-canyon energy flux convergence (blue line), dissipation integrated in the volume between adjacent lines (red and yellow lines), conversion (purple line). Colored stars indicate the canyon-integrated value for the corresponding quantity. Note: for conversion, this total quantity does not include the value of the furthest offshore line (SL8). For each SWIMS lines 2-3 and 5-8 quantities are plotted vs.their distance away from the canyon head.

perturbations ($p'_b(y)$) and barotropic velocities (u_{BT}) at each station, and over the whole region assuming an average p'_b and u_{BT} everywhere. For both methods, conversion from barotropic to baroclinic motions is $\leq$5kW on any given line (in agreement with values computed by *Ponte and Cornuelle* [2013]) and small relative to dissipation and flux terms. Except for those lines surrounding the flux increase on SL5, the observed dissipation integrated in the volume between

lines balances the observed flux convergence within error bars (Fig. 3.8b). Because we assume that the dissipation observed on one line extends between lines, two estimate of volume integrated ε are presented – on integrating in the space towards the canyon head and one towards the canyon mouth (ε_{alt}). Considering the system as a whole, the convergence of flux from mouth (SL8) to head (SL2) is balanced by dissipation integrated over the canyon volume (Fig. 3.8b, stars), putting an upper bound on energy siphoned to frequencies not captured by the harmonic analysis.

3.5 Discussion

The classical theory of internal waves in canyons describes waves that focus towards the canyon head and floor where they eventually break [*Hotchkiss and Wunsch*, 1982]. Our analysis of the La Jolla Canyon System, to the contrary, suggests that steep topography along the sidewalls of a meander and at the head of the canyon system lead to reflection of incident low-mode internal waves and scattering to higher modes. The observed increase in flux between lines SL6 and SL5 could arise from conversion from barotropic to baroclinic motions occurring over the canyon's sidewalls to the east of the meander, but this is unlikely given the relatively small amount of conversion computed (Fig. 3.8b). More likely, partial reflection of the M_2 tide occurs from the steep, eastern side of the canyon wall between SL6 and SL5 leading to lower net fluxes offshore, but higher flux inshore representing only the unreflected fraction of the incident wave. Flux then continues to decrease moving towards the canyon head due in part to further reflection from the canyon head, but also due to dissipation acting to degrade both the incident and reflected waves.

Although not examined closely in this dataset, the reflection process can also siphon energy to the higher harmonics of the fundamental wave [*Rodenborn et al.*, 2011]. This energy siphoning would contribute to flux convergence apparent in the semi-diurnal band (examined in Fig. 3.8), but the finding that dissipation balances flux convergence on the whole suggests that these higher frequency waves by and large do not escape the system, but dissipate their energy

therein. They can (and seemingly do) carry energy away from the reflection point and cause breaking at depths and locations not predictable by considering semi-diurnal flux convergence alone.

The criticality of a given slope is determined relative to the propagation angle of an incident wave (which is set by the near bottom stratification and the frequency of the wave). Waves of higher frequency have steeper propagation angles such that topography that may be reflective to the fundamental wave frequency can be critical or subcritical to the higher harmonics. These waves, then, may propagate further up-canyon and break near steeper topography there. They may also undergo critical breaking over the steeper canyon walls, leading to elevated dissipation higher in the water column.

3.5.1 Inter-canyon comparison: Monterey, Eel, and La Jolla

Monterey Canyon, Eel Canyon (EC), and the La Jolla Canyon System are all fairly well-sampled shelf-incising canyons located on the west coast of the United States. The three have distinct geometry, and the physical processes observed in each differ somewhat. A detailed comparison of the three is offered here.

One primary distinction for this set of canyons is that both MC and EC extend to and incise the continental slope, while the LJCS is confined to the shallower shelf and does not interact with isopycnals in the deep ocean. MC is in all dimensions nearly quadruple the size of the relatively small LJCS (Table 3.5.1); EC is not much longer, but is as deep as MC at its offshore extent. Where LJC has only one large bend in its axis, MC and EC exhibit several meanders, and MC is the trunk off of which multiple branch canyons stem. Despite the size discrepancy, MC, EC, and LJCS share some key characteristics: all are shelf-incising canyons that lie poleward of the turning latitude of the diurnal frequency band. Waves of semi-diurnal frequency, which are free to propagate at these latitudes, are expected to dominate the baroclinic tidal signal in all three.

Table 3.3: Characteristics of Monterey Canyon, Eel Canyon, and the La Jolla Canyon System

	Monterey Canyon	La Jolla Canyon System	Eel Canyon
Length [km]	97	24	30
Width [km]	21	3	3
Depth [m]	1600	650	1500
S_{head}	0.05	0.1	0.15
F_{mouth} [kWm^{-1}]	5	0.2	7.6
$\bar{\varepsilon}$ [W kg^{-}1]	4×10^{-8}	3.3×10^{-8}	4.3×10^{-8}

The differing bathymetry exhibited by the canyons, accordingly, causes different expectations for how semi-diurnal internal tides should behave within their walls. All have steep sidewalls that should reflect M_2 waves towards the canyon floor, and their thalwegs are subcritical to the semi-diurnal internal tide at the canyon mouth given the bottom slope and usual near-bottom stratification (not shown). As a fraction of its length, though, MC is mostly subcritical to semi-diurnal internal waves where LJCS is proportionally much more supercritical (Fig. 3.9). Because of its subcritical geometry, M_2 internal waves in MC are expected to progress forward to the head of the canyon where they may later break at critical bathymetry. (Changes in stratification within the canyon, though, can shift the criticality of the topography enough to make the same slopes reflective [*Petruncio et al.*, 1998; *Zhao et al.*, 2012].) Observations made by *Wain et al.* [2013] align well with this expectation – turbulent hotspots in their study of the upper MC were primarily in the bottom 300m near critical reflection points and near topographic features that induce hydraulically controlled flows. HKE/APE ratios in MC are closer to that of freely propagating M_2 waves at that latitude and actually *increase* moving from off- to on-shore as baroclinic velocities strengthen while isopycnal displacements remain constant; the opposite is true for the LJCS.

In the steeper EC and LJCS, on the other hand, M_2 waves are expected to partially reflect and generate partly standing wave patterns. In LJCS, such reflection was observed by *Alberty et al.* [2017] and in this experiment, where isopycnal displacements become large moving towards

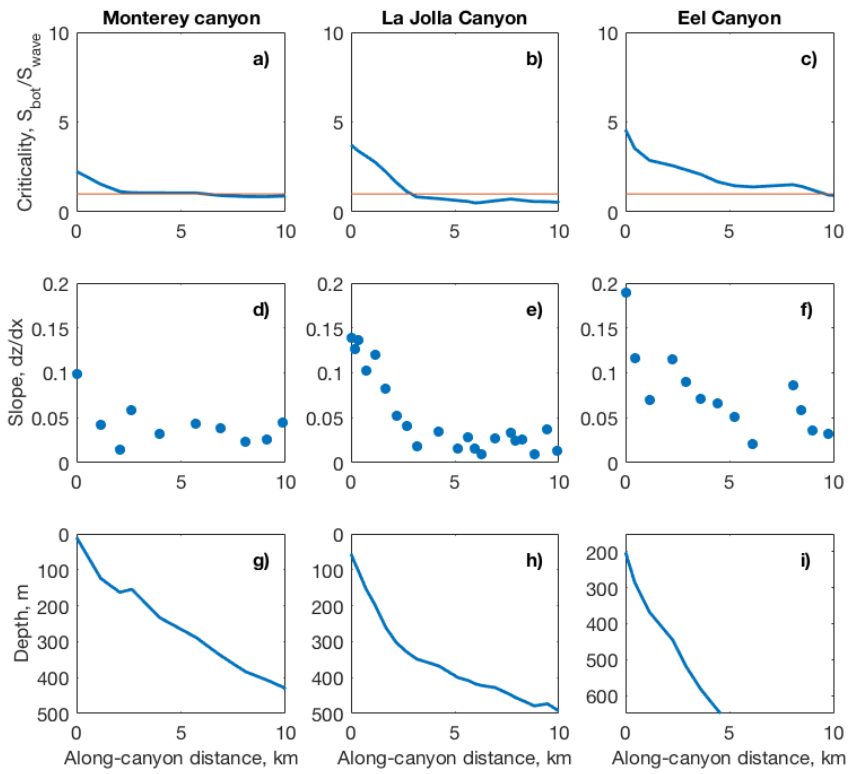

Figure 3.9: Comparison of bathymetry in the 5 km closest to the canyon's nearshore terminus in MC, EC, and LJC. (a-c) Criticality, (d-f) up-canyon slope, and (g-i) thalweg depth are plotted vs.along-canyon distance for MC (left), LJCS (center), and EC (right). The red line in (a) indicates where the slope of the bathymetry is exactly critical to a semi-diurnal internal wave propagating into near-bottom stratification of $N^2 = 10^{-4.5} s^{-2}$.

the head of LJC causing decreasing HKE/APE ratios and belying standing wave patterns there. In conjunction with steepening waves, reflection leads to mid-depth turbulence near the head of the canyon that accounts for a large portion of the dissipation observed in the canyon system as a whole. In LJCS, the enhancement of dissipation near the bottom is much weaker than in MC. Patterns of turbulent enhancement at mid-depths and semi-diurnal frequency, similar to those in the LJCS, are reported near the head of EC [*Waterhouse et al.*, 2017].

In addition to differences in reflectivity and turbulence patterns, the presence of high modes in velocity and HKE toward the head of the LJCS was not reported by *Wain et al.* [2013] from their observations near the head of MC. Time series presented by *Petruncio et al.* [1998]

(see Figures 9 and 10 therein) made in 400m water depth near the head of MC, however, do qualitatively demonstrate high mode velocity structure. Such structure is not expected in a paradigm where incident mode-1 waves simply enter and dissipate at a critical breaking point somewhere up-canyon, but is consistent with a reflected wave that scatters into higher modes. In velocity time series made nearest the head of Eel canyon by *Waterhouse et al.* [2017] (see Figure 6 therein), multiple flow reversals become apparent as do periods of mid-depth turbulence. From along-canyon SWIMS surveys conducted by *Gregg et al.* [2011] in Ascension Canyon (a canyon with mostly supercritical thalweg slope) multiple flow reversals become apparent approaching the canyon head (see Figure 13 therein). Although it has not been analyzed in great detail in previous observations, the presence of high-mode velocity structure near the head of these canyons appears to be a common feature. It is interesting to contemplate wherefrom that structure arises and whether it influences the pattern of mid-depth turbulence near the canyon head reported by *Alberty et al.* [2017]; *Waterhouse et al.* [2017] and this work.

3.5.2 A mechanism for enhanced turbulence: Internal tide reflection, scattering, and mid-depth breaking

Profiles collected at MP1 over a sustained period of 5 weeks demonstrate a relatively robust pattern in which mode-1 internal tides contain most of the energy and flux and are partially standing. Higher-mode waves containing less energy are progressive with energy fluxes oriented down-canyon (Fig. 3.6). Because there appears to be negligible up-canyon propagation in the higher modes, the most likely hypothesis to explain the observed patterns is that a low-mode incident wave enters the canyon and is partially reflected and scattered into high modes that propagate back down-canyon before dissipating. The observation of partially standing waves offshore of both the large meander and the canyon head (but progressive low mode waves along line SL5) suggests that reflection occurs in two locations – first, there is a wall-like effect at the meander where the length scale of the radius of curvature is too small for longer low mode

wavelengths to progress forward; second, there is a reflection from the canyon head where bathymetry steepens and becomes supercritical inshore of the bifurcation point.

2-D models run by *Muller and Liu* [2000] of internal waves encountering a shelf with variable steepness, shape, and depth show for their parameter space that for an incident mode-1 wave, energy transmitted onto the shelf in mode 1 is much smaller than that of the incident wave and that proportionally even less energy is scattered into forward-transmitted high mode waves. A significant fraction of the reflected energy is scattered to mode numbers higher than the incident mode number (see Figure 10 therein). This paradigm is also suggested in observations made by *Nash et al.* [2004] on the continental slope of the Mid-Atlantic Bight. There, convergence of low-mode, semi-diurnal onshore energy flux is approximately balanced by a divergence of high-wavenumber semi-diurnal offshore energy flux, and dissipation rates observed at that location ($O(1\times10^{-8)}Wkg^{-1}$) suggested that the high-mode reflected waves should dissipate on the timescale of ~1 day. Even stronger dissipation rates are observed at the head of the LJCS ($O(1\times10^{-7.5})Wkg^{-1}$) and in Eel Canyon ($O(1\times10^{-7})Wkg^{-1}$) where we would expect topographic focusing of internal waves to lead to additional shear and strain and subsequent breaking events. Scattered high-mode waves would dissipate on a relatively short timescale and would only travel a finite distance down-canyon. In longer canyons such as Eel and MC, high mode waves may not be apparent further offshore, which is consistent with the observations made to date.

The mechanism we propose here is consistent with a simple analytical model proposed by *Waterhouse et al.* [2017] in which an incident wave enters a canyon, reflects from its steep head, scatters, and dissipates completely before reaching the offshore extent of the canyon. Evidence from the modal analysis presented in this study hones in on a specific (and potentially ubiquitous) mechanism by which internal waves encountering a submarine canyon dissipate their energy. Many submarine canyons steepen sharply at their nearshore terminus, and it is possible that focusing, reflection and scattering that cause enhanced shear and strain near the canyon head

and lead to strong mid-depth turbulence is a commonality between them. Although spatially the location of enhanced breaking and turbulence is similar to that expected from the theoretical model proposed by *Hotchkiss and Wunsch* [1982], that turbulence is distributed throughout the water column instead of at critical breaking points near the bottom. Strong turbulence and mixing at mid-depths could strongly influence regional buoyancy fluxes as well as the distribution of enhanced nutrients and benthic larvae that are often found in and around submarine canyon systems.

3.5.3 Contextualizing canyon turbulence

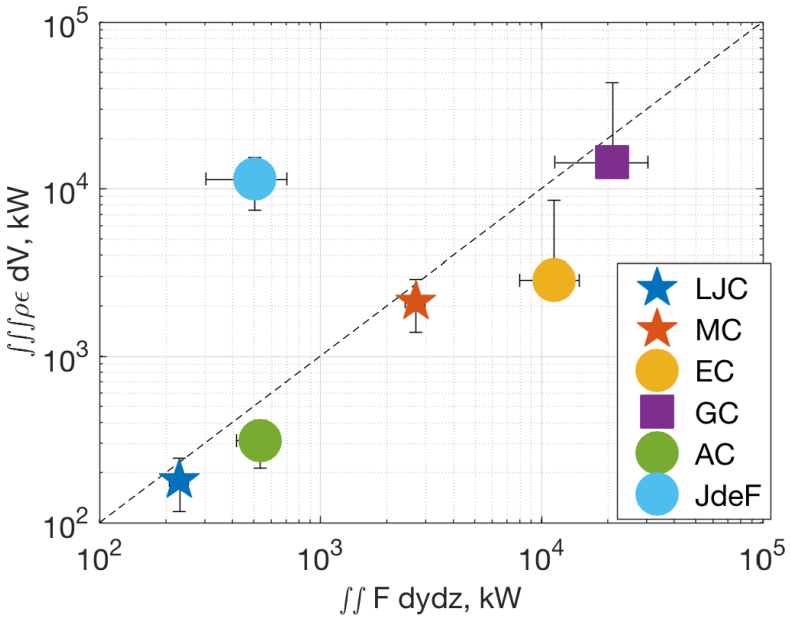

Figure 3.10: Area-integrated up-canyon energy flux at the canyon mouth vs volume integrated dissipation for La Jolla Canyon System (LJC; blue star), Monterey Canyon (MC; red star), Ascension Canyon (AC; green dot), Eel Canyon (EC; yellow dot), Juan de Fuca Canyon (JdeF; blue dot), and Gaoping Canyon (GC; purple square). Dots indicate canyons for which measurements were made only along the canyon axis. Stars indicate canyons in which tidally-resolving, cross-canyon surveys were conducted. Squares indicate measurements of flux and dissipation that were sporadic in space and time.

The observations presented here represent the first comprehensive examination of internal

tides and turbulence in the LJCS, which is only the sixth submarine canyon in which some measure of both dissipation and internal tide energy flux has been made (those that have one or the other are not considered). The others include Monterey Canyon (MC; *Wain et al.* [2013]), Ascension Canyon (AC; *Gregg et al.* [2011]), Eel Canyon (EC; *Waterhouse et al.* [2017]), Juan de Fuca Canyon (JdeF; *Alford and MacCready* [2014]), and Gaoping Canyon (GC; *Lee et al.* [2009]). Although all of these were sampled using different instruments and sampling configurations, we can make some simplifying assumptions and use the values obtained for flux and dissipation for comparing and contextualizing their energetics. If we assume that the measured value of ε averaged over space and time occurs uniformly throughout the canyon's volume and integrate thereover ($\rho \int_V \langle \overline{\varepsilon} \rangle dV$), and that the average value of up-canyon energy flux incident at the canyon mouth occurs everywhere along the cross-sectional area of the canyon mouth ($\int_A \langle \overline{F}_{up-canyon} \rangle dA$), we can compare these roughly estimated terms of the canyon energy budget (Fig. 3.10).

Despite the fact that these canyons differ in location and geometry and are exposed to a wide range of internal wave energy flux from offshore, the markers in Fig. 3.10 mostly fall just below the 1:1 line, which indicates that most energy flux incident at the canyon mouth is balanced by volume-integrated dissipation. The exceptions include Eel Canyon (where dissipation was observed only over the canyon axis and accounts for one quarter of the incident flux [*Waterhouse et al.*, 2017]) and Juan de Fuca Canyon. JdeF is a "long" canyon (it cuts inshore of the coastline and turns into the Puget Sound), and in it tides are weak but cross-shore pressure gradients drive strong subtidal up-canyon flows [*Denman et al.*, 1981; *Waterhouse et al.*, 2009]. A sill within the canyon induces a hydraulic jump, and the majority of the observed turbulence occurs there [*Alford and MacCready*, 2014]. Because of the non-tidal nature of these conditions, we expect dissipation to exceed internal wave energy fluxes as shown in Fig. 3.10.

Although the relationship shown here is based on very simplified metrics, it suggests that anynon-reflected internal wave energy that enters a canyon at the offshore extent is primarily dissipated within the canyon walls rather than depositing any significant energy into small scale

processes or flows on the adjacent shelf.

3.6 Summary and conclusions

Measurements of velocity, density, and turbulence made throughout the La Jolla Canyon System were made in order to characterize the dynamics that drive enhanced mixing in this submarine canyon system. The most important results are summarized here:

- The La Jolla Canyon System is relatively steep and reflective to the semi-diurnal tide. Mode-1 waves exhibit a partially standing character offshore of its meander and head, while higher modes tend to be progressive in character and directed offshore, suggesting reflection and scattering of incident low-mode waves.

- Semi-diurnal energy flux in the system–which is primarily in mode 1–is largely up-canyon. Flux integrated over the cross-sectional area of the canyon at each line decreases from offshore (240 kW) to onshore (5 kW). Smaller energy fluxes are apparent in higher modes and are mostly oriented down-canyon.

- An increase in flux between lines on- and off-shore of the canyon's meander suggest partial reflection and partial transmission of the incident low-mode wave from the steep topography at the meander.

- The highest values of depth-averaged and depth-integrated dissipation occur within 3km of the canyon head and are associated with high strain and up-canyon velocity.

- Offshore, turbulence is enhanced primarily near the bottom and over the sidewalls; onshore, turbulence occurs at mid-depths and is associated with periods of high shear and strain.

- Although flux convergence between adjacent profiles is not always balanced by the dissipation observed locally, flux convergence over the canyon as a whole is balanced by

dissipation over the volume of the canyon–a finding that is consistent with limited observations available from other canyon systems.

From this set of tidally-resolving, cross-canyon measurements, the observed patterns in flux and its partitioning between the modes suggests that mode-1 waves incident on the canyon reflect and scatter backwards at a sharp bend along the canyon axis and at the head of the canyon where the thalweg becomes very steep. High-mode reflected waves induce additional shear and strain, leading to enhanced turbulence near at mid-depth near the canyon head. A review of data presented in previous canyon studies suggests that enhanced mid-depth mixing may be prevalent in both shelf-incising and slope canyons.

The distribution of dissipation both laterally and in the vertical has important implications for regional water mass transformation and biological interactions near canyons worldwide. For slope canyons that connect to deep isopycnals, understanding the physics and correctly parameterizing the distribution of mixing driven by internal waves in canyons could greatly improve our ability to represent and accurately predict future changes in ocean circulation and heat storage [*Melet et al.*, 2013].

3.7 Acknowledgements

This chapter, in part, is currently being prepared for submission for publication of the material. Hamann, Madeleine M.; Alford, Matthew H.; Lucas, Andrew J.; Waterhouse, Amy F. The dissertation/thesis author was the primary investigator and author of this material.

This work was supported by the NSF Graduate Research Fellowship Program, and ship time for this experiment was provided by the UC Ship Funds program. We would especially like to thank Gunnar Voet, Paul Chua, Arnaud LeBoyer, Jonathan Ladner, and Tyler Hughen from the Multiscale Ocean Dynamics (MOD) group at UC San Diego for their time and expertise in

designing, deploying, and recovering moored elements. We greatly appreciate Mike Goldin's assistance and mentorship in preparing turbulence sensors for SWIMS. The captain and crew of the R/V *Gordon Sproul* and R/V *Sally Ride* were instrumental in the success of this field campaign. We would also like to thank Janet Sprintall, Jonathan Nash, Eric Terrill, Geno Pawlak, and Falk Feddersen for generously loaning equipment for our efforts. Shipboard data for this experiment can be found at DOI:10.7284/906929 and DOI:10.7284/907217. Please contact the authors for access to moored datasets.

Chapter 4

Internal tides in a submarine canyon with variable stratification: reflectivity, mixing dynamics, and stationarity

4.1 Introduction

Along continental margins, submarine canyons are common [*Harris and Whiteway*, 2011]. They are known to be hotspots of diapycnal mixing due to their tendency to enhance up- and down-welling flows [*Carmack and Kulikov*, 1998; *Kämpf*, 2006; *Allen and Hickey*, 2010] and to trap and focus internal waves which can later break within the canyon walls [*Hotchkiss and Wunsch*, 1982; *Petruncio et al.*, 1998; *Kunze et al.*, 2002]. Submarine canyons usually have very steep sidewalls and an axis (thalweg) that slopes more gently up towards the coastline in the up-canyon direction so that simple theory predicts that incident internal waves reflect down towards the canyon floor and forward to the canyon head where their energy converges and leads to enhanced breaking near the floor of the canyon head [*Gordon and Marshall*, 1976; *Hotchkiss and Wunsch*, 1982]. Limited observations in the past few decades align with this classical theory

of internal wave progression and turbulence patterns in canyons such Monterey [*Wain et al.*, 2013] and Gaoping [*Lee et al.*, 2009].

In recent studies conducted in Eel canyon [*Waterhouse et al.*, 2017], Monterey Canyon [*Petruncio et al.*, 1998; *Zhao et al.*, 2012], Whittard Canyon [*Hall et al.*, 2017], and La Jolla Canyon System [*Hamann et al.*, 2019], observations indicate that the internal tide in those locations, rather than progressing forward and breaking at the canyon head, is partially standing. As highlighted by *Alberty et al.* [2017] and *Hamann et al.* [2019], reflection signatures at the canyon head coincide with the appearance and prevalence of steep, nonlinear waveforms whose amplitude can exceed half the water depth. Behind their leading edge, isopycnals separate and lead to high strain events at mid-depths with which most of the elevated dissipation is correlated [*Hamann et al.*, 2019]. Instead of being bottom-enhanced (as expected in classical theory) dissipation is elevated throughout the water column.

Studies in Monterey Canyon by *Petruncio et al.* [1998] and *Zhao et al.* [2012] documented both progressive and reflected waveforms at different times, and determined that sub-tidal shifts in stratification force the transition from progressive to reflected waveforms. Because the reflectivity of a given bathymetric slope depends on the ratio of its bottom slope (S_b, which is temporally invariant on the timescale of internal waves) to the slope of the incident wave (S_w, which is a function of wave frequency and the local stratification), if the slope of the bathymetry at a given point is close enough to the average slope of an internal wave in its vicinity (a.k.a near-critical), even small shifts in stratification can alter the fate of an incident wave. However, if S_b is either to steep or too gentle, even extreme stratification changes will not alter the criticality. For canyons with steep enough bathymetry, internal tide reflection would persist through seasonal and sub-tidal stratification shifts – as would the associated turbulence patterns and mechanisms. To date, very few long records exist in canyons–especially for measurements that resolve the timescales of internal waves–so our understanding of the effects of variable stratification on the internal wave climate and mixing processes in canyons is limited.

Due to their prevalence along coastlines and their ability to trap and efficiently dissipate energy from incident internal waves, canyons likely play a significant role in our understanding of the fate of remotely generated internal tides that impinge upon distant margins. Where these waves dissipate and how the associated mixing is distributed in depth have an order one influence on the heat distribution and ocean circulation on global scales [*Melet et al.*, 2016]. On regional scales, buoyancy fluxes and form drag associated with strong mixing in shelf-incising canyons could have a significant influence on circulation and retention times in the inner shelf region.

Canyon mixing also has an impact on local coastal biological productivity that is sensitive to the lateral and vertical distribution of nutrient mixing [*Hales*, 2005; *Avicola et al.*, 2007; *Tanaka et al.*, 2013], and its temporal variability over a range of timescales [*Lévy*, 2008; *Lucas et al.*, 2011]. In general, canyons are found to be hotspots of biological productivity and megafaunal abundance [*Vetter*, 1994; *Vetter and Dayton*, 1999; *De Leo et al.*, 2010] and are often designated as marine protected areas [*Howell et al.*, 2010] and important sites for commercial fisheries [*Sanchez et al.*, 2013]. Productivity and species abundance in canyons is likely the product of a variety of factors (including light and temperature gradients in benthic habitat and shelter for megafauna), but enhanced productivity may be due in part to mixing canyons foster along isopycnals that connect to deep, nutrient waters offshore. As noted by *Alberty et al.* [2017], consistent breaking of internal tides along these nutrient gradients would provide a relatively consistent influx of nutrients to phytoplankton communities that form the basis of an abundant ecosystem [*Lucas et al.*, 2011].

In canyons, internal wave energy levels are often elevated above the canonical Garrett-Munk (GM76) spectrum for internal wave energy [*Garrett and Munk*, 1975; *Cairns and Williams*, 1976; *Hotchkiss and Wunsch*, 1982; *Carter and Gregg*, 2002; *Zhao et al.*, 2012]. This contrasts with the internal wave climate over adjacent open shelf regions. In general, internal waves in the coastal ocean are not very predictable over longer timescales due to the long distances over which they may propagate from their source and the variable currents and stratification they

experience en route [*Nash et al.*, 2012]. Lacking sufficiently long times series, an analysis of the long-term stationarity of internal waves within a canyon has not been possible until now. Using measurements from an unprecedented year-long time series at the head of the La Jolla Canyon System, we demonstrate that, despite its nonlinearity, the stationarity of the internal tide is significantly enhanced in the vicinity of steep canyon bathymetry. Likely due to the phase invariance of internal tide signals we also observe clear spring-neap cycles in energy, dissipation, and even integrated chlorophyll at the head of the canyon system.

4.2 Methods

4.2.1 Observations

The La Jolla Canyon System (LJCS) is a shelf-incising canyon that terminates in the La Jolla Cove just offshore in La Jolla, CA. The greater LJCS is 24km long, 3km wide, and 600m deep at its mouth. Between 8km and 14km from its head the canyon meanders to the south. Two kilometers from its head, the LJCS bifurcates into two branches: the La Jolla Canyon (LJC) extends to the south parallel to the direction of the main canyon axis while the Scripps Canyon (SC) branches off to the north in a direction nearly perpendicular to LJC. Located 1.6 km away, the headland of Point La Jolla sits south of the canyon head blocking strong alongshore flows in the vicinity.

The La Jolla Internal Tide Experiment II (LaJIT2) was executed in the LJCS in September, 2016 (Fig. 3.1). The experiment consisted of 7 days of shipboard surveys (as detailed in *Hamann et al.* [2019]) and moorings deployed on September 10, 2016 at three locations along the canyon axis. MP1 (415m) was located just onshore of the canyon's major meander. MP1 carried a downward-looking 75kHz Workhorse Acoustic Doppler Current Profiler (ADCP) and a McLane moored profiler with SeaBird (SBE) 37 CTD and acoustic current meter (ACM). The McLane made full-depth profiles every 15 minutes, but stopped profiling after 5 weeks. T1 (240m) was

located just onshore of the bifurcation point between the Scripps and La Jolla Canyon branches. T1 carried a downward-looking 75kHz Workhorse ADCP as well as 36 SBE56 thermistors and two SBE37 CTDs spaced 3-8m apart with denser spacing near the thermocline. Stations MP1 and T1 were recovered on December 14, 2016. High resolution (2m) bathymetry data from multibeam sonar were used to map deployments and determine bathymetric gradients [*Dartnell et al.*, 2007].

Station WW (105m) sat at the head of the canyon and was serviced to operate for a full year. The mooring consisted of a WireWalker wave-powered profiler that carried a sideways-looking Aquadopp Acoustic Current Meter (ACM), as well as temperature, conductivity, pressure, oxygen, chlorophyll fluorescence, and backscatter sensors whose high resolution data were everaged into 0.25m bins [*Rainville and Pinkel*, 2001; *Pinkel et al.*, 2011]. WW profiled continuously, spanning the entire water column up to the surface, generating over 35,0000 profiles over the course of the deployment, and averaging 17 minutes between profiles including servicing periods. WW was also equipped with data telemetry system and transmitted its data in real time from September 10 2016 to September 11 2017. Batteries on the WW were replaced every 20-25 days, and each recovery required 1-3 days to service and re-deploy. The ACM on the WW experienced intermittent failures due to power supply issues, so the record of velocity has larger gaps than the other measurements (Fig. 4.1e).

4.2.2 Analysis methods

Wind

Hourly wind velocity measured at the pier is passed through a 3-day lowpass filter to remove diurnal variability. Wind stresses then are computed as $\tau_x = \rho_a C_D u_w$ and $\tau_y = \rho_a C_D v_w$ where ρ_a is an average air density of 1.2 kg/m^3, C_D is a drag coefficient that scales with the magnitude of the total wind velocity, and u_w and v_w are 3-day lowpassed winds.

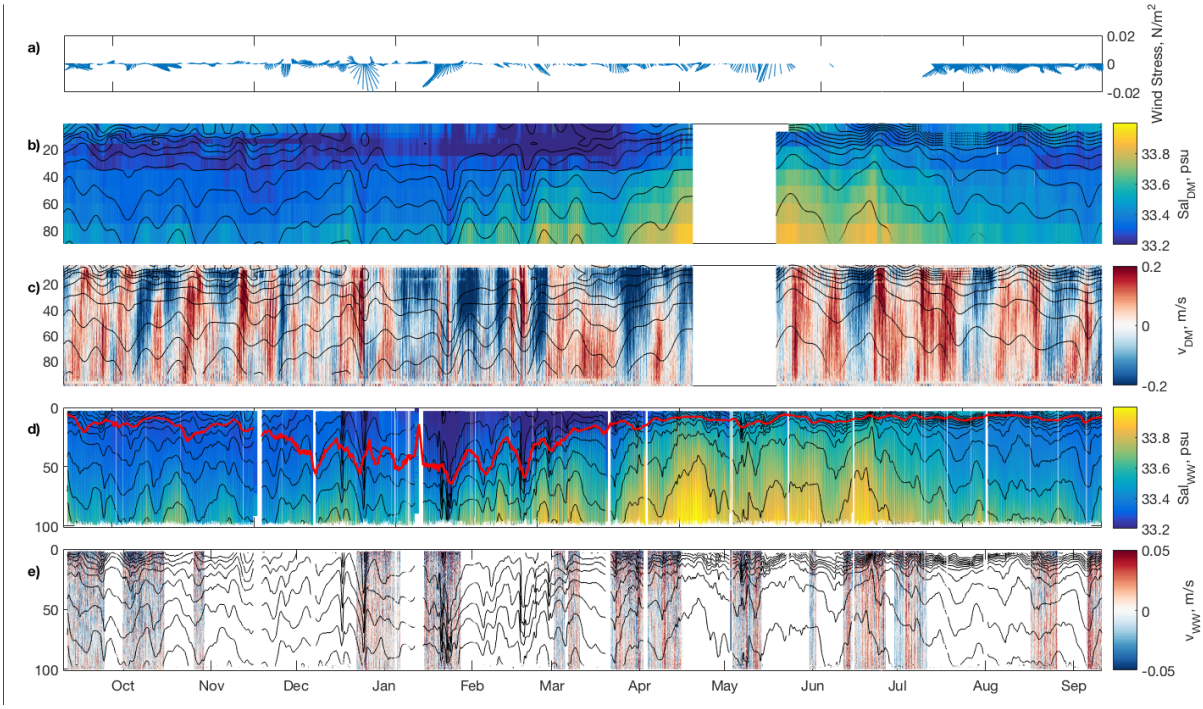

Figure 4.1: Full year timeseries of salinity and 7-day low-passed density contours from (b) Del Mar and (d) the WireWalker. Time series of alongshore velocity at (c) DM and (e) WW demonstrate the gaps in useable data from the Aquadopp on WW throughout the year. 3-day low-passed wind stress is also shown in (a), and the red line in (d) indicates the depth of maximum stratification at WW.

Raw data quantities

Because profile data from the WireWalker and the McLane are collected at irregular intervals, data are interpolated onto regularly spaced grids to conduct any kind of frequency domain analysis. Quantities from the WireWalker are binned every 0.25 m and interpolated to 15 minute intervals. McLane measurements on MP1 are averaged into 1-m vertical bins and interpolated a constant time grid with 10 minute spacing, as are coincident measurements from the ADCP. CTD, thermistor, and ADCP data from T1 are also gridded at 1m and 10 minute.

Buoyancy frequency is computed as

$$N^2(z,t) = \frac{g}{\rho_0}\frac{\delta\overline{\rho}(z,t)}{\delta z}, \tag{4.1}$$

where g is gravitational acceleration, ρ_0 is a reference density of 1026 kg/m^3 ocean water density, and $\overline{\rho}(z,t)$ is density $\rho(z,t)$ smoothed over 4-m vertical window. 4-m vertical squared shear was computed from velocity profiles as $S^2 = \frac{\delta u^2}{\delta z} + \frac{\delta v^2}{\delta z}$. Richardson number was computed from 4-m shear and stratification as $Ri = \frac{N^2}{S^2}$ [*Miles and Howard*, 1964]. Eulerian strain was computed as $\frac{N^2(z,t)}{\langle N^2(z,t)\rangle} - 1$ where angle brackets indicate smoothing over a 2 day window to remove tides [*Pinkel et al.*, 1991]. Low frequency shifts in the density structure at all moorings are calculated using a 7-day lowpass through a fourth order Butterworth filter, and isopycnal displacements ($\eta(z,t)$) are then calculated relative to this slowly varying background density $\overline{\sigma_\theta}$.

Raw data from the ADCPs at MP1 and T1 are used to compute rotary spectra of velocity computed as the multi taper spectrum of complex velocity u+iv. Gridded velocity data from WW (though not useful for analyzing low frequencies due to short operation period during each deployment) are also used to compute rotary spectra. Displacement spectra are computed using gridded values of isopycnal displacement η (calculated as described above). Rotary and displacement data are computed using 20 tapers, and then averaged over a depth range of 20m.

Rotary and displacement spectra computed using 20 tapers, then averaged over a depth range of 20m. The *Garrett and Munk* [1975] model spectrum, as modified by *Cairns and Williams* [1976] (here called GM76) is computed for the average value of N^2 in the corresponding depth range and plotted in the same panel for comparison. Internal waves are expected only for frequencies f ¡ ω ¡ N (dashed). At this location, the diurnal (K_1) frequency is lower than f so that K_1 waves are trapped and evanescent.

Energetics

Available potential energy (APE) and horizontal kinetic energy (HKE) are computed as

$$APE(z,t) = \frac{1}{2}\rho N^2(z)\eta^2(z) \tag{4.2}$$

and horizontal kinetic energy (HKE)

$$HKE(z,t) = \frac{1}{2}\rho|\mathbf{u}^2(z)| \tag{4.3}$$

where ρ is density, H is water depth, and the overline indicates vertical averaging. Total energy (E) is taken as the sum of HKE and APE at any given location and time. Velocity perturbation, $\mathbf{u}'(z,t)$, baroclinic pressure perturbation, $p'(z,t)$, and energy flux $\mathbf{F}(z,t) = \mathbf{u}'p'$ are computed by standard methods following *Kunze et al.* [2002] and *Nash et al.* [2005]. After gridding, semidiurnal signals are isolated by running all measured quantities through a fourth-order Butterworth bandpass filter, with the central frequency at 12.43 hr^{-1} and the cutoff periods of 11.3 to 13.9 hours. Energetic quantities are computed, then, for both the full dataset and for the semidiurnal component (HKE_{M_2},APE_{M_2}, E_{M_2}, and F_{M_2}).

At each mooring, u_{M_2}, v_{M_2}, and η_{M_2} (where the subscript indicates that the semi-diurnal bandpassed quantities are used) are further separated into vertical modes as a function of $N(z)$ following *Gill* [1982]. The equation

$$\frac{\partial^2}{\partial z^2}\eta(z) + \frac{N^2(z)}{c_n^2}\eta(z) = 0 \tag{4.4}$$

with boundary conditions $\eta(0) = \eta(H) = 0$ (where n is mode number, c_n is eigenspeed, and H is water depth) is solved for the first five modes. Semi-diurnal HKE_n, APE_n, and $\mathbf{F_n}$ are computed for each mode where the subscript indicates the mode number. The boundary conditions used here are not strictly valid on a slanted bottom where geometry allows for coupled vertical and horizontal velocities, so computations from modal quantities are examined qualitatively and reservedly in order to identify the persistence of patterns observed in the spatial surveys conducted by *Hamann et al.* [2019].

Reflection

Temporal variability in the reflected character of the incident internal tide is of particular interest, and energetic quantities are assessed in the same manner as in *Hamann et al.* [2019]. The expected ratio of HKE to APE over a wavelength of a progressive (for each individual mode as well in total) is

$$\frac{HKE}{APE} = \frac{\omega^2 + f^2}{\omega^2 - f^2} = 1.92 \tag{4.5}$$

at this latitude [*Gill*, 1982]. If the wave is reflected (or partially reflected), the vertical component of the motion of the interface becomes larger so that the value this ratio decreases. We assess HKE/APE for all computed modes in order to diagnose reflection, by mode.

For a progressive, linear internal wave, group speed (c_g) times energy (E) is equal to energy flux (F). If the wave is partially reflected, fluxes of the opposing wave cancel and the observed ratio of $c_g E/F$ increases [*Alford et al.*, 2006; *Alford and Zhao*, 2007b]. This diagnostic can also be computed by mode. Unlike HKE/APE ratios, this diagnostic is not dependent on the distance from the reflection point, so we use it here as the main indicator of internal tide reflection. Whether a particular bottom slope should be reflective to an internal wave of frequency ω that propagates through near-bottom stratification N^2 is dubbed "criticality" and is computed as

$$\alpha = \frac{s_b}{s_w} = \frac{\delta H/\delta x}{\sqrt{(\omega^2 - f^2)/(N^2 - \omega^2)}} \tag{4.6}$$

where s_b and s_w are the bottom bathymetry and wave slope, respectively, f is the local inertial frequency, $\delta H/\delta x$ is bottom slope in the direction of wave propagation (assumed to be in the up-canyon direction here), N^2 is the value of stratification near the bottom, and ω is the incident internal wave frequency. For moored measurement, temporal changes in criticality are assessed for semi-diurnal waves ($\omega = 12.4$ hr^{-1}) due to sub-tidal changes in bottom stratification $\langle N^2(z_{max}, t)\rangle$ where angle brackets indicate averaging over 2 days.

Dissipation of Turbulent Kinetic Energy

Profiles of ε were estimated at MP1 and WW from observed density overturns measured by the McLane and WireWalker profilers, repsectively, following the Thorpe scale method described in *Thorpe* [1977], *Dillon* [1982], and *Gargett and Garner* [2008]. Although these methods are indirect, past studies have shown good agreement between time-averaged estimates of dissipation from Thorpe scales and microstructure shear profilers [*Ferron et al.*, 1998; *Alford et al.*, 2006]. *Hamann et al.* [2019] use microstructure shear profiler measurements from the La Jolla Canyon region to validate the use of Thorpe scales in this well-stratified coastal region (see Appendix A therein).

At T1, profile data are not available, so an estimate of dissipation rate is made from the 1 Hz moored thermistor measurements following methods laid out by *Zhang and Moum* [2010]; *Musgrave et al.* [2016]. Temperature gradient spectra were computed from 2 minute segments for each of the thermistors, averaged over 3 h and fitted to the canonical spectrum to determine the dissipation rate of thermal variance (ε_χ). This computation requires an estimate of the mean flow across each temperature sensor in order to convert frequency to wavenumber space, and this is determined from the surface ADCP velocity record. Assuming that the turbulent diffusivities of heat and momentum are equal, the turbulent dissipation rate can then be inferred (see *Musgrave et al.* [2016]). Because this method has not been extensively vetted, we do not make quantitative assessments or comparisons with values of ε computed using this method at T1, but rather examine the data qualitatively to glean understanding of the variability of turbulence and the processes that drive it throughout the measurement period.

Harmonic Analyses

Following the methods of *Nash et al.* [2012], harmonic analyses conducted at WW and DM are used to investigate the stationarity and stationarity of internal tides throughout the year. Because the velocity record collected at WW is filled with gaps, we use isopycnal displacement

to represent internal tide motions. After bandpassing data between 6 hour and 30hour periods to isolate tidal motions, we use a harmonic fit of the form

$$H_T(t) = A_{M_2}\cos(\omega_{M_2}(t-t_{ref}) - \psi_{M_2}) + A_{S_2}\cos(\omega_{S_2}(t-t_{ref}) - \psi_{S_2}) \tag{4.7}$$

where A is the amplitude, ψ is the phase and ω the frequency of the lunar semi-diurnal (M_2) and the solar semi-diurnal (S_2) components, and t_{ref} is a common reference time. The fit is conducted over time windows (T) ranging from 3 days to 3 months. For windows less than 15 days, the S_2 component is not resolved.

We consider the predictive capability of a given harmonic fit using its "skill score"

$$SS_T = 100\% \times \left(1 - \frac{\langle \eta - H_T(\eta))^2 \rangle}{\langle \eta^2 \rangle}\right) \tag{4.8}$$

where H_T is the fit for a window of length T and brackets indicate a running average over the length of the fit window and averaging over depth. SS_T assesses how much variance is captured by a given fit; when SS_T = 100%, the fit captures all variance, and when SS_T = 0% it captures none. SS_T can be negative if the harmonic prediction is anti-correlated with the data.

4.3 Results

4.3.1 Oceanographic Context

Measurements available from September 2016 to September 2017 from the WireWalker, the Del Mar mooring, and the SIO pier are drawn on to examine seasonal shifts in currents, stratification, water masses, and wind forcing in the LJCS region. Hourly winds measured from the SIO pier are most often onshore (northwesterly), with some periods of offshore (southeasterly) wind interspersed. During the fall (October to December), winds relax and sometimes weakly

reverse. Moving into winter, winds strengthen and wind reversals are frequent. The strongest wind events are associated with winds of northerly origin. Beginning in February, winds blow persistently from the north, favoring upwelling.

In concert with persistent upwelling-favorable springtime winds, isopycnals uplift and cold, salty water masses appear at depth at both WW and DM (Fig. 4.1b,d). In general, sub-tidal isopycnal displacements and the appearance of different water masses are well correlated between WW and DM (located 22 km to the north). A subsurface salinity minimum is apparent between 10m and 30m depths at both moorings for most of the year (this is typical for this region where fresher high latitude surface waters subduct beneath warm, salty, warm surface waters of tropical origin in the eastern boundary current [*Reid*, 1973]).

At both moorings, the subsurface salinity minimum disappears in the winter as fresh water is input from surface runoff coincident with storms. The winter of 2016-2017 was anomalously wet for the state of California [*Swain et al.*, 2018], and San Diego experienced multiple heavy rainfall events. At WW, these events are apparent as short (1-3 day) periods when near-surface salinity decreases and isopycnals rapidly depress (Fig. 4.1). The most extreme events in December and January impact the entire water column. Before these winter storm events (from September to December), the water column is well-stratified. Strong surface stratification begins to erode in late November. Stratification decreases and the mixed layer depth drops from December to March after which point the surface begins to re-stratify and the subsurface salinity minimum reappears. From April to August, near-surface stratification is strong.

Unlike water mass appearance and sub-tidal isopycnal displacements, velocities at DM and WW are not correlated. Alongshore currents at Del Mar are as expected for a coastal mooring in this region with strong barotropic currents that respond to basin scale events (large scale wind stress and coastally trapped waves) as well as several day periods of two-layer flow likely due to the passage of submesoscale eddies (Fig. 4.1c) [*Nam and Send*, 2011]. At WW, velocities are very weak (1-2 cm/s as compared to 20 cm/s at DM) and sub-tidal, barotropic velocities are

almost non-existent (Fig. 4.1e).

4.3.2 Internal wave climate in LJCS

Spectra

Rotary velocity spectra at T1, MP1, and WW exhibit the strongest peaks at semidiurnal frequency (Fig. 4.2). At WW, the semidiurnal peak is significantly less energetic than those at MP1 and T1 due to the fact that velocities are so much smaller there. At MP1, there is significant energy at low frequencies (7-14 days) in the top 150 m. At both MP1 and T1 a surface-intensified peak is apparent around the diurnal/inertial frequency (which at this latitude are nearly indistinguishable). This peak is more energetic further offshore at MP1. Peaks at the higher harmonic frequencies of the M_2 tide are also apparent, but are more distinct and energetic at the moorings further inshore. Moving up-canyon, the difference between CW and CCW spectra becomes smaller (Fig. 4.2), indicating that tidal motions become increasingly rectilinear moving onshore. Spectra level off indicating a noise floor at approximately 50 cpd at T1 and 30 cpd at MP1. The noise is due, likely, to topographic interference with downward-looking beams (not an ideal configuration for ADCP measurements near abrupt topography.

Spectra of displacement, similarly, exhibit the strongest peaks at M_2, and show more energy at higher harmonic frequencies moving inshore. On the other hand, neither mooring captures a significant peak at near the diurnal/inertial band and no sub-tidal peak in the near-surface is apparent at MP1. At both MP1 and T1, energy in the spring-neap band is elevated near the bottom, as well as near the surface at T1.

At station T1, rotary velocity spectra indicate an internal wave environment elevated 2-3 times above the Garrett-Munk (GM76) spectrum [*Garrett and Munk*, 1975] throughout most of the internal wave frequency range (Fig. 4.3a), consistent with many previous observations of elevated internal wave activity in canyons [*Hotchkiss and Wunsch*, 1982; *Carter and Gregg*, 2002;

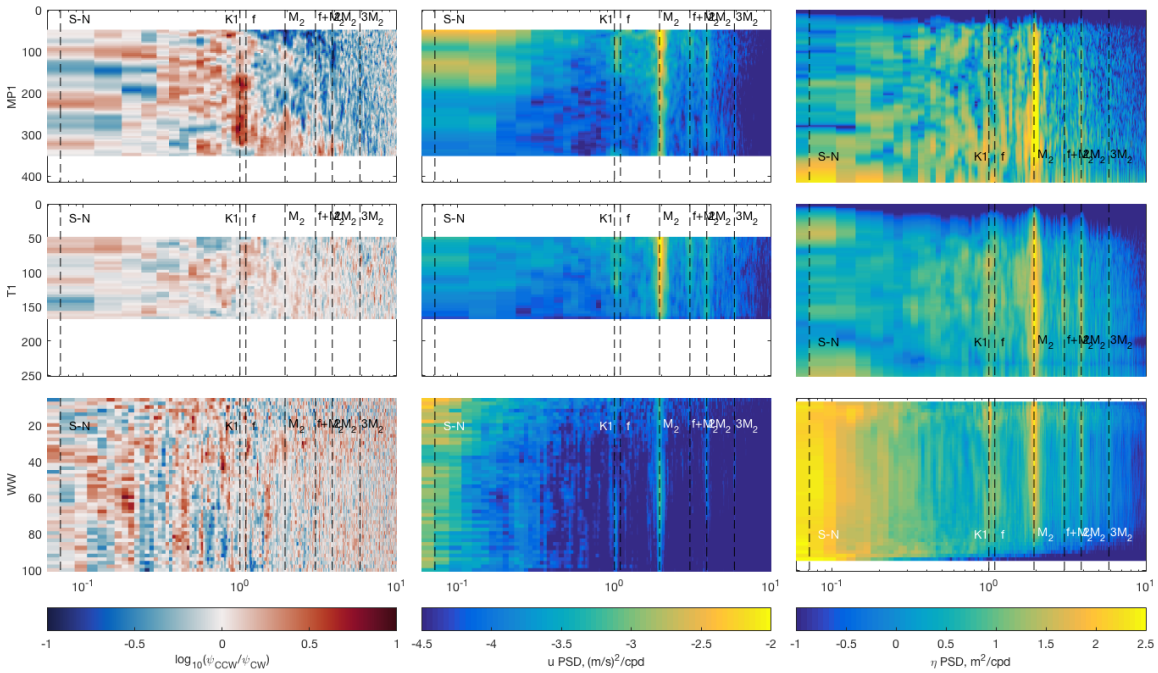

Figure 4.2: Plots of (center) clockwise rotary velocity (ψ_{CW}) and (right) displacement power spectral density for all depths at MP1(top) , T1(middle), and WW (bottom). The ratio of ψ_{CW}/ψ_{CCW} is also shown (left).

Zhao et al., 2012]. A small, broad peak spans the diurnal/inertial range. At MP1, on the other hand, the velocity spectrum is at or below GM76, and the broad peak spanning K_1 and f is much higher relative to the peak at M_2 (Fig. 4.3b). At MP1

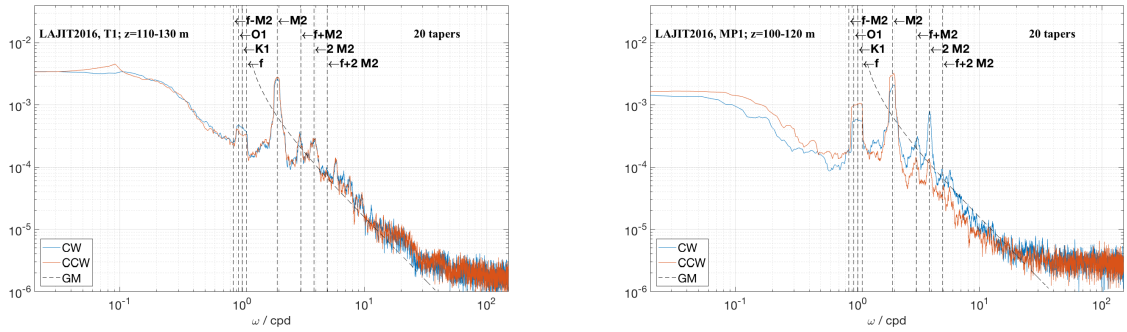

Figure 4.3: Rotary spectra from ADCP measurements on (left) T1 and (right) MP1 overlaid with GM76.

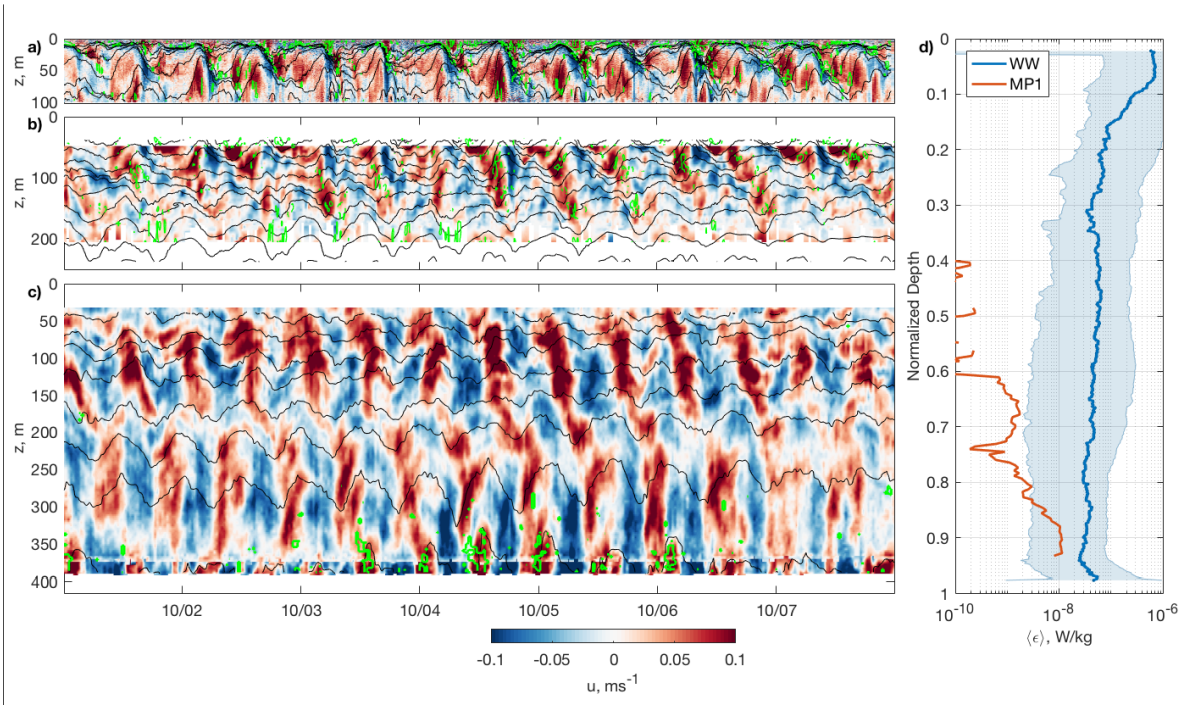

Figure 4.4: Coincident time series of eastward velocity from (a) WW, (b) T1, and (c) MP1 overlaid with isopycnal depths (black, spaced every 0.25 kg/m^3) and contours of $\varepsilon = 10^{-6.5}$(green). (d) Time average of ε from WW and MP1 from the 5 weeks during which MP1 operated are plotted against normalized depth at each location, and error bars shown for WW indicate the maximum and minimum values of a 5-week running mean of ε from its entire year long deployment.

Raw data such as that shown in Fig. 4.4 are bandpassed (using a fourth-order Butterworth filter with zero-phase response, a center frequency at 12.4^{-1} hr^{-1} and quarter-power points at 10.1^{-1} hr^{-1} and 14.8^{-1} hr^{-1}) around the semi-diurnal frequency band that dominates the signal at all moorings in the canyon. At all locations, depth-integrated APE_{M_2} almost alwayds exceeds HKE_{M_2}. Typically, both depth-integrated energy E_{M_2} and energy flux F_{M_2} decrease in magnitude moving onshore, although at the beginning of the measurement period E_{M_2} and F_{M_2} at T1 exceed those offshore at MP1 (Fig. 4.5), consistent with the patterns in energy and flux *Hamann et al.* [2019] computed from spatial surveys surrounding the moorings during this time period.

Depth-integrated energy flux F_{M_2} is generally oriented up-canyon; at T1 and WW, this

is almost always the case, but at MP1 (which is located near a meander and a point of greater canyon width from rim to rim) the direction of energy flux is more variable (Fig. 4.6). Although the strongest fluxes at MP1 are oriented up-canyon and the majority of measured fluxes are in this direction, fluxes in directions spanning the southward swath between up- and down-canyon directions are observed (Fig. 4.6c).

At all locations, semidiurnal energy and flux are typically dominated by mode 1. At MP1 and WW, APE_{M_2} exceeds HKE_{M_2} in all modes. There, 50% of APE_{M_2} is contained in mode 1 while 60% of HKE_{M_2} is in modes 2 and 3. At T1, the opposite is the case: HKE_{M_2} is mode 1 while APE_{M_2} is primarily in modes 2 and 3. The change in the ratio of HKE to APE moving from on- to off-shore is consistent with HKE/APE vs. distance for a fully reflected linear internal wave with a wavelength of 12km. This assumes that the location of reflection is the canyon head (WW)–an assumption that is supported by the observation that $HKE$is nearly zero at WW, and APE far exceeds it at all times as would be expected at the wall node of a reflected wave. The ratio of $c_g E/F$ is also used to qualify the progressive vs. standing character of the wave as it is not dependent on wavelength or distance from the point of reflection. At all locations and all times, $c_g E/F$ exceeds 1 indicating that the M_2 tide is always partially standing throughout the canyon.

Up-canyon evolution of the internal tide and dissipation patterns

Records from three coincident moorings along the axis of the LJCS allows a several week long view of the up-canyon evolution of internal tide waveforms similar to the 2-day view shown by *Alberty et al.* [2017]. Their work uses harmonic analyses to demonstrate that moving from off- to on-shore, internal tide waveforms become increasingly steep and nonlinear and harmonic fits that describe a similar amount of the variance in pressure perturbation at a given depth and for a single tidal constituent at the station furthest offshore require the inclusion of the overtides of the semi-diurnal tide (M_4 and M_6). Fig. 4.4 shows velocity records and isopycnal

Table 4.1: Time-averaged values of depth-integrated semi-diurnal energy, flux, HKE, and APE for modes 1-5 at all moorings.

Mooring	Mode #	Energy (J/m^2)	Flux (W/m)	HKE (J/m^2)	APE (J/m^2)
MP1	1	324.7	123.4	**53.7**	**270.5**
	2	175.7	38.1	72.9	101.2
	3	105.1	21.8	71.3	32.8
	4	75.5	13.2	44.0	30.9
	5	27.4	2.8	17.6	9.4
T1	1	990.2	160.1	**902.9**	**87.4**
	2	720.9	77.4	546.3	174.3
	3	492.9	36.0	380.7	112.5
	4	177.9	10.2	137.4	40.6
	5	71.2	3.1	57.9	13.3
WW	1	178.2	10.0	**2.0**	**139**
	2	119.5	5.2	4.3	86.4
	3	42.6	1.5	2.9	27.8
	4	8.0	0.2	1.1	6.4
	5	5.4	0.2	0.6	3.7

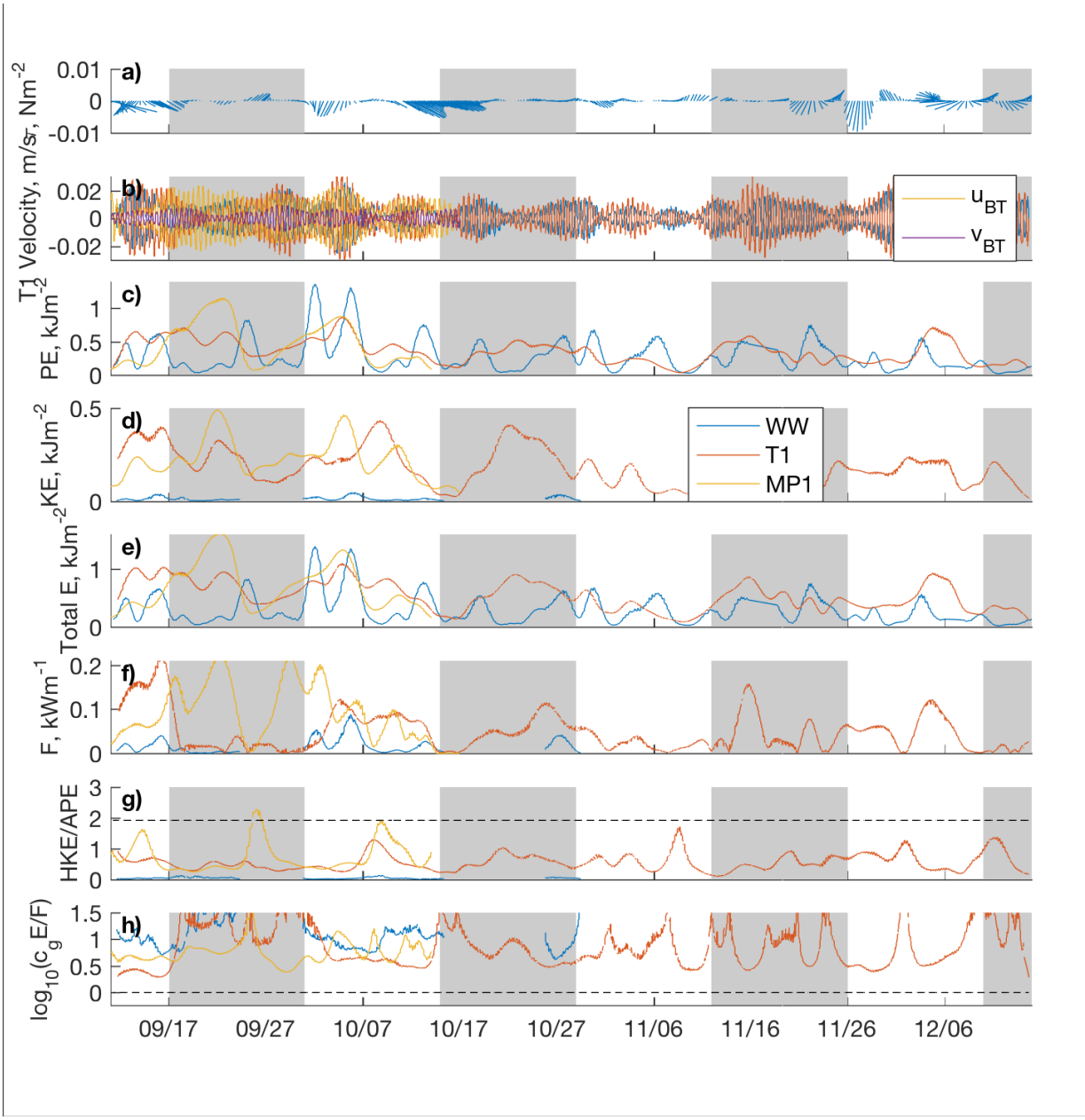

Figure 4.5: Time series of (a) winds, (b) semidiurnal barotropic velocity measured at T1, and integrated semidiurnal (c) KE, (d) PE, (e) total E and (f) flux magnitude, (g) HKE/APE, and (h)$c_g E/F$ for all moorings and between September and and December, 2016. Alternating grey and white bars are spaced at 14-day intervals to reflect the spring-neap cycle.

displacements recorded at the three moorings for a 1-week period in early October that is typical of the measurements made from mid-September to mid-December. As in *Alberty et al.* [2017] isopycnal displacements are visually sinusoidal at MP1, and they become increasingly steep

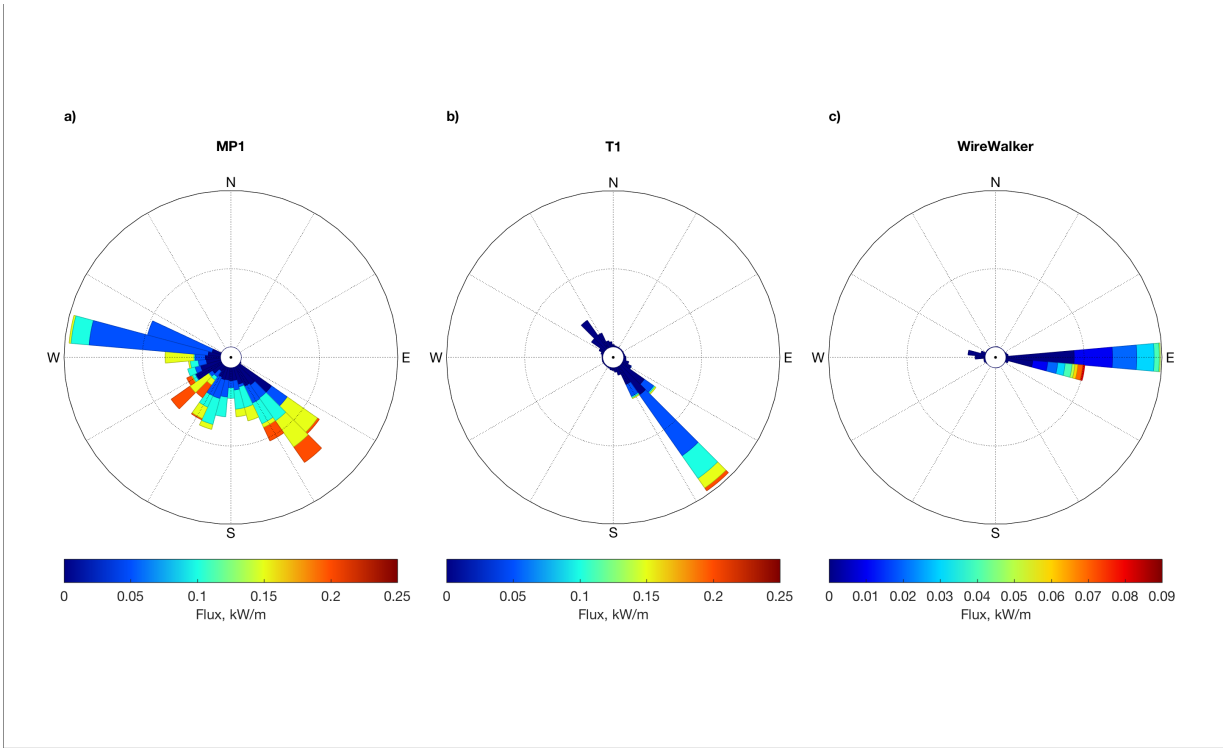

Figure 4.6: Magnitude and direction of depth-averaged semidiurnal energy flux observed at (a) WW, (b) T1, and (c) MP1.

and oscillate over a larger fraction of the water column moving up-canyon. Spectral analyses (described above) indicate that higher harmonic frequencies become increasingly energetic moving up-canyon as well.

As waveforms become increasingly steep moving up-canyon, the processes that drive mixing – and the vertical distribution of ε that results therefrom – also evolve. Spatial surveys made by *Hamann et al.* [2019] provided a snapshot view in which turbulent processes occurred primarily near the bottom on offshore lines where the up-canyon thalweg slope is subcritical, but moving up-canyon where the thalweg steepend turbulence occurred at mid-depths and in conjunction with high strain. Long time series confirm that this up-canyon evolution of turbulent processes occurs throughout the measurement period. Contours of $\varepsilon > 10^{-6.5}$ W/kg in Fig. 4.4 show enhanced turbulence occurs near the bottom at MP1, in phase with onshore (up-slope) flows and the time-averaged profile of dissipation is bottom-enhanced. At T1 and WW, time-averaged

dissipation is elevated throughout the water column, and periods of elevated dissipation occur just behind the leading edge of steep, nonlinear internal tides.

As in *Hamann et al.* [2019], probability distributions of shear, strain, and Richardson number computed at each mooring are computed for all data at MP1 and WW (where profile data permit estimates of dissipation via the Thorpe scale overturning method), for data indicating non-background levels of dissipation, and for data associated with $\varepsilon > 10^{-7}$ W/kg (Fig. 4.7). At MP1 and WW, values of enhanced dissipation are more likely to be associated with low Richardson numbers, up-canyon velocities, and high shear. At MP1, though, the distributions of shear and up-canyon velocity are much more skewed for overturns than at WW, and a skewness towards values of high strain is only apparent at WW. Like the time-averaged profiles of dissipation, the PDFs suggest that the processes that drive turbulence change from off- to on-shore. Moving towards the canyon head, strain becomes dominant driver of enhanced dissipation near the canyon head.

4.3.3 Temporal variability of the internal tide

Spring-Neap Cycles

Time series of semi-diurnal components of quantities computed at MP1, T1, and WW exhibit oscillations over sub-tidal frequencies ranging from several days to several weeks (Fig. 4.5). At MP1 in particular, fluctuations in E_{M_2} and F_{M_2} exhibit a clear cycle of about 2 weeks (Fig. 4.8c), as do bursts of enhanced dissipation near the bottom (Fig. 4.8d). At MP1, peaks in energy, which result primarily from increased *APE* occur with 14-day spacing and are correlated with maxima in the surface spring tide with nearly zero phase lag. Peaks in *HKE* are smaller, and lag behind *APE* peaks by 1 day.

At MP1, the first peak in energy flux aligns with the coincident peak in total energy, but the second peak in flux precedes that in energy by a few days. At T1, something similar occurs.

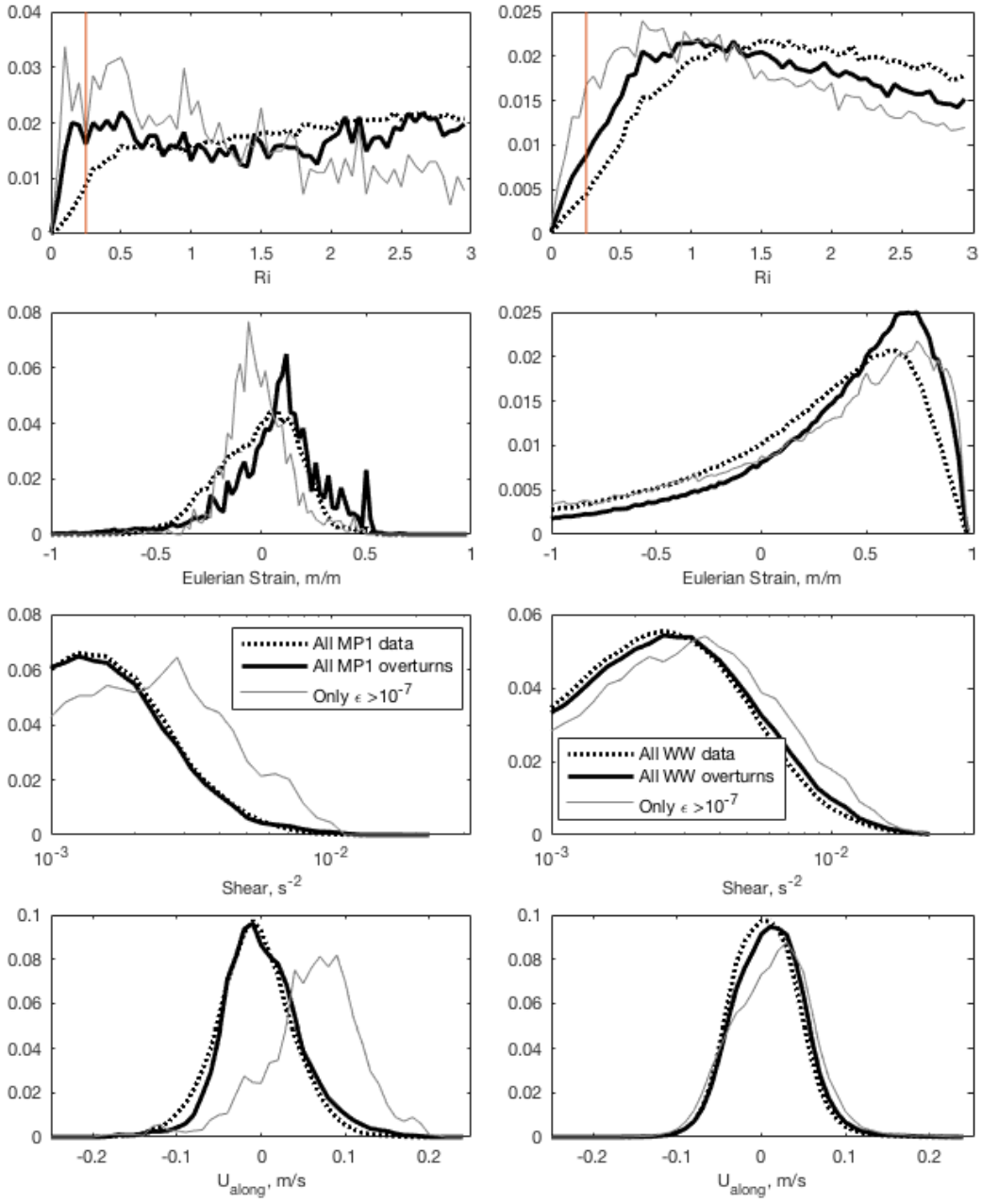

Figure 4.7: Probability distribution of (from top to bottom) 4-m Richardson number, Eulerian strain, 4-m shear magnitude, and along canyon velocity at (left) MP1 and (right) WW.

There, a spring neap cycle in energy is less clear: oscillations of 2-3 period are superimposed over a 2-week cycle. Peaks in energy, also dominated by fluctuations in *APE* are in phase with

energy peaks at MP1. Flux magnitude, however, shows no clear cycle on 14-day periods.

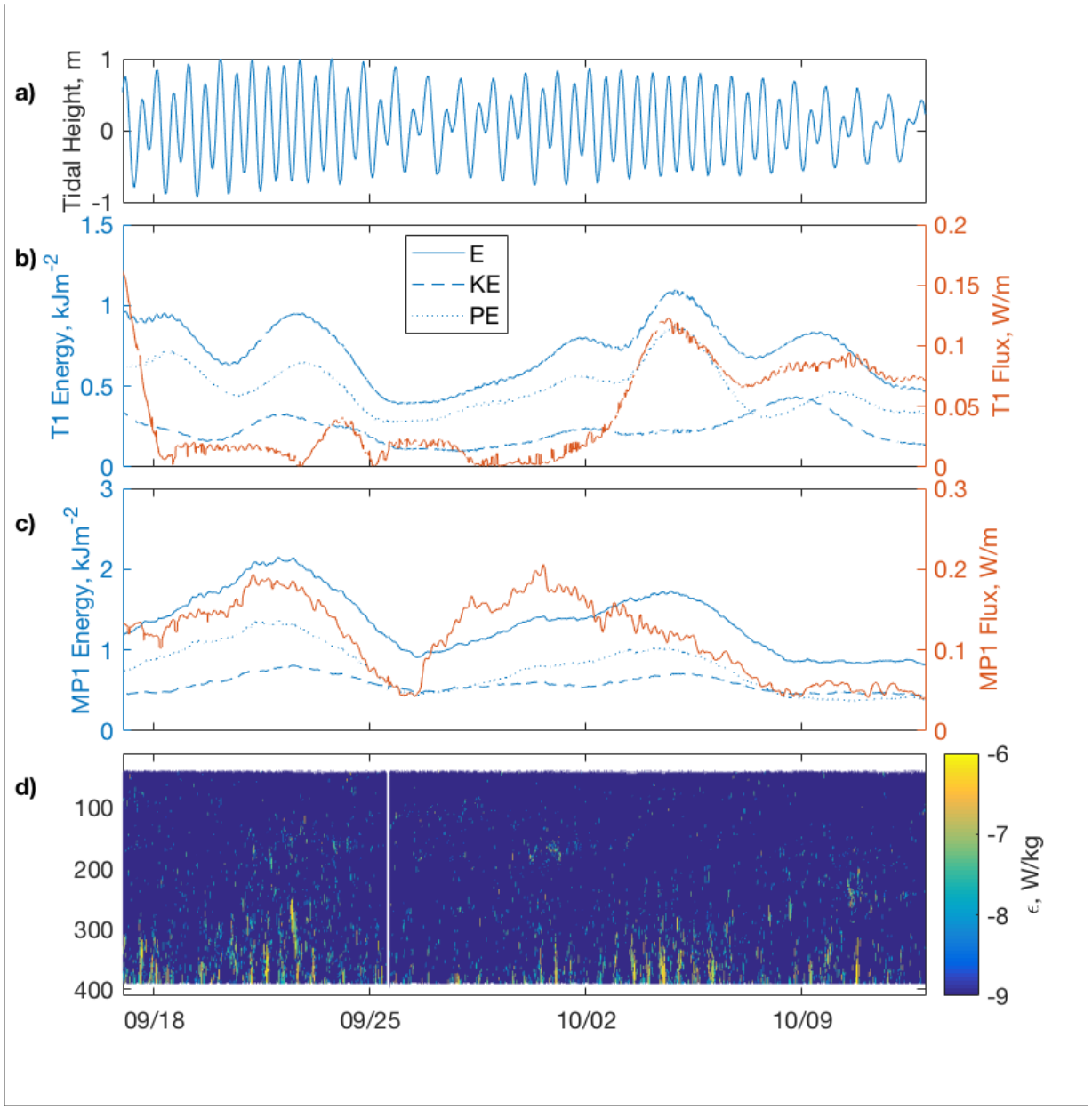

Figure 4.8: Time series capturing spring-neap cycles from (a) tidal height at the pier, depth-integrated semidiurnal energy, kinetic energy, potential energy, and energy flux magnitude at (b) T1 and (c) MP1, and (d) dissipation at MP1 observed over the 5 weeks for which data is available from MP1.

Summer vs Winter conditions

Because T1 and MP1 were recovered on December 15, 2016, an examination of the seasonal variability of internal waves in the LJCS is restricted to measurements from WW. We also use measurements from the nearby Del Mar mooring to bolster our understanding of basin-scale sub-tidal phenomena and to compare variability in the internal wave field in the canyon to that outside the walls of the canyon system.

During the winter, when winds strengthen and become directionally variable, rainfall and runoff events occur, and the angle of solar incidence provides less heat to the upper water column, the depth of the thermocline observed at WW shoals and stratification decreases over the water column (Fig. 4.1). During this time, integrated energy at WW also decreases from a 2-week average of about 1.6 kJ/m^2 to 1 kJ/m^2 and peaks in energy flux magnitude decrease from maxima in the fall of $>$100 kW/m to $<$25 kW/m. Steep, nonlinear wavefronts like those observed by *Alberty et al.* [2017] and that are observed throughout the fall (Fig. 4.9, right) continue to appear and their amplitudes are still up to and over half of the water column depth. Fig. 4.9 shows a comparison of the wavefronts observed at WW under two different stratification regimes.

In these less stratified conditions, neither isopycnal squeezing on the leading edge of incident waves nor isopycnal stretching trailing the leading edges are as strong as during the well stratified summer and autumn. Regardless, periods of enhanced dissipation at mid-depth coincide with periods of isopycnal straining. In the same fashion as for the comparison made between MP1 and WW moorings, figure 4.10 compares probability distributions of shear, strain, Richardson number, and along-canyon velocity computed for summer vs. winter conditions.

During the summer, elevated levels of dissipation tend towards higher strain, shear, and positive up-canyon velocities. For overturns and high values of ε, there is only a slight skew towards lower Richardson numbers. During winter, on the other hand, there is a pronounced skewness towards low Ri for overturns and high values of ε, but the distribution of shear does not change when considering only dissipative regions, indicating that decreased stratification, rather

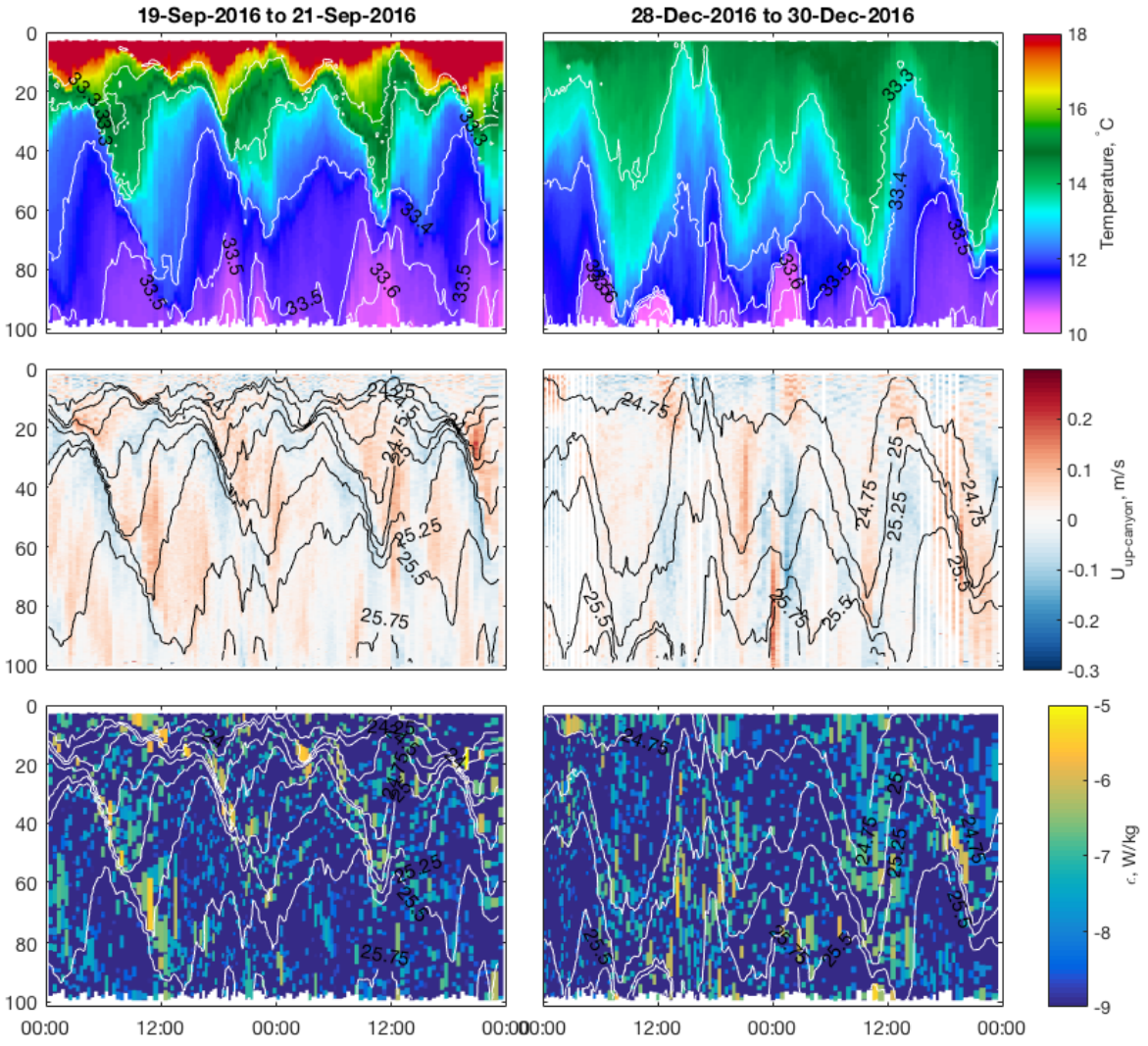

Figure 4.9: Two-day snapshots of (top) temperature, (middle) up-canyon velocity, and (bottom) ε_{OT} measured at WW during (left) summer vs. (right) winter stratification conditions.

than enhanced shear, sets the stage for instability.

Internal Tide Stationarity

Following the methods of *Nash et al.* [2012], harmonic fit skill scores are used to assess the predictive capability of harmonic fits for various time windows (Fig. 4.11). Skill scores

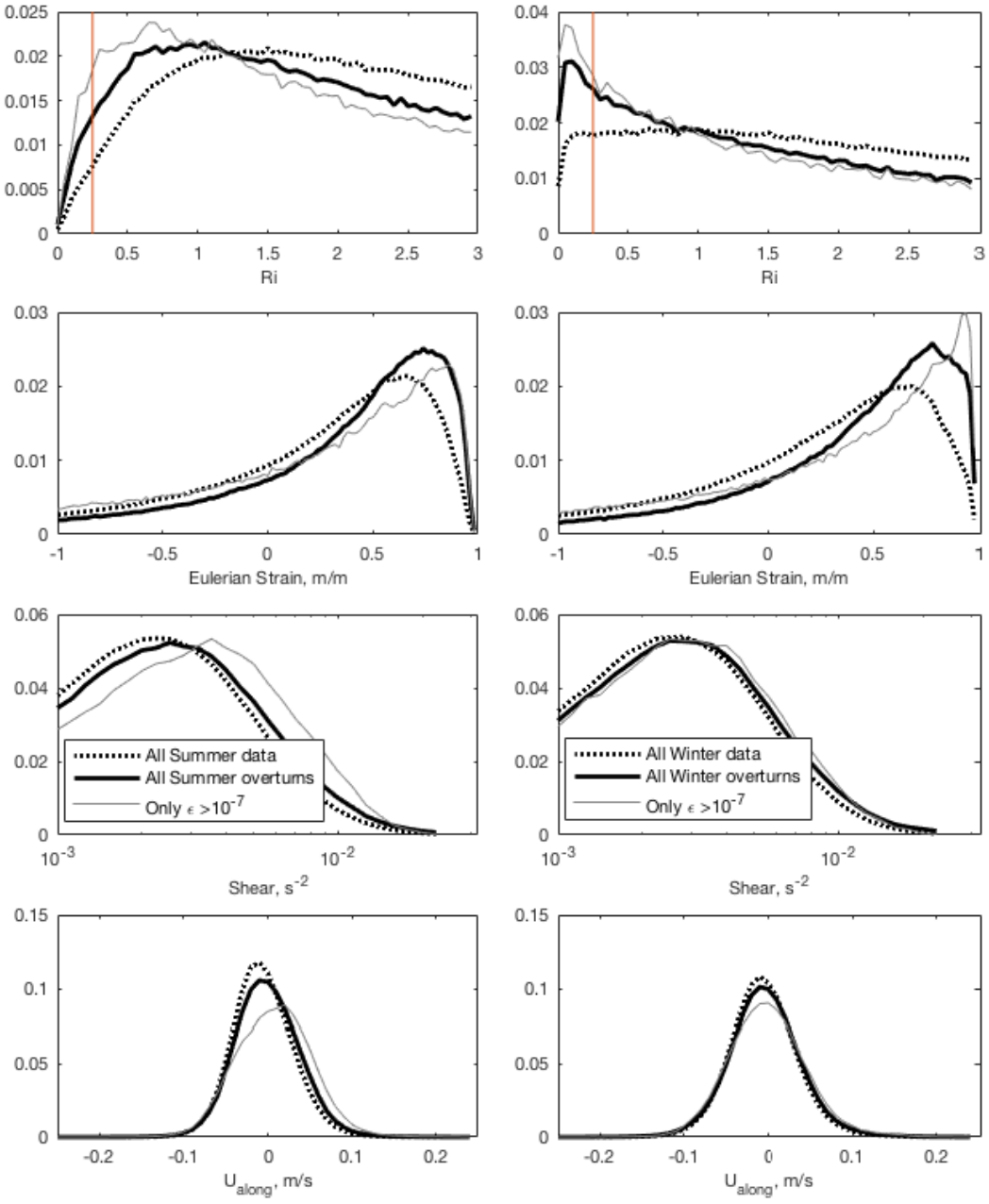

Figure 4.10: Probability distribution of (from top to bottom) 4-m Richardson number, Eulerian strain, 4-m shear magnitude, and along canyon velocity from WW for observations during the Summer (left) vs. Winter (right).

can be interpreted as an upper bound for the mismatch between data and fit that results from phase variability and de-tuning of the internal tide due to refraction between the measurement location and their generation source. As highlighted by *Nash et al.* [2012], the phase variability in observations of internal tides along the coastlines is generally quite significant due to the fact that internal tides can propagate away from local and remote sources and experience significant variability in the wave guide due to variable stratification and background currents. At WW, skill scores for harmonic fits using M_2, S_2, N_2, K_1, O_1, J_1, K_2 and L_2 tidal constituents (following *Nash et al.* [2012]) perform nearly as well as the most predictable mooring site they report, with an average of 50% of the variance in isopycnal displacement accounted for in the fit over the year (Fig. 4.11b; Table 4.2).

Table 4.2: Time- and depth- averaged skills scores for harmonic fits to displacement measured at Del Mar (DM) and WireWalker (WW) moorings using 12.5% overlapping fit windows of length T. Data from WW are subsampled to the same vertical and temporal resolution as data from DM.

T	**WW**	**DM**
3 d	96.0	92.3
5 d	90.3	73.3
1 wk	87.2	64.4
10 d	84.2	56.3
2 wk	81.4	50.0
3 wk	76.8	42.4
1 m	73.1	35.8
3 m	49.7	18.9

To determine whether the relatively high stationarity of the internal tide is specific to the canyon rather than a regional phenomenon, the same analysis is conducted on data collected from the Del Mar mooring. To ensure that differences in sampling do not affect the comparison, the WW data is subsampled to the same sparse depth coverage and longer time steps of measurements from DM. The comparison is shown in Fig. 4.11 and Table 4.2. As the fitting window T increases, skill scores decrease as expected, but at DM skill falls off much more than at WW.

Over 90-day fit windows, SS_{90} variation is 20-30% at both locations. From mid-October

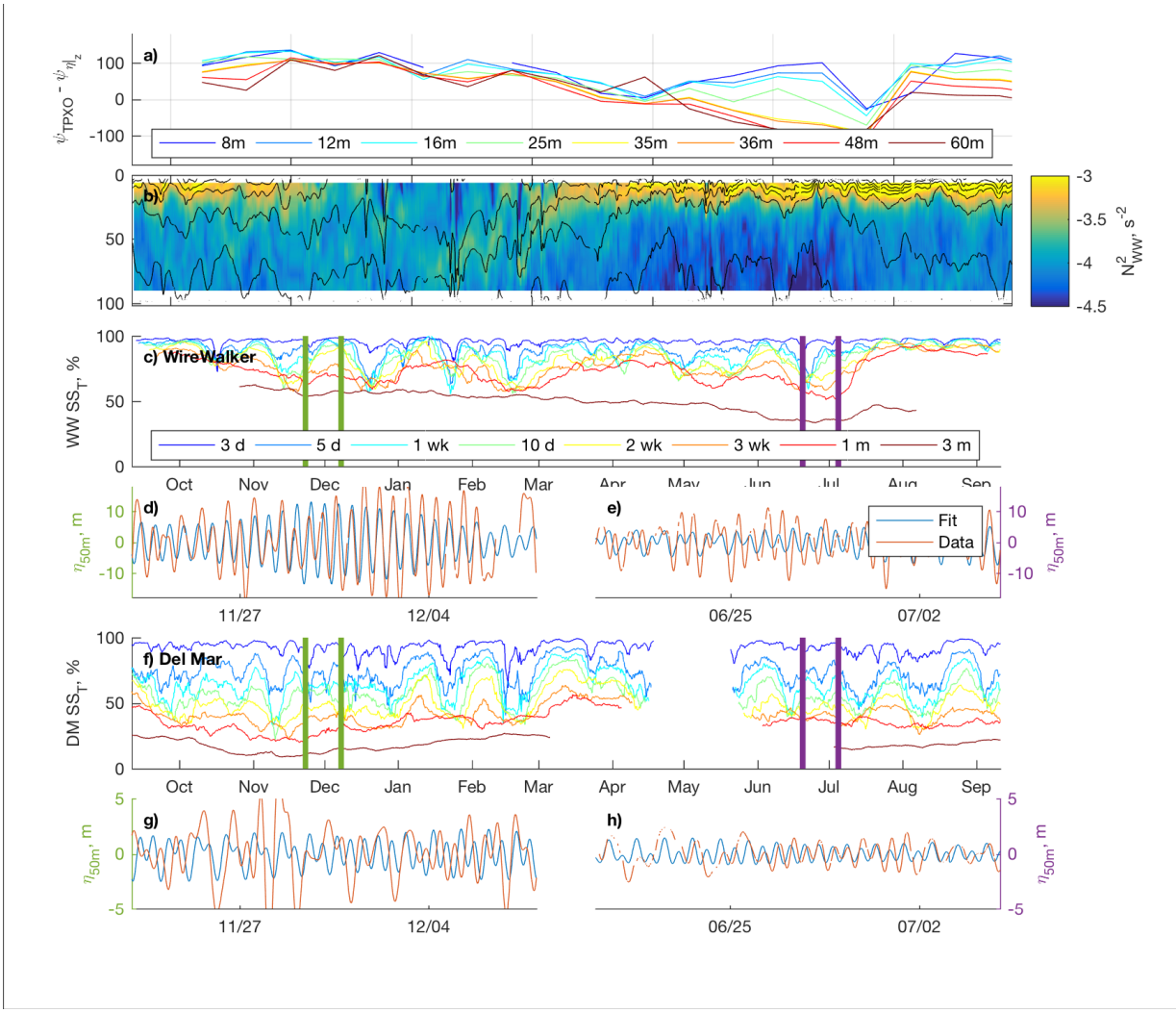

Figure 4.11: Harmonic analyses and skill scores for WW and DM. Time series (a) phase offset between TPXO surface tides and isopycnal displacement at several depths, (b) stratification averaged over a running 30-hour window and plotted with 7-day low-passed density contours (black lines), and SS_T computed from displacements at (c) WW and (f) DM for fit windows (T) ranging from 3 days to 3 months. Examples of the computed fit at 50m depth at both moorings for 2-week window during a period with higher (left; e,h) and lower (right; f,i) predictive skill; these periods are indicated by red and blue vertical lines in (c) and (f), respectively.

to January SS_{90} at DM is depressed. A notable decrease in 90-day stationarity occurs at WW between April and mid-July when upwelling is apparent in the region (Fig. 4.11b,c; not captured at DM due to mooring turnaround during that period). At the same time period, the phase offset between surface tidal height and isopycnal displacement changes (Fig. 4.11a). At the surface the

shift in phase offset is smallest (about 20°), but the difference increases steadily with depth so that at 60m depth the offset is shifted by almost 200° from the offset observed in Autumn. The large spread in phase offsets during this period indicates slower downward phase propagation that is visually apparent when comparing time series from the the different periods. Compared to non-upwelling periods, tidal oscillations of the shallow thermocline are relatively decoupled from deeper isopycnal displacements during this period.

At both moorings, skill scores become more variable as the length of the fit window decreases. When event-scale stratification shifts (such as heavy rain events in December, January, and February) occur, short term stationarity falls off at both mooring locations. In general, just as is the case with sub-tidal isopycnal displacements, shifts in stationarity are generally correlated between the two moorings.

In Fig, 4.11, panels (c) and (f) show an example of the data and fit for a 14-day fit window at 40m depth for WW and DM during a period with high stationarity at WW, and panels (d) and (g) show the same for a period of lower stationarity. For both time periods, there is remarkably little phase variation over the fit window at either location; the primary offsets between data and fit are not due to de-tuning of the semi-diurnal phase (as would be expected for waves coming primarily from remote and/or variable generation sites), but are the result of modulation in amplitude.

4.4 Discussion

4.4.1 Internal Tide Stationarity

Time series of measured and reconstructed displacement from harmonic analyses from WW show relatively little phase variation even for periods for which skill scores are reduced (Fig. 4.11d,e). Phase modulation at DM is greater (Fig. 4.11g,h), but still the majority of the mismatch between data and fit is due to variation in amplitude. These results suggest that the internal tide observed at both WW and DM comes from a nearby source.

Models of internal wave generation and propagation in the region offshore of San Diego by *Ponte and Cornuelle* [2013] find that the Coronado Escarpment (CE, approximately 24 km to the southwest of LJCS) is a region of strong conversion from barotropic to baroclinic internal tides and a likely source of internal tides observed in the region. The phase speed of a linear, mode 1 internal wave in the region (assuming an average depth of 500m and depth-averaged stratification $N = 10^{-2}s^{-1}$) is about 1.3 m/s so that the travel time between the CE and WW is 5.2 hours and between CE and DM is 9.4 hours–less than 1 semidiurnal period. Under these conditions, internal motions WW would lead those at CE by a phase shift of 152°, which is close to the observed phase offset between surface tides and internal isopycnal displacement at WW (Fig. 4.11a).

As upwelling conditions arise, surface stratification increases but stratification in the lower half of the water column decreases from $N = 10^{-2}s^{-1}$ to $N = 5.6 \times 10^{-3}s^{-1}$. Assuming that in deeper water these values are consistent and decrease the depth-averaged value of N^2 offshore accordingly during upwelling, the phase speed of a mode 1 internal wave in the region should decrease to about 0.8 m/s with travel times to WW and DM increasing accordingly to 9.3 and 16.8 hours, respectively. Internal motions at WW would shift to to a phase lag of 90° behind surface displacements at CE – which is again consistent the observed phase offset between surface forcing and isopycnal displacement at WW during this period and reinforces the likelihood that

CE is the primary generation region for the internal tides observed at WW and DM.

The reduction in SS_{90} and the observation that phase offsets between surface forcing and isopycnal displacement have a wider spread over the water column between May and August is most likely due to the stratification structure associated with upwelling conditions. During this period, surface stratification is strengthened above time-averaged values while deep stratification is reduced. Reduced stratification at depth means that less energy is required to cause large isopycnal displacements, and the effect of energy input from even small non-stationarity waves would be visible in amplitude offsets as is the case in Fig. 4.11e. The difference in internal wave phase speeds between the deep and shallow stratification regimes would be significant so that the apparent downward phase propagation would be more pronounced, as is observed.

That the stationarity of a locally generated internal tide is so different between locations only 22km apart is somewhat surprising, especially given the nonlinear nature of the internal tide observed at WW. Station DM is about twice as far from Coronado escarpment, which would allow twice as much time for background currents and stratification changes to alter the phasing of arrival times at DM. If we assume that alongshore barotropic currents of a magnitude similar to those observed at DM ($\tilde{0}.2$ m/s) act in the direction of propagation, they could alter arrival times at WW and DM by ± 3 hr and ± 6 hr, respectively, and so phase variation due to shifting alongshore currents could explain part of the observed modulation. However, in order for the phase modulation to appear *differently* at the two locations, currents would need to shift on timescales similar to the change in travel time between the mooring locations, and they do so infrequently.

Another possibility is that canyon geometry "selects" for a smaller subset of incident wave directions – where DM is on the open shelf and exposed to waves from all directions, waves at WW are first trapped and focused in the up-canyon direction; that is, WW and DM are highly directional and omnidirectional wave antennae, respectively.. Waves of a different (perhaps northerly) origin that are oblique to the canyon mouth may not propagate up-canyon where their

contribution would scramble the phase. Although results from *Hamann et al.* [2019] suggest that conversion from barotropic to baroclinic motions within the canyon is not significant, there is certainly more near-critical bathymetry in the canyon region than at DM that would lead to local conversion and internal tide signal phase locked to the barotropic forcing. The phase offset between surface tides and isopycnal displacements, though, is not consistent with generation at a nearby location being the primary internal tide source at WW. Further investigation to determine how bathymetry, stratification, IT sources, and regional conditions contribute to the stationarity observed at WW is warranted.

The implications of such stationarity and potential predictability of internal tides at this nearshore location are numerous. Combined with knowledge of the dynamics and mixing processes that occur in concert with internal tides, it is possible that the strength and location of mixing is relatively predictable as well. If so, properties at the sea surface (temperature and salinity)le might be predictab. Because the local relationship between temperature and nitrate is strong [*Li et al.*, 2012], a reasonable prediction of nutrient fluxes into the euphotic zone might be assessed, and local phytoplankton blooms and red tide conditions may be predicted with more advance notice. Stationary tides and predictable isopycnal motions would also contribute to more predictable sound speed changes and could simplify the acoustic environment near the canyon both for both humans seeking to better underwater communication and sensing capabilities and for local marine creatures that rely on acoustics for navigation.

4.4.2 Spring Neap Variability

Variability in semidiurnal energy and flux at 14-day periods that is nearly in phase with the spring-neap cycle of the surface tide at MP1 also supports the notion that the internal tides in LJCS are generated nearby. With short distances to travel from the generation site to the canyon, the internal tide impinging on LJCS is mostly stationary and regular; compounded with the canyon's geometry that traps and focuses internal tides, the signal to noise ratio of semidiurnal

tides to contributions from low frequency current shifts and other wave frequencies is much higher than that on the adjacent shelf, and so the beating of the solar and lunar semi-diurnal tides becomes a discernible and important signal in the time series collected within the canyon walls.

Not only is the signal apparent in physical quantities within the canyon–depth-integrated chlorophyll fluorescence also exhibits a clear spring neap cycle that lags behind maxima in semidiurnal energy by 2-3 days at times throughout the year (Fig. 4.12). Although spring-neap cycles do not always dominate the chlorophyll signal (a seasonal cycle is apparent and response to strong rainfall events mixed layer deepening are also clear), the regularity of internal tides, their associated turbulence, and the nutrients that turbulence could deliver to the system by mixing up deeper waters are likely key for the productivity of this kind of system. These regular and somewhat predictable physics may set the foundation for productivity and biological abundance that may make the LJCS–and perhaps other canyons with similar physics–a particularly good location to foster habitat rehabilitation and species recovery. Although the details of the connection between the physics and the biological response has not been documented in the LJCS, there are examples such as in Cabo Pulmo, Mexico where protection of water adjacent to canyon systems has led to massive and rapid species recovery [*Álvarez-Filip and Reyes-Bonilla*, 2006; *Aburto-Oropeza et al.*, 2011].

In longer time series at T1 and WW variability at spring-neap timescales is not always clear–especially in energy flux, as highlighted in Fig. 4.8b. That spring-neap cycles in energy and energy flux are not always clear supports the notion that the majority of IT energy in LJC comes from a relatively local generation region, but (as addressed above) is not primarily generated from tidal conversion over canyon topography. Though they are generated nearby, low mode internal waves of offshore origin are the primary source of energy to the IW field and its associated turbulence in the LJCS.

Since observed energy fluxes are a combination of both the incident and reflected wave-forms, when total reflection occurs net fluxes can approach zero. Energy flux magnitude can

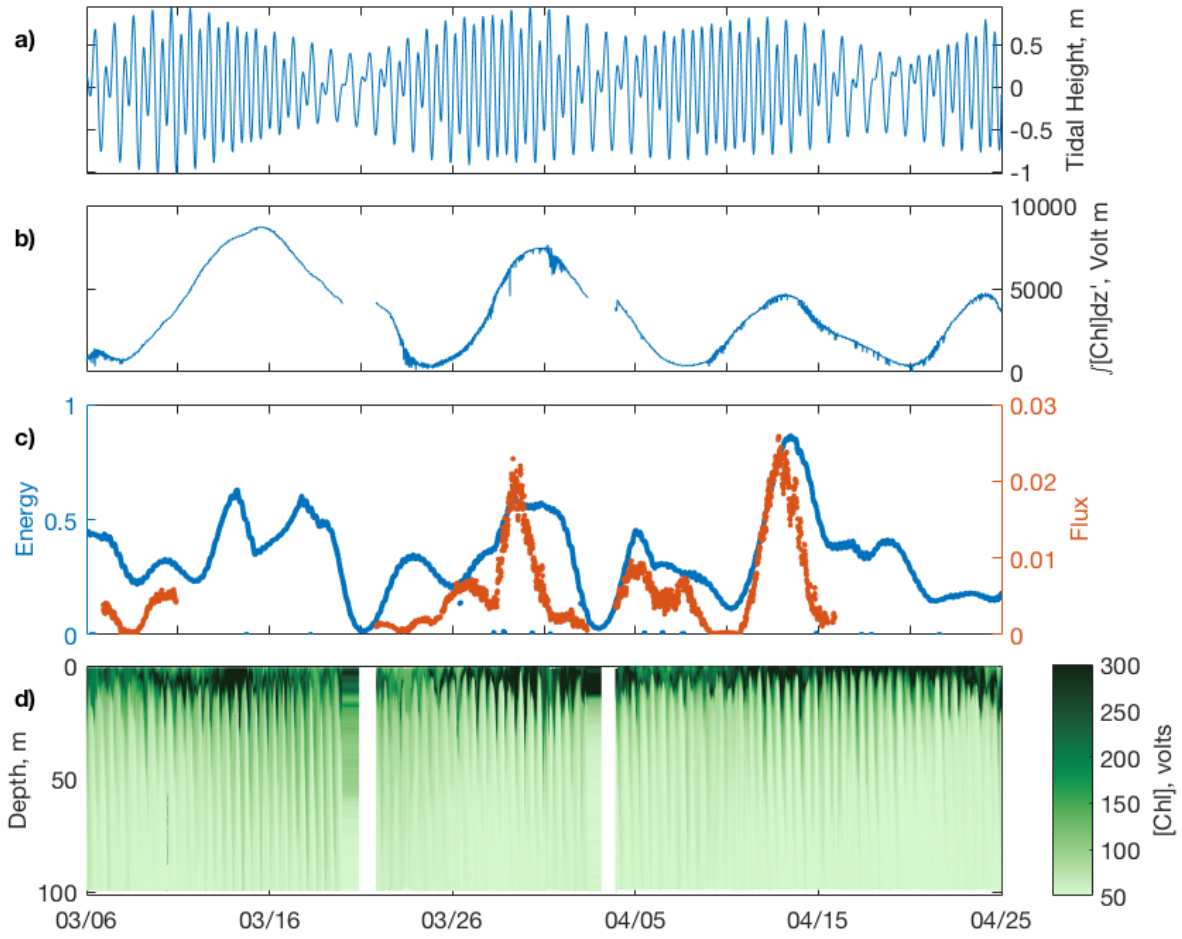

Figure 4.12: Time series of (a) tidal height at the Scripps pier and (b) depth-integrated chlorophyll fluorescence after removing seasonal cycle, (c) depth-integrated energy and energy flux magnitude, and (d) raw chlorophyll fluorescence data.

therefore be affected if the reflectivity of the tide changes. As reflectivity is set by changes in near-bottom stratification, sub-tidal shifts associated with basin-scale upwelling and downwelling of isopycnals could affect whether and from which location along the canyon axis a wave should reflect at a given time.

The effects of changing location of the reflection point in the canyon could cascade into energy and flux signals in a complicated manner. First, the distance over which the reflected wave travels from the node to the measurement location correlates to the amount of energy that

is lost to dissipative processes along the way and would affect the observed energy and energy partitioning (as pointed out by the theoretical model of partial reflection laid out by *Waterhouse et al.* [2017]). If the primary reflection point moved to a location offshore of the mooring, the flux observed at the mooring would consist of only the forward-progressing component of the total energy flux. The three-dimensionality of the system likely also factors in – reflection from a point further up-canyon where sidewalls are closer together may enhance energy convergence and enhance dissipation at the node so that the energy flux of the reflected wave is reduced.

In addition to altering reflection within the canyon, basin-scale shifts in stratification could alter both the strength of the conversion at the generation site and the waveguide through which wave energy travels. A deepening of the thermocline or strengthening of near-bottom stratification could cause waves to reflect off of topographic features offshore of the canyon that previously permitted forward progression.

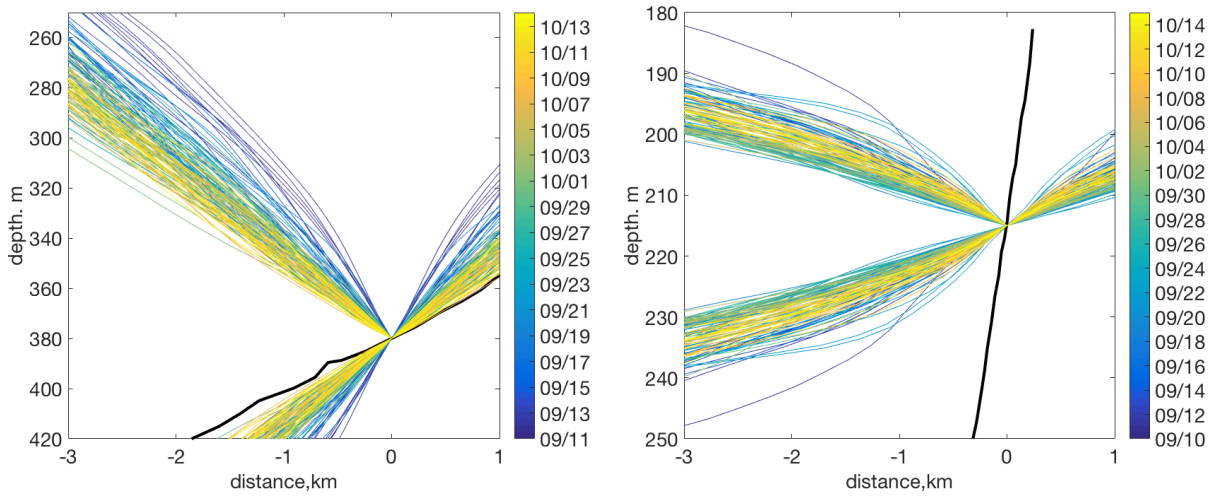

Figure 4.13: Folllowing *Zhao et al.* [2012]: ray paths (colored lines) for semidiurnal waves in the vicinity of (left) MP1 and (right) T1 moorings. Rays are colored according to the date. Thick black lines indicate the slope along the canyon axis at each location.

During periods where spring neap variability is clear, our measurements suggest a coupling between the forcing and feedbacks. In the vicinity of near-critical slopes, an enhancement of near-bottom mixing is in phase with the surface spring-neap forcing. This enhanced dissipation could

erode near-bottom stratification such that the slope of the ray paths of semi-diurnal internal waves shifts from being near-critical to being forward-progressing. During neap tide, re-stratification near the bottom brings the ray paths back to a near-critical slope. This is demonstrated in the ray paths at MP1 shown in Fig. 4.13. Further up-canyon at T1, ray paths of the semi-diurnal internal tide do shift over spring-neap timescales, but because the slope of the topography is so steep, the change is not enough to bring them to near-critical and T1 remains reflective to the M_2 internal tide throughout the measurement period, consistent with results from examining energy ratios that suggest the internal tide is always partially standing at that location. Many canyons exhibit a similar steepening in a the few kilometers close to the canyon head such that the dynamics and mid-depth mixing processes associated with internal tide reflection could occur consistently throughout the year in a multitude of shelf-incising canyons. Persistent mid-depth mixing associated with canyon reflection could play a key role in setting the physical, chemical, and biological properties of coastal ocean environments.

4.5 Summary

Long time series of tidally resolving measurements in the La Jolla Canyon allow an assessment of the temporal variability of internal wave dynamics and associated turbulent processes in the La Jolla Canyon System. Building on and confirming results from spatial surveys made by *Hamann et al.* [2019], we find:

- Semidiurnal internal tides always dominate velocity signals within the LJCS
- Continuum spectral levels are not significantly elevated above GM76.
- Internal tidal motions become increasingly rectilinear moving up-canyon.
- Mode 1 semidiurnal internal tides are partly standing in LJCS throughout the observed time period, and energy ratios are consistent with the canyon head being a reflection node.

- Further offshore, dissipation is primarily enhanced near the bottom, and is correlated with elevated shear and up-canyon velocities. Inshore, dissipation occurs in concert with high strain events at mid-depth, and time-averaged dissipation is elevated throughout the water column

- During the winter months, local stratification decreases. Although large-amplitude tidal oscillations persist at the canyon head and elevated dissipation is correlated with high strain, elevated dissipation is also correlated with low Richardson numbers that occur due to decreased stratification.

- Depth-integrated energy, flux, stratification, dissipation, and chlorophyll fluorescence exhibit spring-neap variability at times throughout the year.

- Compared with typical results from coastal ocean moorings, internal tides in the LJCS are quite predictable and exhibit very little phase variability over time suggesting that the majority of internal tide energy focused into the La Jolla canyon is generated at an offshore location nearby.

4.6 Acknowledgements

Chapter 4, in part, is currently being prepared for submission for publication of the material. Hamann, Madeleine M.; Alford, Matthew H.; Lucas, Andrew J. The dissertation/thesis author was the primary investigator and author of this material.

This work was supported by the NSF Graduate Research Fellowship Program, and ship time for this experiment was provided by the UC Ship Funds program. We would especially like to thank Gunnar Voet, Paul Chua, Arnaud LeBoyer, Jonathan Ladner, and Tyler Hughen from the Multiscale Ocean Dynamics (MOD) group at UC San Diego for their time and expertise

in designing, deploying, and recovering moorings. The captain and crew of the R/V *Gordon Sproul* and R/V *Sally Ride* were instrumental in the success of this field campaign. We would also like to thank Janet Sprintall, Jonathan Nash, Eric Terrill, Geno Pawlak, and Falk Feddersen for generously loaning equipment for our efforts. Shipboard data for this experiment can be found at DOI:10.7284/906929 and DOI:10.7284/907217. Please contact the authors for access to moored datasets.

Appendix A

Estimates of Dissipation of TKE

A.1 Methods

Three different techniques were used to compute ε from the various datasets collected during this experiment. They are explained in detail in what follows and then compared.

A.1.1 ε from shear variance

The most direct method available to estimate ε is to measure high-frequency velocity fluctuations using airfoil shear probes. The MMP, with its slower fall rate and loosely-tethered configuration, is equipped with such probes and is able to resolve turbulent velocity fluctuations over the full spectrum of shear variance [*Oakey*, 1982; *Wesson and Gregg*, 1994]. Integrating beneath these fully resolved spectra gives a value of ε directly. We treat these direct measurements of ε as the "gold standard" to which we can compare estimates made using other techniques from concurrent measurements on MMP.

A.1.2 ε from χ

In the formulation of scalar gradient spectra, χ and ε are treated as independent parameters so that determination of χ from data requires measurements from fully resolved spectra. Although the fall rate of MMP allows for such resolution, measurements from the FP07 rapid thermistor on the SWIMS Chiometer do not. The package moves vertically at a rate of 1-2 m s^{-1} so that at moderate levels of ε only a fraction of wavenumbers in the diffusive subrange are captured and the highest wavenumbers are attenuated due to sensor response (see Fig. A1 of *Alford and Pinkel* [2000a] for example).

Instead of integrating under the observed temperature gradient spectrum, then, we here use an iterative approach similar to that laid out by *Moum and Nash* [2009] to determine χ by fitting a canonical form of the temperature gradient spectrum within a range of wavenumbers in the inertial-convective subrange (Note: while *Moum and Nash* [2009] use the *Kraichnan* [1968] canonical form, we use that proposed by *Batchelor* [1959]). Because the fitting of the canonical spectrum leaves both ε and χ undetermined, the system of equations is closed by equating the eddy diffusivity for heat (κ_T) prescribed by *Osborn and Cox* [1972] and the eddy diffusivity of density (κ_ρ) proposed by *Osborn* [1980] and prescribing a constant mixing efficiency (Γ) of 0.2. This leaves us, ultimately, with an equation for the dissipation of turbulent kinetic energy from χ (ε_χ) given by:

$$\varepsilon_\chi = \frac{N^2 \chi}{2\Gamma \langle dT/dz \rangle^2} \tag{A.1}$$

where dT/dz is a mean vertical temperature gradient in the background state.

A.1.3 ε from overturns

In using χ to estimate ε we operate on the assumption that high temperature variance is due to turbulence. However, in regions where density is more strongly influenced by salinity—such as in intrusions—this assumption does not hold and the aforementioned method is invalid.

Wherever intrusions are observed from SWIMS (which does not carry shear probes), then, an alternative method is required, and so in these regions we estimate dissipation from observed density overturns (ε_{OT}) following the Thorpe scale method described by *Thorpe* [1977]; *Dillon* [1982] and *Gargett and Garner* [2008]. Because most dissipation tends to coincide with large regions of statically unstable fluid, values of ε_{OT} have been shown to agree well with values of ε from shear variance in a time-averaged sense [*Ferron et al.*, 1998; *Alford et al.*, 2006].

A.2 Method comparison

To justify using the latter two methods for determining and using ε_{OT} and ε_{χ} in our energy budgets, we apply the methods to measurements of density and microscale temperature taken from MMP and compare the resulting ε_{OT} and ε_{χ} to the concurrent estimates of ε. The comparison is laid out in Fig A.1. In regions where the computed χ is high while ε is low (on the boundaries of intrusions, for example), the resulting ε_{χ} is artificially high (Fig. A.1a). However, these regions are relatively rare (especially in shallower water where this method was used) such that relationship between ε and ε_{χ} is nearly 1:1 in a bin-averaged view (Fig. A.1b). Estimates from Thorpe scales (ε_{OT}) agree with ε to within a factor of 2 in a time averaged sense, but provide estimates only in areas for which an overturn $>$1m is detected. Everywhere else, ε_{OT} is set to a default value of 10^{-11}. This can be seen clearly in Fig. A.1c, where even for high values of ε, ε_{OT} is set to the minimum value. Because of this, ε_{OT} is biased low in some profiles.

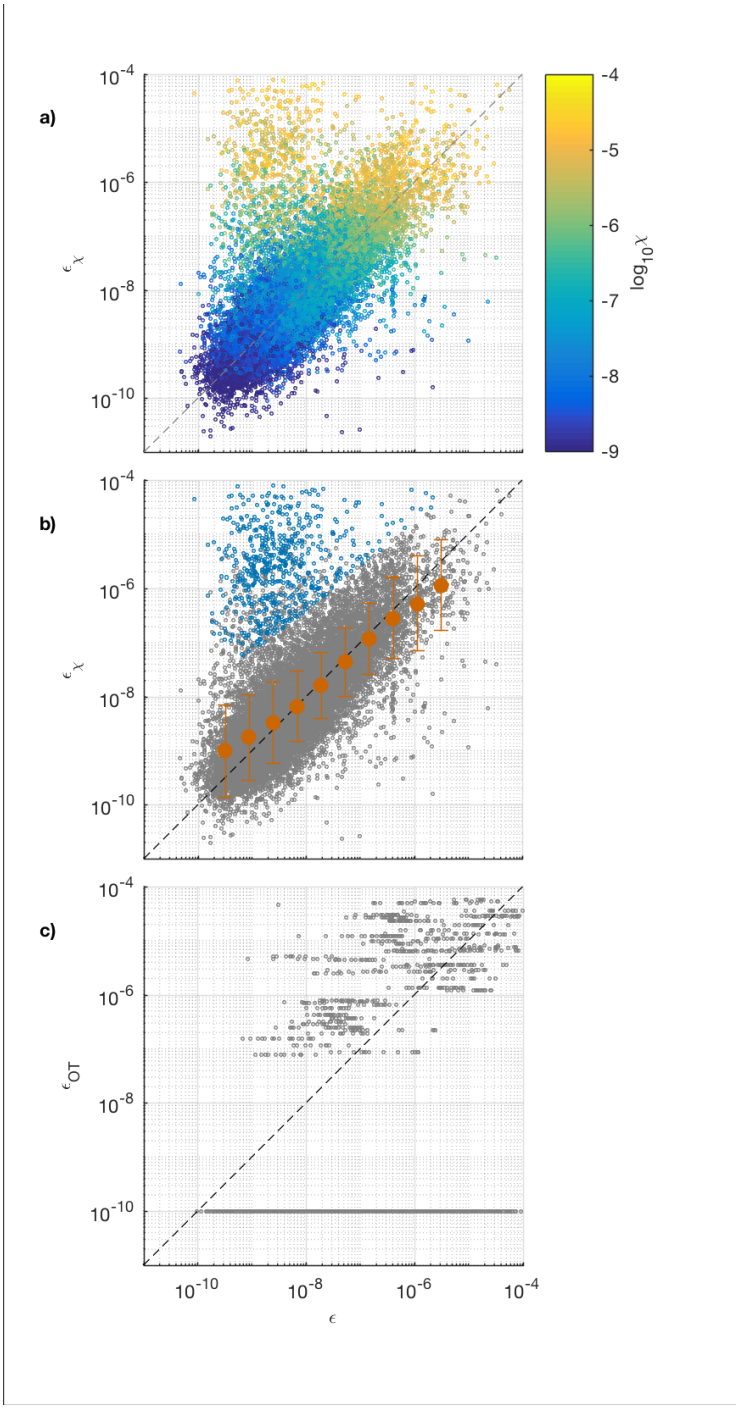

Figure A.1: Comparison of ε computed from shear probes vs. ε_χ estimated from microscale temperature gradients. In panel (a) the relationship is colored by the computed value of χ while in panel (b) shows a bin-averaged relationship (orange dots) with error bars indicating the standard deviation. Dashed lines indicated the ideal 1:1 relationship between the two variables.

Appendix B

Thorpe scale vs microstructure validation

In February 2017, a short experiment (PLUMEX) was conducted in the vicinity of the LJCS. During this experiment, profiles were made over the axis of the LJC over the course of 10.5 hours using the Modular Microstructure Profiler (MMP). MMP is a loosely tethered body that measures temperature, conductivity, pressure, oxygen, and micro- shear and temperature as it free-falls vertically at 0.6 m s^{-1} such that its shear probes are able to resolve turbulent velocity fluctuations over the full spectrum of shear variance [*Oakey*, 1982; *Wesson and Gregg*, 1994]. By integrating under these well-resolved spectra, an estimate for the value of ε is obtained directly. Values obtained from this direct method can then be compared to those obtained by other methods. During LaJIT2, no usable microstructure measurements were recovered from SWIMS, and we therefore estimate dissipation (ε_{OT}) from regions of statically unstable fluid (overturns) following the Thorpe scale method described by *Thorpe* [1977]; *Dillon* [1982] and *Gargett and Garner* [2008].

Because turbulence tends to coincide with overturns, values of ε_{OT} tend to agree well with values of ε from shear variance in a time-averaged sense [*Ferron et al.*, 1998; *Alford et al.*, 2006]. To justify using ε_{OT} in this particular region where stratification is relatively strong, we compare ε_{OT} to the concurrent estimates of ε made from MMP. This comparison is laid out in

time-averaged profiles of ε_{OT} and ε in Fig. B.1 and point-by-point in Fig. B.2. In a bin-averaged sense, ε_{OT} is biased slightly high (particularly for lower values of ε). However, in a time-averaged sense there is good agreement in the vertical profile of ε and ε_{OT}, and the average value computed for the two methods agrees well within a factor of 2 ($\langle\varepsilon_{OT}\rangle = 1.05 \times 10^{-8}$; $\langle\varepsilon\rangle = 1.10 \times 10^{-8}$).

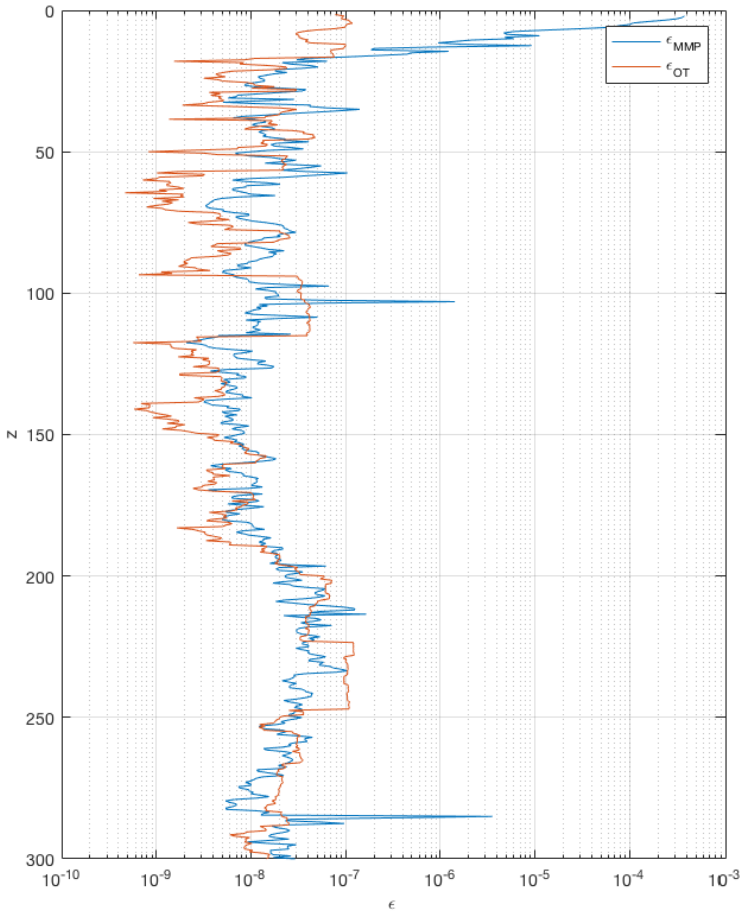

Figure B.1: Example profile to compare ε measured from MMP (ε_{MMP}, blue line) and computed from overturns (ε_{OT}, red line)

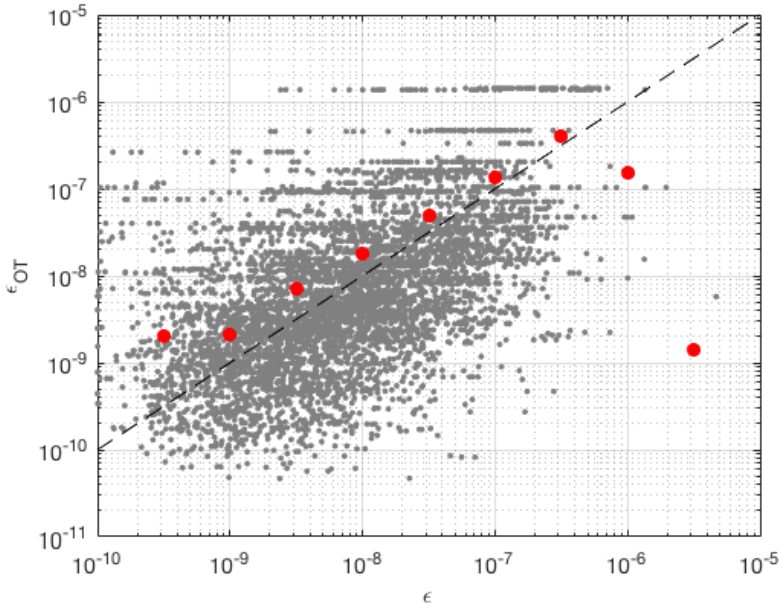

Figure B.2: Scatterplot of ε vs. ε_{OT} for all overturns detected below 30m depth. Red squares indicate binned and averaged values.

Bibliography

Aburto-Oropeza, O., B. Erisman, G. R. Galland, I. Mascareñas-Osorio, E. Sala, and E. Ezcurra, Large recovery of fish biomass in a no-take marine reserve, *PLoS One*, *6*(8), e23,601, 2011.

Alberty, M. S., S. Billheimer, M. M. Hamann, C. Y. Ou, V. Tamsitt, A. J. Lucas, and M. H. Alford, A reflecting, steepening, and breaking internal tide in a submarine canyon, *Journal of Geophysical Research: Oceans*, *122*, 6872–6882, doi:10.1002/2016JC012583, 2017.

Alford, M., and R. Pinkel, Patterns of turbulent and double diffusive phenomena: Observations from a rapid profiling conductivity probe, *J. Phys. Oceanogr.*, *30*, 833–854, 2000a.

Alford, M. H., and P. MacCready, Flow and mixing in Juan de Fuca Canyon, Washington, *Geophys. Res. Lett.*, *41*, 1–8, doi:10.1002/2013GL058967, 2014.

Alford, M. H., and R. Pinkel, Observations of overturning in the thermocline: The context of ocean mixing, *J. Phys. Oceanogr.*, *30*, 805–832, 2000b.

Alford, M. H., and Z. Zhao, Global patterns of low-mode internal-wave propagation, Part I: Energy and energy flux, *J. Phys. Oceanogr.*, *37*(7), 1829–1848, 2007a.

Alford, M. H., and Z. Zhao, Global patterns of low-mode internal-wave propagation, Part II: Group velocity, *J. Phys. Oceanogr.*, *37*(7), 1849–1858, 2007b.

Alford, M. H., M. C. Gregg, and M. A. Merrifield, Structure, propagation and mixing of energetic baroclinic tides in Mamala Bay, Oahu, Hawaii, *J. Phys. Oceanogr.*, *36*(6), 997–1018, 2006.

Alford, M. H., J. B. Mickett, S. Zhang, Z. Zhao, and J. Newton, Internal waves on the Washington continental shelf, *Oceanography*, *25*(2), 66–79, 2012.

Alford, M. H., et al., Energy flux and dissipation in Luzon Strait: Two tales of two ridges, *J. Phys. Oceanogr.*, *41*(11), 2211–2222, 2011.

Alford, M. H., et al., The formation and fate of internal waves in the South China Sea, *Nature*, *521*, 65–73, 2015.

Allen, S., and X. Durrieu de Madron, A review of the role of submarine canyons in deep-ocean exchange with the shelf, *Ocean Science Discussions*, *6*(2), 1369–1406, 2009.

Allen, S., and B. Hickey, Dynamics of advection-driven upwelling over a shelf break submarine canyon, *Journal of Geophysical Research*, *115*(C8), C08,018, 2010.

Allen, S. E., C. Vindeirinho, R. E. Thomson, M. G. Foreman, and D. L. Mackas, Physical and biological processes over a submarine canyon during an upwelling event, *Canadian Journal of Fisheries and Aquatic Sciences*, *58*(4), 671–684, doi:10.1139/f01-008, 2001.

Althaus, A., E. Kunze, and T. Sanford, Internal tide radiation from Mendocino Escarpment, *J. Phys. Oceanogr.*, *33*(7), 1510–1527, 2003.

Álvarez-Filip, L., and H. Reyes-Bonilla, Comparison of community structure and functional diversity of fishes at cabo pulmo coral reef, western mexico between 1987 and 2003, in *Proceedings of 10th International Coral Reef Symposium*, vol. 2, pp. 16–225, Okinawa, 2006.

Apel, J., L. Ostrovsky, Y. Stepanyants, and J. Lynch, Internal solitons in the ocean, *Tech. rep.*, Woods Hole Oceanog. Inst. Tech. Rept., WHOI-2006-04.

Apel, J. R., J. R. Holbrook, A. K. Liu, and J. J. Tsai, The Sulu Sea internal soliton experiment, *J. Phys. Oceanogr.*, *15*, 1625–1651, 1985.

Aslam, T., R. A. Hall, and S. R. Dye, Internal tides in a dendritic submarine canyon, *Progress in Oceanography*, doi:10.1016/j.pocean.2017.10.005, 2017.

Avicola, G. S., J. N. Moum, A. Perlin, and M. D. Levine, Enhanced turbulence due to the superposition of internal gravity waves and a coastal upwelling jet, *J. Geophys. Res.*, *112*(C6), doi:10.1029/2006JC003831, 2007.

Batchelor, G. K., Small-scale variation of convected quantitites like temperature in turbulent fluid, *J. Fluid Mech.*, *5*, 113–139, 1959.

Boegman, L., and A. Dorostkar, Three-dimensional simulation of nliw generation, propagation and breaking in cayuga lake, in *7th Int. Symp. on Stratified Flows, Rome, Italy*, pp. 22–26, Citeseer, 2011.

Bogucki, D., T. Dickey, and L. Redekopp, Sediment resuspension and mixing by resonantly generated internal solitary waves, *J. Phys. Oceanogr.*, *27*(7), 1181–1196, 1997.

Bond, N. A., M. F. Cronin, H. Freeland, and N. Mantua, Causes and impacts of the 2014 warm anomaly in the ne pacific, *Geophysical Research Letters*, *42*(9), 3414–3420, 2015.

Bosley, K. L., J. W. Lavelle, R. D. Brodeur, W. W. Wakefield, R. L. Emmett, E. T. Baker, and K. M. Rehmke, Biological and physical processes in and around astoria submarine canyon, oregon, usa, *Journal of Marine Systems*, *50*(1), 21–37, 2004.

Butman, B., P. Alexander, A. Scotti, R. Beardsley, and S. Anderson, Large internal waves in massachusetts bay transport sediments offshore, *Continental shelf research*, *26*(17-18), 2029–2049, 2006.

Cairns, J. L., and G. O. Williams, Internal wave observations from a midwater float, 2, *J. Geophys. Res.*, *81*, 1943–1950, 1976.

Carmack, E. C., and E. A. Kulikov, Wind-forced upwelling and internal kelvin wave generation in mackenzie canyon, beaufort sea, *Journal of Geophysical Research: Oceans*, *103*(C9), 18,447–18,458, doi:10.1029/98jc00113, 1998.

Carter, G. S., and M. C. Gregg, Intense, variable mixing near the head of Monterey Submarine Canyon, *J. Phys. Oceanogr.*, *32*, 3145–3165, 2002.

Chang, M., R. Lien, Y. Yang, and T. Tang, Nonlinear internal wave properties estimated with moored adcp measurements, *Journal of Atmospheric and Oceanic Technology*, *28*(6), 802–815, 2011.

Charney, J. G., and G. R. Flierl, Oceanic analogues of large-scale atmospheric motions, 1981.

Chiu, C.-S., S. R. Ramp, C. W. Miller, J. F. Lynch, T. F. Duda, and T. Y. Tang, Acoustic intensity fluctuations induced by south china sea internal tides and solitons, *IEEE Journal of Oceanic Engineering*, *29*(4), 1249–1263, 2004.

Choi, W., The effect of a background shear current on large amplitude internal solitary waves, *Physics of Fluids*, *18*, 036,601, 2006.

Coastal Data Information Program, Coastal data information program station 073 - scripps pier, la jolla ca, 2016-2017.

Colosi, J. A., R. C. Beardsley, J. F. Lynch, G. Gawarkiewicz, C. S. Chiu, and A. Scotti, Observations of nonlinear internal waves on the outer New England continential shelf during the summer Shelfbreak Primer Study, *J. Geophys. Res.*, *106*(C5), 9587–9601, 2001.

Dartnell, P., W. R. Normark, N. W. Driscoll, J. M. Babcock, J. V. Gardner, R. G. Kvitek, and P. J. Iampietro, Multibeam bathymetry and selected perspective views offshore san diego, california, *Tech. rep.*, 2007.

De Leo, F. C., C. R. Smith, A. A. Rowden, D. A. Bowden, and M. R. Clark, Submarine canyons: hotspots of benthic biomass and productivity in the deep sea, *Proceedings of the Royal Society of London B: Biological Sciences*, p. rspb20100462, 2010.

Denman, K., D. Mackas, H. Freeland, M. Austin, and S. Hill, Persistent upwelling and mesoscale zones of high productivity off the west coast of vancouver island, canada, *Coastal upwelling*, *1*, 514–521, 1981.

DeVries, T., M. Holzer, and F. Primeau, Recent increase in oceanic carbon uptake driven by weaker upper-ocean overturning, *Nature*, *542*, 215 EP –, 2017.

Dillon, T. M., Vertical overturns: A comparison of Thorpe and Ozmidov length scales, *J. Geophys. Res.*, *87*, 9601–9613, 1982.

Eriksen, C. C., Observations of internal wave reflection off sloping bottoms, *J. Geophys. Res.*, *87*, 525–538, 1982.

Farmer, D. M., and L. Armi, The generation and trapping of solitary waves over topography, *Science*, *283*, 188–190, 1999.

Farmer, D. M., and J. D. Smith, Generation of lee waves over the sill in Knight Inlet, in *Fjord Oceanography*, edited by H. J. Freeland, D. M. Farmer, and C. Levings, pp. 259–269, Plenum Press, New York, 1980.

Ferron, B. H., H. Mercier, K. Speer, A. Gargett, and K. Polzin, Mixing in the Romanche Fracture Zone, *J. Phys. Oceanogr.*, *28*, 1929–1945, 1998.

Filonov, A., and V. Novotryasov, Features of the nonlinear internal wave spectrum in the coastal zone, *Geophys. Res. Lett.*, *32*(L15602), doi:10.1029/2005GL023,046, 2005.

Frants, M., G. M. Damerell, S. T. Gille, K. J. Heywood, J. MacKinnon, and J. Sprintall, An assessment of density-based finescale methods for estimating diapycnal diffusivity in the southern ocean, *Journal of Atmospheric and Oceanic Technology*, *30*(11), 2647–2661, 2013.

Friedrich, T., A. Timmermann, T. Decloedt, D. Luther, and A. Mouchet, The effect of topography-enhanced diapycnal mixing on ocean and atmospheric circulation and marine biogeochemistry, *Ocean Modelling*, *39*(3), 262–274, 2011.

Gargett, A., and T. Garner, Determining Thorpe Scales from Ship-Lowered CTD Density Profiles, *Journal of Atmospheric and Oceanic Technology*, *25*, 1657–1670, 2008.

Garrett, C. J. R., and W. H. Munk, Space-time scales of internal waves: A progress report, *J. Geophys. Res.*, *80*(3), 291–297, 1975.

Gerkema, T., A unified model for the generation and fission of internal tides and solitary waves, *J. Mar. Res.*, *54*, 421–450, 1995.

Gill, A. E., *Atmosphere-Ocean Dynamics*, 662 pp., Academic Press, 1982.

Goosse, H., E. Deleersnijder, T. Fichefet, and M. H. England, Sensitivity of a global coupled ocean-sea ice model to the parameterization of vertical mixing, *Journal of Geophysical Research: Oceans*, *104*(C6), 13,681–13,695, doi:10.1029/1999jc900099, 1999.

Gordon, R., and N. Marshall, Submarine canyons: Internal wave traps?, *Geophysical Research Letters*, *3*(10), 622–624, 1976.

Gregg, M., Estimation and geography of diapycnal mixing in the stratified ocean, *Physical processes in lakes and oceans*, 1998.

Gregg, M., and C. Cox, The vertical microstructure of temperature and salinity, *Deep-Sea Res.*, *19*, 355–376, 1972.

Gregg, M. C., R. A. Hall, G. S. Carter, M. H. Alford, R. Lien, D. P. Winkel, and D. J. Wain, Flow and mixing in Ascension, a steep, narrow canyon, *J. Geophys. Res.*, *116*(C07016), doi:doi:10.1029/2010JC006610, 2011.

Hales, B., Irreversible nitrate fluxes due to turbulent mixing in a coastal upwelling system, *Journal of Geophysical Research*, *110*(C10), doi:10.1029/2004jc002685, 2005.

Hall, R. A., and G. S. Carter, Internal tides in monterey submarine canyon, *Journal of Physical Oceanography*, *41*(1), 186–204, doi:10.1175/2010jpo4471.1, 2011.

Hall, R. A., M. H. Alford, G. S. Carter, M. C. Gregg, R.-C. Lien, D. J. Wain, and Z. Zhao, Transition from partly standing to progressive internal tides in monterey submarine canyon, *Deep Sea Research Part II: Topical Studies in Oceanography*, *104*, 164–173, 2014.

Hall, R. A., T. Aslam, and V. A. Huvenne, Partly standing internal tides in a dendritic submarine canyon observed by an ocean glider, *Deep Sea Research Part I: Oceanographic Research Papers*, 2017.

Hamann, M. M., M. H. Alford, A. J. Lucas, and A. F. Waterhouse, Reflected internal tides in a shelf-incising submarine canyon: dynamics, turbulence, and context, 2019.

Haney, R. L., On the pressure gradient force over steep topography in sigma coordinate ocean models, *Journal of Physical Oceanography*, *21*(4), 610–619, doi:10.1175/1520-0485(1991)021⟨0610:otpgfo⟩2.0.co;2, 1991.

Harris, P. T., and T. Whiteway, Global distribution of large submarine canyons: Geomorphic differences between active and passive continental margins, *Marine Geology*, *285*(1), 69–86, 2011.

Helfrich, K. R., and W. K. Melville, Long nonlinear internal waves, *Ann. Rev. Fluid Mech.*, *38*, 395–425, 2006.

Hickey, B., The response of a steep-sided, narrow canyon to time-variable wind forcing, *J. Phys. Oceanogr.*, *27*(5), 697–726, 1997.

Hickey, B., E. Baker, and N. Kachel, Suspended particle movement in and around quinault submarine canyon, *Marine Geology*, *71*(1-2), 35–83, doi:10.1016/0025-3227(86)90032-0, 1986.

Hickey, B. M., Coastal submarine canyons, in *Topographic Effects in the Ocean, Proceedings Hawaiian Winter Workshop, Jan. 17–20, 1995*, edited by P. Müller and D. Henderson, pp. 95–110, Hawaii Institute of Geophysics, Honolulu, HI 96822, 1995.

Holloway, P. E., Internal hydraulic jumps and solitons at a shelf break region on the australian north west shelf, *Journal of Geophysical Research*, *92*(C5), 5405, doi:10.1029/jc092ic05p05405, 1987.

Hosegood, P., and H. van Haren, Near-bed solibores over the continental slope in the faeroe-shetland channel, *Deep Sea Research Part II: Topical Studies in Oceanography*, *51*(25), 2943–2971, 2004.

Hotchkiss, F. S., and C. Wunsch, Internal waves in Hudson Canyon with possible geological implications, *Deep-Sea Res.*, *29*, 415–422, 1982.

Howell, K., J. Davies, and B. Narayanaswamy, Identifying deep-sea megafaunal epibenthic assemblages for use in habitat mapping and marine protected area network design, *Journal of the Marine Biological Association of the United Kingdom*, *90*(1), 33–68, 2010.

Hyder, P., D. Jeans, E. Cauquil, and R. Nerzic, Observations and predictability of internal solitons in the northern andaman sea, *Applied Ocean Research*, *27*(1), 1–11, 2005.

Inall, M. E., T. P. Rippeth, and T. J. Sherwin, Impact of nonlinear waves on the dissipation of internal tidal energy at a shelf break, *J. Geophys. Res.*, *105*(C4), 8687–8705, 2000.

Inman, D. L., C. E. Nordstrom, and R. E. Flick, Currents in submarine canyons: an air-sea-land interaction, *Annual Review of Fluid Mechanics*, *8*(1), 275–310, 1976.

Ivey, G., and R. Nokes, Vertical mixing due to the breaking of critical internal waves on sloping boundaries, *J. Fluid Mech*, *204*, 479–500, 1989.

Jackson, C. R., and J. Apel, An atlas of oceanic internal solitary waves and their properties, $http://www.internalwaveatlas.com/Atlas2\_index.html$, 2004.

Jackson, C. R., J. C. da Silva, and G. Jeans, The generation of nonlinear internal waves, 2012.

Jeans, D., and T. Sherwin, The variability of strongly non-linear solitary internal waves observed during an upwelling season on the portuguese shelf, *Continental Shelf Research*, *21*(16), 1855–1878, 2001.

Jochum, M., Impact of latitudinal variations in vertical diffusivity on climate simulations, *Journal of Geophysical Research*, *114*(C1), doi:10.1029/2008jc005030, 2009.

Kämpf, J., Transient wind-driven upwelling in a submarine canyon: A process-oriented modeling study, *Journal of Geophysical Research: Oceans*, *111*(C11), 2006.

Kavanaugh, M., F. Abdala, H. Ducklow, D. Glover, W. Fraser, D. Martinson, S. Stammerjohn, O. Schofield, and S. Doney, Effect of continental shelf canyons on phytoplankton biomass and community composition along the western antarctic peninsula, *Marine Ecology Progress Series*, *524*, 11–26, doi:10.3354/meps11189, 2015.

Kelly, S., J. Nash, and E. Kunze, Internal-tide energy over topography, *J. Geophys. Res.*, *115*(C06014), doi:10.1029/2009JC005,618, 2010.

Kelly, S., J. D. Nash, M. H. Alford, and K. I. Martini, The cascade of tidal energy from low to high modes on a continental slope, *J. Phys. Oceanogr.*, *42*(7), 1217–1232, 2012.

Klinck, J. M., Geostrophic adjustment over submarine canyons, *Journal of Geophysical Research*, *94*(C5), 6133, doi:10.1029/jc094ic05p06133, 1989.

Klymak, J. M., and J. N. Moum, Internal solitary waves of elevation advancing on a shoaling shelf, *Geophys. Res. Lett.*, *30*(20), 2045, doi:10.1029/2003GL017,706, 2003.

Klymak, J. M., J. N. Moum, J. D. Nash, E. Kunze, J. B. Girton, G. S. Carter, C. M. Lee, T. B. Sanford, and M. C. Gregg, An estimate of tidal energy lost to turbulence at the Hawaiian Ridge, *J. Phys. Oceanogr.*, *36*(6), 1148–1164, 2006.

Klymak, J. M., R. Pinkel, and L. Rainville, Direct breaking of the internal tide near topography: Kaena Ridge, Hawaii, *J. Phys. Oceanogr.*, *38*, 380–399, 2008.

Koch-Larrouy, A., A. Atmadipoera, P. Van Beek, G. Madec, J. Aucan, F. Lyard, J. Grelet, and M. Souhaut, Estimates of tidal mixing in the indonesian archipelago from multidisciplinary indomix in-situ data, *Deep Sea Research Part I: Oceanographic Research Papers*, *106*, 136–153, 2015.

Konyaev, K., K. Sabinin, and A. Serebryany, Large-amplitude internal waves at the mascarene ridge in the indian ocean, *Deep Sea Research Part I: Oceanographic Research Papers*, *42*(11-12), 2075–2091, doi:10.1016/0967-0637(95)00067-4, 1995.

Kraichnan, R., Small-scale structure of a scalar field convected by turbulence, *Phys. Fluids*, *11*, 945–953, 1968.

Kundu, P., I. Cohen, and D. Dowling, *Fluid Mechanics*, Academic Press, New York, NY, 2012.

Kunze, E., L. K. Rosenfeld, G. S. Carter, and M. C. Gregg, Internal waves in Monterey Submarine Canyon, *J. Phys. Oceanogr.*, *32*(6), 1890–1913, 2002.

Kunze, E., C. MacKay, E. E. McPhee-Shaw, K. Morrice, J. B. Girton, and S. R. Terker, Turbulent mixing and exchange with interior waters on sloping boundaries, *J. Phys. Oceanogr.*, *42*, 910–927, 2012.

LaCasce, J. H., The prevalence of oceanic surface modes, *Geophysical Research Letters*, *44*(21), 11,097–11,105, doi:10.1002/2017gl075430, 2017.

Lamb, K., A numerical investigation of solitary internal waves with trapped cores formed via shoaling, *Journal of Fluid Mechanics*, *451*, 109–144, 2002.

Lamb, K. G., Particle transport by nonbreaking, solitary internal waves, *Journal of Geophysical research*, *102*(C8), 18,641–18, 1997.

Lamb, K. G., Internal wave breaking and dissipation mechanisms on the continental slope/shelf, *Ann. Rev. Fluid Mech.*, *46*, 231–254, 2014.

Lee, C.-Y. u., and R. C. Beardsley, The generation of long nonlinear internal waves in a weakly stratified shear flow, *J. Geophys. Res.*, *79*(3), 453–462, 1974.

Lee, I., R. Lien, J. T. Liu, and W. Chuang, Turbulent mixing and internal tides in Gaoping (Kaoping) Submarine Canyon, Taiwan, *Journal of Marine Systems*, *76*, 383–396, 2009.

Lee, T., Decadal weakening of the shallow overturning circulation in the south indian ocean, *Geophysical research letters*, *31*(18), 2004.

Lentz, S. J., and C. Winant, Subinertial currents on the Southern California Shelf, *J. Phys. Oceanogr.*, *16*(11), 1737–1750, 1986.

Levine, M. D., and T. J. Boyd, Tidally forced internal waves and overturns observed on a slope: Results from HOME, *J. Phys. Oceanogr.*, *36*(6), 1184–1201, 2006.

Lévy, M., The modulation of biological production by oceanic mesoscale turbulence, in *Transport and Mixing in Geophysical Flows*, pp. 219–261, Springer, 2008.

Li, Q. P., P. J. Franks, M. D. Ohman, and M. R. Landry, Enhanced nitrate fluxes and biological processes at a frontal zone in the southern california current system, *Journal of plankton research*, *34*(9), 790–801, 2012.

Lien, R.-C., F. Henyey, B. Ma, and Y.-J. Yang, Large-amplitude internal solitary waves observed in the northern South China Sea: Properties and energetics, *J. Phys. Oceanogr.*, *44*(4), 1095–1115, 2014.

Liu, A. K., J. R. Holbrook, and J. R. Apel, Nonlinear internal wave evolution in the Sulu Sea, *J. Phys. Oceanogr.*, *15*, 1613–1624, 1985.

Liu, J. T., K.-j. Liu, and J. C. Huang, The effect of a submarine canyon on the river sediment dispersal and inner shelf sediment movements in southern taiwan, *Marine Geology*, *181*(4), 357–386, doi:10.1016/s0025-3227(01)00219-5, 2002.

Lucas, A. J., P. J. S. Franks, and C. L. Dupont, Horizontal internal-tide fluxes support elevated phytoplankton productivity over the inner continental shelf, *Limnology and Oceanography: Fluids and Environments*, *1*(1), 56–74, doi:10.1215/21573698-1258185, 2011.

MacKinnon, J. A., and M. C. Gregg, Mixing on the late-summer New England Shelf- Solibores, shear, and stratification, *J. Phys. Oceanogr.*, *33*, 1476–1492, 2003.

MacKinnon, J. A., et al., Climate process team on internal-wave driven ocean mixing, *Bulletin of the American Meteorological Society*, *98*(11), 2429–2454, doi:10.1175/bams-d-16-0030.1, 2017.

Martini, K. I., M. H. Alford, J. D. Nash, E. Kunze, and M. A. Merrifield, Diagnosing a partly standing internal wave in Mamala Bay, Oahu, *Geophys. Res. Lett.*, *34*(L17604), doi:10.1029/2007GL029,749, 2007.

Maxworthy, T., A note on the internal solitary waves produced by tidal flow over a three-dimensional ridge, *Journal of Geophysical Research: Oceans (1978–2012)*, *84*(C1), 338–346, 1979.

Melet, A., R. Hallberg, S. Legg, and K. L. Polzin, Sensitivity of the ocean state to the vertical distribution of internal-tide-driven mixing, *J. Phys. Oceanogr.*, *43*(3), 602–615, doi:http://dx.doi.org/10.1175/JPO-D-12-055.1, 2013.

Melet, A., S. Legg, and R. Hallberg, Climatic impacts of parameterized local and remote tidal mixing, *Journal of Climate*, *29*(2016), 3473–3500, 2016.

Miles, J. W., and L. N. Howard, Note on a heterogeneous shear flow, *J. Fluid Mech.*, *20*(02), 331, doi:10.1017/s0022112064001252, 1964.

Moum, J., and J. Nash, Mixing measurements on an equatorial ocean mooring, *J. Atmos. Ocean. Tech.*, *26*, 317–336, 2009.

Moum, J., D. Farmer, E. Shroyer, W. Smyth, and L. Armi, Dissipative losses in nonlinear internal waves propagating across the continental shelf, *J. Phys. Oceanogr.*, *37*(7), 1989–1995, 2007.

Moum, J. N., and J. D. Nash, Seafloor pressure measurements of nonlinear internal waves, *J. Phys. Oceanogr.*, *38*, 481–491, 2008.

Muller, P., and X. Liu, Scattering of internal waves at finite topography in two dimensions. Part I: Theory and case studies, *J. Phys. Oceanogr.*, *30*, 532–549, 2000.

Munk, W. H., Abyssal recipes, *Deep-Sea Res.*, *13*, 707–730, 1966.

Musgrave, R. C., J. A. MacKinnon, R. Pinkel, A. F. Waterhouse, and J. Nash, Tidally Driven Processes Leading to Near-Field Turbulence in a Channel at the Crest of the Mendocino Escarpment*, *J. Phys. Oceanogr.*, *46*(4), 1137–1155, doi:10.1175/jpo-d-15-0021.1, 2016.

Nakamura, T., T. Awaji, T. Hatayama, K. Akitomo, T. Takizawa, T. Kono, Y. Kawasaki, and M. Fukasawa, The generation of large-amplitude unsteady lee waves by subinertial k 1 tidal flow: A possible vertical mixing mechanism in the kuril straits, *J. Phys. Oceanogr.*, *30*(7), 1601–1621, 2010.

Nam, S., and U. Send, Direct evidence of deep water intrusions onto the continental shelf via surging internal tides, *Journal of Geophysical Research*, *116*(C5), doi:10.1029/2010jc006692, 2011.

Nash, J., E. Kunze, K. Polzin, J. Toole, and R. Schmitt, Internal tide reflection and turbulent mixing on the continental slope, *J. Phys. Oceanogr.*, *34*, 1117–1134, 2004.

Nash, J. D., M. H. Alford, and E. Kunze, Estimating internal-wave energy fluxes in the ocean, *J. Atmos. Ocean. Tech.*, *22*(10), 1551–1570, 2005.

Nash, J. D., E. Kunze, C. M. Lee, and T. B. Sanford, Structure of the baroclinic tide generated at Kaena ridge, Hawaii, *J. Phys. Oceanogr.*, *36*(6), 1123–1135, 2006.

Nash, J. D., S. M. Kelly, E. L. Shroyer, J. N. Moum, and T. F. Duda, The unpredictable nature of internal tides and nonlinear waves on the continental shelf, *J. Phys. Oceanogr.*, *42*(11), 1981–2000, 2012.

National Oceanic and Atmospheric Administration, La jolla, ca - station id: 9410230, 2016-2017.

Nazarian, R. H., and S. Legg, Internal wave scattering in continental slope canyons, part 1: Theory and development of a ray tracing algorithm, *Ocean Modelling*, *118*, 1–15, doi:10.1016/j.ocemod.2017.07.002, 2017.

Oakey, N. S., Determination of the rate of dissipation of turbulent energy from simultaneous temperature and velocity shear microstructure measurements, *J. Phys. Oceanogr.*, *12*, 256–271, 1982.

Osborn, T. R., Estimates of the local rate of vertical diffusion from dissipation measurements, *J. Phys. Oceanogr.*, *10*, 83–89, 1980.

Osborn, T. R., and C. S. Cox, Oceanic fine structure, *Geophys. Fluid Dyn.*, *3*, 321–345, 1972.

Osborne, A., and T. Burch, Internal solitons in the andaman sea, *Science*, *208*(4443), 451–460, 1980.

Perry, R. B., and G. R. Schimke, Large-amplitude internal waves observed off the northwest coast of sumatra, *Journal of Geophysical Research*, *70*(10), 2319–2324, 1965.

Petruncio, E. T., L. K. Rosenfeld, and J. D. Paduan, Observations of the internal tide in Monterey Canyon, *J. Phys. Oceanogr.*, *28*, 1873–1903, 1998.

Pineda, J., Predictable upwelling and the shoreward transport of planktonic larvae by internal tidal bores., *Science(Washington)*, *253*(5019), 548–551, 1991.

Pinkel, R., J. Sherman., J. Smith, and S. Anderson, Strain: Observations of the vertical gradient of isopycnal vertical displacement, *J. Phys. Oceanogr.*, *22*, 527–540, 1991.

Pinkel, R., M. A. Goldin, J. A. Smith, O. M. Sun, A. A. Aja, M. N. Bui, and T. Hughen, The wirewalker: A vertically profiling instrument carrier powered by ocean waves, *Journal of Atmospheric and Oceanic Technology*, *28*(3), 426–435, doi:10.1175/2010jtecho805.1, 2011.

Pinkel, R., et al., Tidal energy conversion and ocean mixing processes at Kaena Ridge, Hawaii, *Science*, *in prep.*, 2006.

Pinkel, R., et al., Breaking internal tides keep the ocean in balance, *EOS Transactions*, *96*, doi:10.1029/2015EO039,555, 2015.

Ponte, A. L., and B. Cornuelle, Coastal numerical modelling of tides: sensitivity to domain size and remotely generated internal tide., *Ocean Modelling*, 2013.

Puig, P., A. Ogston, B. Mullenbach, C. Nittrouer, and R. Sternberg, Shelf-to-canyon sediment-transport processes on the eel continental margin (northern california), *Marine Geology*, *193*(1-2), 129–149, doi:10.1016/s0025-3227(02)00641-2, 2003.

Rainville, L., and R. Pinkel, Wirewalker: An autonomous wave-powered vertical profiler, *Journal of Atmospheric and Oceanic Technology*, *18*(6), 1048–1051, doi:10.1175/1520-0426(2001)018⟨1048:waawpv⟩2.0.co;2, 2001.

Reid, J. L., The shallow salinity minima of the pacific ocean, *Deep Sea Research and Oceanographic Abstracts*, *20*(1), 51–68, doi:10.1016/0011-7471(73)90042-9, 1973.

Rhines, P., Edge-, Bottom-, and Rossby Waves in a Rotating Stratified Fluid, *Geophys. Fluid. Dyn.*, *1*, 273–302, 1970.

Rodenborn, B., D. Kiefer, H. P. Zhang, and H. L. Swinney, Harmonic generation by reflecting internal waves, *Physics of Fluids*, *23*(2), 026601, doi:http://dx.doi.org/10.1063/1.3553294, 2011.

Saenko, O. A., and W. J. Merryfield, On the effect of topographically enhanced mixing on the global ocean circulation, *J. Phys. Oceanogr.*, *35*(5), 826–835, 2005.

Samelson, R. M., Large scale circulation with locally enhanced vertical mixing, *J. Phys. Oceanogr.*, *28*(4), 712–726, 1998.

Sanchez, F., G. Morandeau, N. Bru, and M. Lissardy, A restricted fishing area as a tool for fisheries management: example of the capbreton canyon, southern bay of biscay, *Marine Policy*, *42*, 180–189, 2013.

Sandstrom, H., and J. A. Elliott, Internal tide and solitons on the scotian shelf: A nutrient pump at work, *J. Geophys. Res.*, *89*(C4), 6415–6426, doi:10.1029/JC089iC04p06415, 1984.

Sandstrom, H., and N. S. Oakey, Dissipation in internal tides and solitary waves, *J. Phys. Oceanogr.*, *25*, 604–614, 1995.

Schafstall, J., M. Dengler, P. Brandt, and H. Bange, Tidal-induced mixing and diapycnal nutrient fluxes in the mauritanian upwelling region, *Journal of Geophysical Research: Oceans (1978–2012)*, *115*(C10), 2010.

Schmittner, A., J. A. M. Green, and S.-B. Wilmes, Glacial ocean overturning intensified by tidal mixing in a global circulation model, *Geophysical Research Letters*, *42*(10), 4014–4022, doi:10.1002/2015gl063561, 2015.

Scotti, A., and J. Pineda, Observation of very large and steep internal waves of elevation near the massachusetts coast, *Geophys. Res. Lett.*, *31*(L22307), 1–4, 2004.

Scotti, A., and J. Pineda, Plankton accumulation and transport in propagating nonlinear internal fronts, *Journal of Marine Research*, *65*(1), 117–145, 2007.

Scotti, A., R. Beardsley, B. Butman, and J. Pineda, Shoaling of nonlinear internal waves in massachusetts bay, *J. Geophys. Res.*, *113*(C08031), 2008.

Shepard, F., and D. Inman, Nearshore water circulation related to bottom topography and wave refraction, *Eos, Transactions American Geophysical Union*, *31*(2), 196–212, 1950.

Shepard, F. P., N. F. Marshall, and P. A. Mcloughlin, Currents in submarine canyons, *Deep Sea Res.*, *21*, 691–706, 1974.

Shroyer, E., J. Moum, and J. Nash, Energy transformations and dissipation of nonlinear internal waves over new jersey's continental shelf, *Nonlinear processes in Geophysics*, *17*, 345–360, 2010a.

Shroyer, E., J. Moum, and J. Nash, Nonlinear internal waves over New Jersey's continental shelf, *J. Geophys. Res.*, *116*(C03022), 1–16, 2011.

Shroyer, E. L., J. N. Moum, and J. D. Nash, Vertical heat flux and lateral mass transport in nonlinear internal waves, *Geophysical Research Letters*, *37*(8), 2010b.

Simmons, H., S. Jayne, L. S. Laurent, and A. Weaver, Tidally driven mixing in a numerical model of the ocean general circulation, *Ocean Modell.*, *6*, 245–263, 2004.

Stastna, M., and K. Lamb, Large fully nonlinear internal solitary waves: The effect of background current, *Physics of Fluids*, *14*, 2987, 2002.

Stephenson, G. R., J. A. M. Green, and M. E. Inall, Systematic bias in baroclinic energy estimates in shelf seas, *Journal of Physical Oceanography*, *46*(9), 2851–2862, doi: 10.1175/jpo-d-15-0215.1, 2016.

Swain, D. L., B. Langenbrunner, J. D. Neelin, and A. Hall, Increasing precipitation volatility in twenty-first-century california, *Nature Climate Change*, *8*(5), 427, 2018.

Talley, L. D., Shallow, intermediate, and deep overturning components of the global heat budget, *Journal of Physical Oceanography*, *33*(3), 530–560, doi:10.1175/1520-0485(2003)033⟨0530: siadoc⟩2.0.co;2, 2003.

Tanaka, T., I. Yasuda, Y. Tanaka, and G. S. Carter, Numerical study on tidal mixing along the shelf break in the green belt in the southeastern bering sea, *Journal of Geophysical Research: Oceans*, *118*(12), 6525–6542, doi:10.1002/2013jc009113, 2013.

Thomas, J., J. Lerczak, and J. Moum, Horizontal variability of high-frequency nonlinear internal waves in massachusetts bay detected by an array of seafloor pressure sensors, *Journal of Geophysical Research: Oceans*, *121*(8), 5587–5607, 2016.

Thorpe, S., Turbulence and mixing in a Scottish Loch., *Philos. Trans. R. Soc. London Ser. A*, *286*, 125–181, 1977.

Thorpe, S. A., Internal wave reflection and scatter from sloping rough topography, *J. Phys. Oceanogr.*, *31*, 537–553, 2001a.

Thorpe, S. A., On the reflection of internal wave groups from sloping topography, *J. Phys. Oceanogr.*, *31*, 3121–3126, 2001b.

Vetter, E., and P. Dayton, Organic enrichment by macrophyte detritus, and abundance patterns of megafaunal populations in submarine canyons, *Marine ecology. Progress series*, *186*, 137–148, 1999.

Vetter, E. W., Hotspots of benthic production, *Nature*, *372*(6501), 47–47, 1994.

Vetter, E. W., C. R. Smith, and F. C. De Leo, Hawaiian hotspots: enhanced megafaunal abundance and diversity in submarine canyons on the oceanic islands of hawaii, *Marine Ecology*, *31*(1), 183–199, doi:10.1111/j.1439-0485.2009.00351.x, 2010.

Wain, D. J., M. C. Gregg, M. H. Alford, R. C. Lien, G. S. Carter, and R. A. Hall, Propagation and dissipation of the internal tide in upper Monterey Canyon, *J. Geophys. Res.*, *118*, 4855–4877, 2013.

Walter, R. K., M. Stastna, C. B. Woodson, and S. G. Monismith, Observations of nonlinear internal waves at a persistent coastal upwelling front, *Continental Shelf Research*, *117*, 100–117, 2016.

Waterhouse, A. F., S. E. Allen, and A. W. Bowie, Upwelling flow dynamics in long canyons at low Rossby number, *Journal of Geophysical Research: Oceans (1978–2012)*, *114*(C5), 2009.

Waterhouse, A. F., J. A. Mackinnon, R. C. Musgrave, S. M. Kelly, A. Pickering, and J. Nash, Internal tide convergence and mixing in a submarine canyon, *Journal of Physical Oceanography*, *47*(2), 303–322, 2017.

Wesson, J. C., and M. C. Gregg, Mixing at Camarinal Sill in the Strait of Gibraltar, *J. Geophys. Res.*, *99*(C5), 9847–9878, 1994.

Wunsch, C., On the propagation of internal waves up a slope, *Deep-Sea Res.*, *15*, 251–258, 1968.

Wunsch, C., and R. Ferrari, Vertical mixing, energy and the general circulation of the oceans, *Ann. Rev. Fluid Mech.*, *36*, 281–314, 2004.

Zhang, S., and M. H. Alford, Instabilities in nonlinear internal waves on the Washington continental shelf, *Journal of Geophysical Research: Oceans*, *120*, 5272–5283, doi:10.1002/2014JC010638, 2015.

Zhang, S., M. H. Alford, and J. B. Mickett, Characteristics of Nonlinear Internal Waves on the Washington Continental Shelf, *Journal of Geophysical Research: Oceans*, *120*(doi:10.1002/2014JC010393), 2015.

Zhang, W. G., T. F. Duda, and I. A. Udovydchenkov, Modeling and analysis of internal-tide generation and beamlike onshore propagation in the vicinity of shelfbreak canyons, *J. Phys. Oceanogr.*, *44*(3), 834–849, 2014.

Zhang, Y., and J. N. Moum, Inertial-convective subrange estimates of thermal variance dissipation rate from moored temperature measurements., *Journal of Atmospheric & Oceanic Technology*, *27*(11), 2010.

Zhao, Z., and M. H. Alford, Source and propagation of nonlinear internal waves in the northeastern South China Sea, *J. Geophys. Res.*, *111*(C11012), doi:10.1029/2006JC003,644, 2006.

Zhao, Z., M. H. Alford, R.-C. Lien, M. C. Gregg, and G. S. Carter, Internal tides and mixing in a submarine canyon with time-varying stratification, *J. Phys. Oceanogr.*, *42*, 2121–2142, doi:10.1175/JPO-D-12-045.1, 2012.